PhD Thesis

Interactive Proteins and Nanoscale Particles for Cancer Therapeutics

by

Rumi Khandelia

Department of Chemistry

Indian Institute of Technology Guwahati

March 2015

Interactive Proteins and Nanoscale Particles for Cancer Therapeutics

A thesis submitted by

Rumi Khandelia
Roll No. 09612209

to

Indian Institute of Technology Guwahati

for the award of the degree of

Doctor of Philosophy

Department of Chemistry
Indian Institute of Technology Guwahati
Guwahati – 781039
India

March 2015

STATEMENT

This thesis entitled "***Interactive Proteins and Nanoscale Particles for Cancer Therapeutics***" is a work of research and investigation carried out by me under the supervision of Dr. Arun Chattopadhyay, Professor, Department of Chemistry, Indian Institute of Technology Guwahati. This thesis has been submitted by me to the Department of Chemistry, Indian Institute of Technology Guwahati for the award of the degree of Doctor of Philosophy. I further declare that this work has not been submitted anywhere else for any degree, diploma, associateship or membership etc. of any Institute or University to the best of my knowledge.

Rumi Khandelia
Department of Chemistry
IIT Guwahati,
Guwahati-781039, Assam
India

Date:
Place: Guwahati, Assam

CERTIFICATE

It is certified that the thesis entitled "***Interactive Proteins and Nanoscale Particles for Cancer Therapeutics***" being submitted to the Indian Institute of Technology Guwahati by Rumi Khandelia (Roll. No. 09612209) for the award of the degree of Doctor of Philosophy in Chemistry, is a bonafide record of research work carried out by her. The information and data reported by her are solely the results of her original findings. She has meticulously carried out the investigations and followed the guidelines of the laboratory. This work has not been submitted elsewhere for any degree or diploma.

Arun Chattopadhyay
Professor,
Department of Chemistry,
IIT Guwahati,
Guwahati-781039, Assam,
India.
Thesis Supervisor

Dedicated to
My Parents

Mr. Rajkumar Khandelia
&
Mrs. Lalita Khandelia

Acknowledgements

The period that I have spent in IIT Guwahati has been the most precious time in my academic life. Here, I have grown both intellectually and personally. There are many people who have contributed, directly or indirectly, in making my journey in IIT a successful one. I take this opportunity to express my sincere gratitude to everyone who supported me throughout the course of my PhD.

First and foremost, I would like to express my deepest appreciation to my supervisor, Prof. Arun Chattopadhyay, for his constant mentoring, aspiring guidance, invaluable & constructive criticism, friendly advice, for encouraging my research and for allowing me to grow as a research scholar. His advice on research as well as on my career has been priceless. He has introduced in me the concept of patience and perseverance in research. Sir, I would always be indebted to you for shaping my career and personality.

Furthermore, I would like to acknowledge my doctoral committee members Dr. Aiyagari Ramesh, Dr. Debasis Manna and Dr. Manabendra Sarma for evaluating my thesis from time to time. Their expert scrutiny always helped me in analyzing an experimental data more closely and clearly.

I would also like to thank Dr. Anumita Paul, Dr. S. S. Ghosh, Dr. Biplab Bose and Dr. G. Krishnamoorthy for their contribution and support in completion of my PhD thesis. I frequently use to seek their guidance on various topics of research related to physical chemistry and biology. I would also like to acknowledge all the other faculty members of Chemistry Department for extending their endless support and helping me whenever I was in need.

I would also like to acknowledge CIF, IIT Guwahati for permitting me to use the sophisticated instruments like SEM, FESEM, TEM and AFM. I am also very thankful to CSIR, New Delhi, for providing me the PhD fellowship.

I would like to acknowledge all my past and present lab members Jashmini Deka, Krishna Kanti Dey, Pallab Sanpui, Nirmala Devi, Madhulekha Gogoi Borborah, Subhojit Das, Sadhucharan Mallick, Raihana Begum, Amaresh, Palash, Satya, Rama, Anushree, Shilaj, Uday, Sabyasachi, Kafeel, Srestha, Ayan, Upashi, Sunil, Bandhan, Deepanjalee and Srilatha for providing a healthy and friendly environment in the lab.

I would also like to acknowledge the peoples with whom I worked in different projects – Jashmini Deka who introduced me to the research area of nanoparticle-protein interaction, Krishna Kanti Dey for helping me in deriving some of the equations used in my thesis, Amit for teaching me cell culture and Satya for his support in the fluorescence experiments. Uday gave his valuable suggestions from time to time. Subhojit Das taught me to design the experiments, use the instruments and analyze the data in my initial days of research in IIT Guwahati.

Then I would like to acknowledge all the other persons who have directly or indirectly contributed in my research work - Dr. Anupam Banerjee, Mr. Madhukar Chaudhary, Jayanta Mazumder, Indrajit Talukdar, Niranjan Barah, Manab Deb Adhikari, Ziyauddin Khan, Amaresh, Chokalingam, Johney, Anamika, Ashish, Dipjyoti, Puspal, Manoj, Subhamoy, Kohila, Archita, Sharmila, Asif and Neha. A special thanks to Amaresh for helping me out with some of the major problems during my research.

I would also like to acknowledge all the staff members of Department of Chemistry, Centre for Nanotechnolgy and CIF for their support.

Next, I would like to acknowledge Prof. K. Ismail, Dr. Subhra Chakraborty, Dr. Devasish Chowdhury, Dr. J. Mahanta and Dr. Utpala Devi for allowing me to use their instrument facility outside IITG.

At last, I would like to express my thanks to all of my friends outside IIT Guwahati and my family members and relatives who extended their cooperation, support and well wishes during the tenure of my research.

Thanks to all of you. This journey would not have been easy without the support from you all.

Rumi

Table of Contents

CHAPTER 1

Introduction and Literature Review

Nanotechnology has its impact on almost all areas of science like chemistry, biology, physics, material science and engineering. Nanobiotechnology is related to the use of nanotechnology in biotechnological applications. One of the important applications of nanobiotechnology is the use of nanomaterials in cancer therapy and imaging.[1-9]

1.1 Cancer – a Brief Introduction

Cancer is a disorder characterized by an abnormal mass of tissue (formed as a result of mutations in a gene) that grow and divide in an uncontrolled and uncoordinated manner as compared to normal tissue, invade and destroy adjacent structures and spread to distant anatomic sites by metastasis.[10] It could be caused by various chemical, physical or biological factors or it may be inherited in the germ line.[10] Chemical factors include the chemical substances like (i) alkylating agents, (ii) acylating agents, (iii) polycyclic and heterocyclic aromatic hydrocarbons, (iv) aromatic amines, amides and azo dyes and (v) natural plant and microbial products.[10] Physical factors mainly include the radiations (both ultraviolet light and ionizing radiations like X-rays, α-, β-, γ-rays, radioactive isotopes, protons and neutrons) and the biological factors involve the oncogenic viruses and some other microbes.[10] There are various treatments for cancer like surgery, chemotherapy, radiation therapy, immunotherapy, photothermal and photodynamic therapy,[11,12] of which chemotherapy is the most popular and widely used. Chemotherapeutic drugs may be hydrophilic or hydrophobic in nature. Although the hydrophilic drugs can be administered directly in to the body, they have the disadvantage of side effects. For example, doxorubicin hydrochloride (Dox) can cause congestive heart failure.[13] On the other hand, hydrophobic drugs - being water insoluble - cannot be administered directly. They are either given with emulsifying agents like cremophor EL or converted to their water soluble forms.[14,15] Emulsifying agents like cremophor EL lead to hypersensitive reactions in the body due to which premedication with histamine

blockers and steroids is required. In addition, the drug pharmacokinetics is also affected due to micellar encapsulation of the drug formed by cremophor EL.[14] For the latter case, where the drugs are converted to their water soluble forms, sometimes the anticancer activity gets reduced. For example, the anticancer activity of water soluble forms of 20(S)-camptothecin (CPT), i.e. irinotecan and topotecan is lower than that of CPT.[15]

1.2 Nanocarriers for Cancer Drug Delivery

As a result of various problems associated with direct administration of chemotherapeutic drugs into the body, nanocarriers are developed to encapsulate and carry them to the desired tumor site.[1] Several nanocarriers which are approved by Food and Drug Administration (FDA) for cancer therapeutics and are available in market are listed below:

Table 1.1 Representative examples of nanocarrier-based drugs for cancer therapeutics.

Commercial name	Nanocarrier	Drug	Indications	Company
Abraxane[1]	Albumin Nanoparticles	Paclitaxel	Metastatic breast cancer	Abraxis Biosciences
Doxil/Caelyx[1]	PEGylated liposomes	Doxorubicin	Refractory Kaposi's sarcoma, recurrent breast cancer, ovarian cancer	Janssen
Oncaspar[1]	Polymer–protein conjugate	Peg-L-asparaginase	Acute lymphoblastic leukemia	Sigma-Tau Pharmaceuticals
Nanoxel[16]	Polymeric micelle	Paclitaxel	Breast cancer and ovarian cancer	Dabur Pharma

1.2.1 Advantages of nanocarriers

There are various advantages of nanocarriers over free drugs and these are mentioned below:

- Increase the aqueous solubility of the drugs, especially the hydrophobic drugs like paclitaxel, CPT, actinomycin D, curcumin etc.[1,16]
- Protect the drug from premature degradation, hydrolysis or loss during circulation.[1,16] For example, the active lactone form of CPT gets hydrolyzed to inactive carboxylate form at physiological pH (7.4), as shown in **Figure 1.1**, when administered directly and this in turn binds irreversibly with human serum albumin (HSA).[17]
- Minimize the side-effects of the drugs by facilitating preferential uptake of the nanocarriers by the tumor cells through active or passive targeting.[1,16]
- Improve the pharmacokinetics of the drugs.[1,16]
- Facilitate the slow and prolong release of the drugs.[16]
- Offer appropriate form for different routes of administration.[16]

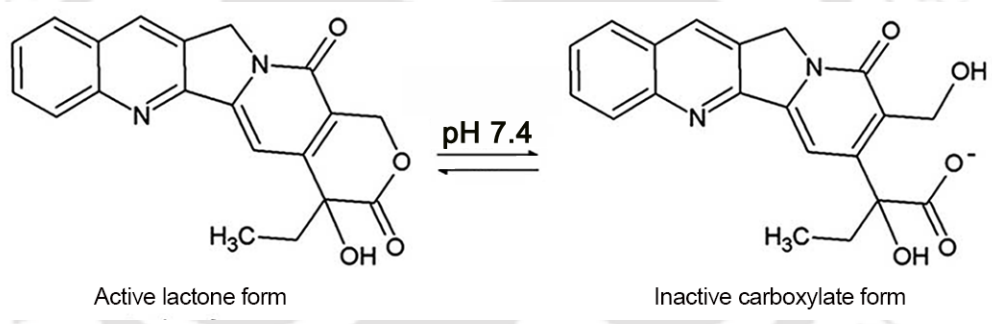

Figure 1.1 Hydrolysis of camptothecin at physiological pH.

1.2.2 Aspects of an ideal nanocarrier

- All the components of a nanocarrier must be biocompatible, well characterized and easily functionalized.[1]
- The nanocarrier must be soluble or dispersible under aqueous conditions.[1]
- The nanocarrier itself must be non-cytotoxic.[1]
- It should have the ability to efficiently encapsulate and release the drugs inside the cancerous cells.[1]
- The nanocarrier must be stable in blood,[18,19] which is a mixture of plasma and several kinds of cells. Plasma, on the other hand, contains different components

such as growth factors, proteins, vitamins, hormones, trace elements, and other essential and non-essential elements.[19] Adsorption of these components on the nanocarrier surface may often results in further aggregation or disruption of the nanocarrier leading to premature unloading of the drug in the systemic circulation before reaching the targeted site.[18]

- It should also be resistant to protease degradation in the presystemic circulation.[20, 21]
- The nanocarrier must have extended circulation half-life and this is mainly governed by the surface charge of the nanocarrier. Although the positively charged nanocarriers are easily internalized by tumor cells (due to negatively charged cell membrane), they are quickly adsorbed by serum proteins and are removed by the mononuclear phagocyte system (MPS) to the liver and spleen. They may also lead to significant immune reactions. Thus, neutral and negatively charged nanocarriers are preferred for in vivo applications.[22, 23]
- The nanocarrier must have the ability to be preferentially internalized by the tumor cells, either through active targeting or passive targeting.[1] Active targeting can be achieved by functionalization of the carrier surface with targeting ligands. These targeting ligands can bind to tumor-specific surface markers and mediate the internalization of the nanocarriers.[1] On the other hand, the size of the nanocarrier is the major factor for passive targeting of tumor cells.[1, 24] As the pores of normal blood vessels are around 10 nm, any nanoformulation greater than 10 nm will preferentially pass through the leaky blood vessels of the tumor vasculature and accumulate in the tumor site because of enhanced permeation and retention (EPR) effect (**Figure 1.2**).[24] Literature reports also suggest that the nanocarriers of less than 200 nm in size are more effective for the EPR effect.[1]
- It should also be amenable to external stimulation of light,[25-27] radiofrequeny,[28] or magnetic field.[29, 30]

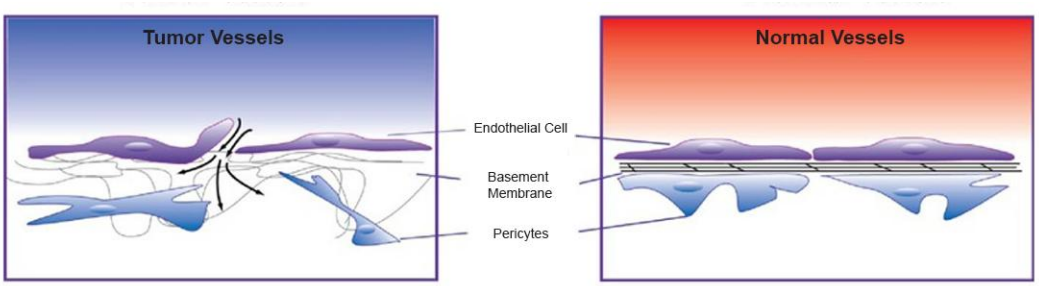

Figure 1.2 Contrary to normal vessels (right), tumor vessels (left) might have an abnormal endothelial cell (EC) lining, an abnormally thick or thin basement membrane (BM), and detached or absent pericytes (PC). As a result, nanocarriers above 10 nm can easily pass through the tumor vessel wall. Reproduced with permission from reference 24.

1.2.3 Types of nanocarriers

There are various types of nanocarriers like liposomes,[31] micelles,[32] dendrimers,[33,34] inorganic,[35-40] protein[41-43] or polymer[44-47] nanoparticles (NPs), carbon nanotubes[48, 49] and quantum dots[50] which are used as drug delivery vehicles (**Figure 1.3**).

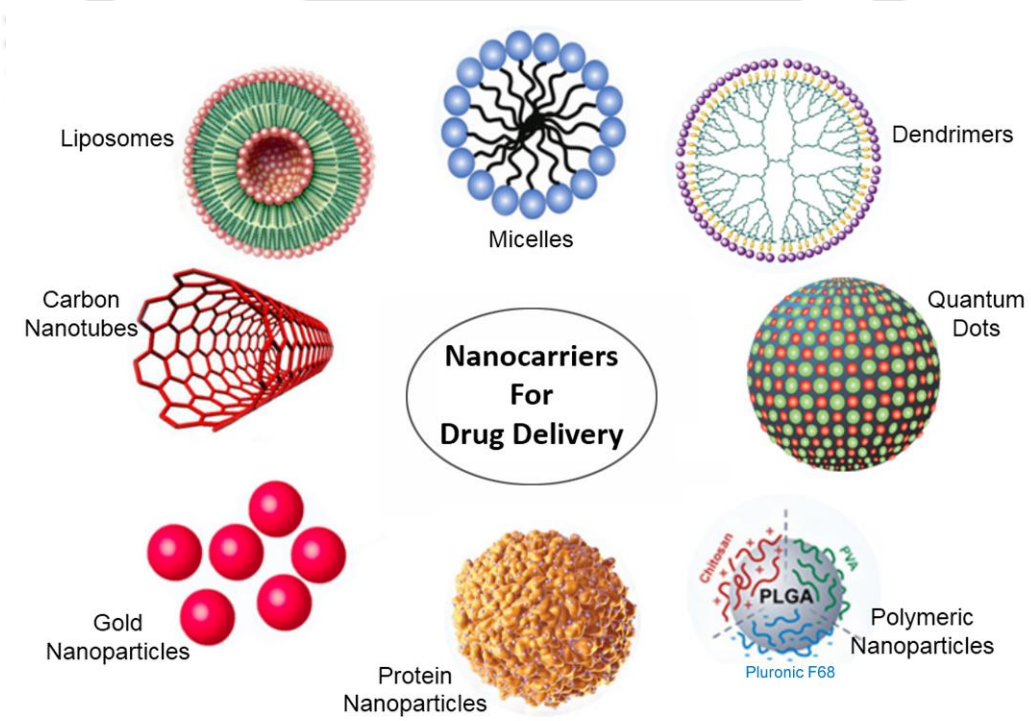

Figure 1.3 Examples of nanocarriers used for cancer drug delivery.

Proteins

Among the above mentioned carriers, proteins are used extensively because of having several advantages like biocompatibility, biodegradability, non-cytotoxicity, high solubility and robust stability in biological environment and most importantly the ability to bind both covalently and non-covalently with wide variety of molecules (like drugs, dyes or targeting ligands), owing to high content of hydrophilic, hydrophobic and charged sites in them.[41, 51, 52] In some cases, the drugs are covalently conjugated to protein molecules[53] and in some, several protein molecules are agglomerated by desolvation to form NPs to which drug molecules are encapsulated.[54] Most commonly used proteins in drug delivery are albumin, transferrin and lysozyme (Lyz).[41-43, 52-57] Albumin is the most abundant protein in plasma (35–50 g L^{-1} human serum) and is known to be a natural transporter of hydrophobic molecules (like vitamins and hormones), endogenous ligands (like fatty acids and prostaglandins) as well as different exogenous molecules (like drugs, antibiotics, anticoagulants and heavy metal ions) in the body.[55, 56] Moreover, the albumin based carriers are known to accumulate preferentially in some tumors like breast, lung and prostate cancer because of the over-expression of the albumin receptor SPARC (secreted protein acid rich in cysteine) on their surfaces.[56] As a result of these specific advantages, paclitaxel loaded albumin nanoparticle has been marketed as Abraxane™, following approval of US FDA and European Medicine Agency (EMA), and is in use against a host of cancers.[41, 56] Transferrin is another example which is being used in targeted drug delivery as its receptors are over-expressed in some tumors.[43] Lyz is a low molecular weight protein (M.W. 14.7 kDa) known for uptake and catabolization in the proximal tubules of the kidney - serving as renal specific drug carriers.[57] Moreover, as the isoelectric point (pI) of Lyz is ~10.7,[58] it remains positively charged at physiological pH (7.4) and thus interacts with negatively charged citrate-stabilized gold NPs (Cit-Au NPs) to form nanoscale agglomerates,[59] which will be discussed in details in the later section.

However, protein carriers undergo protease degradation in the presystemic circulation when administered orally.[20, 21] To improve the stability of protein based nanocarriers, these are conjugated covalently or non-covalently with lipids

or polymers.[20] The use of lipids is limited because of their low stability in the gastrointestinal tract and weak interaction with proteins.[20] Whereas, synthetic polymers, have generated considerable interest due to their ability to protect proteins from enzymatic and hydrolytic degradation in vivo, maintain their activity and integrity and improve their bioavailability.[20] For example, polyethylene glycol-b-polylactic acid (PEG-PLA) nanocarrier served as a protective cage for the enzyme catalase[60] and isobutyl-2-cyanoacrylate nanocapsule retained the activity of the loaded insulin.[21] Among all the polymers available, poly(lactic-co-glycolic acid) (PLGA) is of special interest due to its unique attractive properties like – biocompatibility, bioavailability and biodegradability.[45, 46] PLGA undergoes biodegradation leading to the formation of lactic acid and glycolic acid, which are easily metabolized in the body.[45] Moreover, PLGA-based nanocarriers can be used safely for oral, nasal, pulmonary, parenteral, transdermal and intra-ocular routes of administration.[46] PLGA is also known for controlled and sustained release of the drug and has gained approval from US FDA and EMA in drug delivery systems.[45, 46]

Gold Nanoparticles

Another important candidate in cancer drug delivery is gold nanoparticle (Au NP).[35-40, 61, 62] Au NPs are stable, biocompatible, non-cytotoxic and are suitable for easy and versatile functionalization and depending on their shapes and sizes have high extinction coefficient of light from visible to near infrared (NIR) regions.[25, 63] Au nanorods (NRs) could be used for laser-induced hyperthermia treatment of cancer cells, taking advantage of their NIR absorption characteristics.[5, 64] Further, it has been demonstrated that antibody-conjugated Au NPs could be thermally activated by radiofrequency and the resulting dissipated heat could be used for killing cancer cells.[28] On the other hand, Au NPs functionalized with proteins have been found to be effective for targeting cancer cells.[65] Moreover, cyclic peptide capped Au NPs have been reported to be efficient drug delivery vehicles.[66] Interestingly, protein coronas around Au NRs have shown the promise of storing cancer drug, which could be released by light or heat, although the use of cytotoxic stabilizer prevents their application as such in reality.[26]

1.3 Gold Nanoparticle-Protein Agglomerates

Au NP interacts with almost all proteins but forms agglomerates with some specific proteins.[59, 67, 68] The agglomeration of Au NPs with proteins was first observed by Nidhi et al.[69] They have observed that when the solution temperature - containing Au NPs onto which elastin-like polypeptides were absorbed - was raised from 10 °C to 40 °C, the polypeptides undergo hydrophilic to hydrophobic phase transition, resulting in the agglomeration of Au NPs due to interparticle hydrophobic interaction.[69] Lyz was also demonstrated to form Au NP-protein agglomerates.[59] Lyz being positively charged at physiological pH interacted with negatively charged Au NPs to form Au NP-Lyz agglomerates. Lyz at the Au NP surface were found to be partially unfolded and these partially unfolded proteins were responsible for the formation and growth of agglomerates.[59] In another report, it was demonstrated that the extent of agglomeration for thiol containing proteins (α-amylase and green fluorescent protein) was higher in their native state than denatured state; whereas, for proteins that either did not contain thiol at all (amyloglucosidase, AMG) or contain thiol that was not exposed to the solution (bovine serum albumin, BSA), the agglomeration was higher in the denatured state.[67] In all the above cases, agglomeration of Au NPs was accompanied by broadening of the extinction spectrum of Au NPs.[67]

The physical origin of the extinction of metal NPs is localized surface plasmon resonance (LSPR). According to Mie theory,[70] the electric field of an incoming light wave induces a coherent oscillation of the conduction band electrons at the NP surface, known as LSPR (**Figure 1.4**), if its size is much smaller than the wavelength of the incident light. The extinction results when the oscillation frequency of the conduction band electrons is resonant with the frequency of the incident light wave.

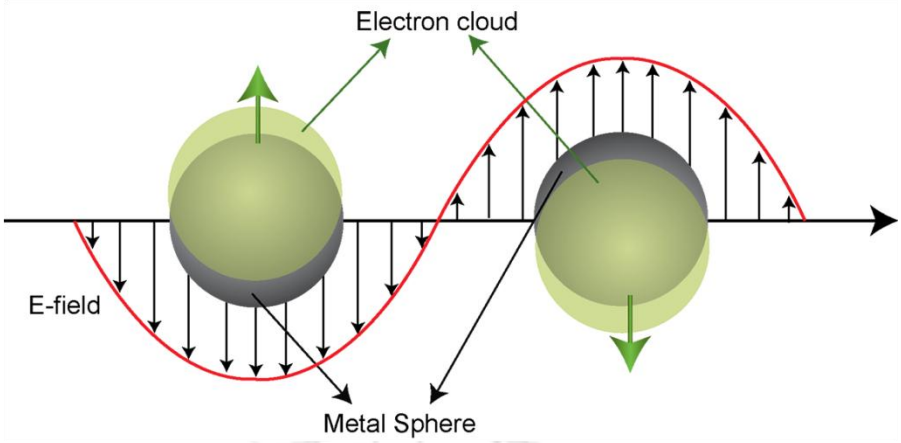

Figure 1.4 A schematic representation of plasmon oscillation on a metal sphere in the presence of an electromagnetic radiation.

It has been observed that a protein at its lower concentrations gets attached to Cit-Au NP accompanied by minimum changes in the extinction spectrum of the NP. However, when the concentration of the protein is increased, the protein-NP composites agglomerate, forming larger structures with red-shifting and broadening of the extinction spectrum of the NP (**Figure 1.5**).[67] With increase in the protein concentration, there was increase in broadening and when the area under the extinction curve was plotted against the concentration of the protein, it varied linearly and the slope of the curve was dependent on the nature and conformational state of the protein.[67] The method allowed estimation of protein with the ability to distinguish conformation (native or denatured) and its fractional content.[67, 68]

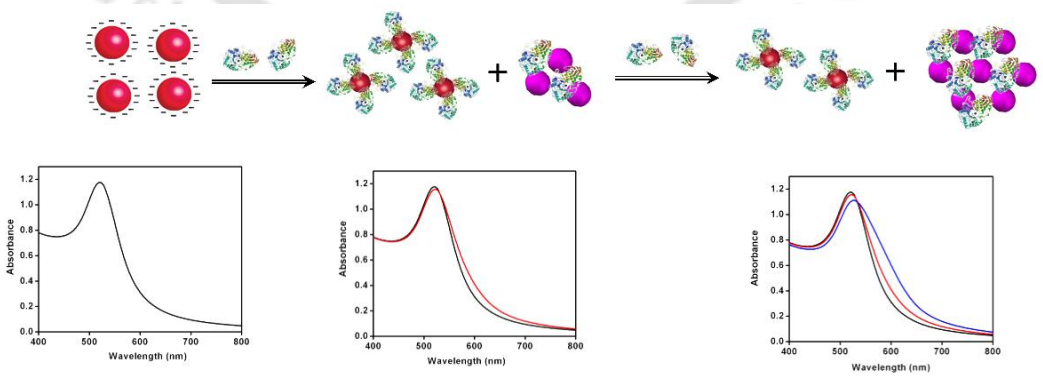

Figure 1.5 A schematic representation of the process of agglomeration of Cit-Au NPs in presence of proteins. Reproduced with permission from reference 68.

1.4 Fluorescent Probes

Fluorescent probes are the imaging agents incorporated in nanocarriers that noninvasively enables a better understanding of the pharmacokinetics of the drug loaded nanocarriers – including their active or passive tumor targeting capability and renal clearance.[71]

1.4.1 Fluorescent probes for clinical utilization

A fluorescent probe – in order to find use in clinical applications - must have characteristics such as both its excitation[72] and emission wavelengths[73-76] must lie in the near-infrared (NIR) region i.e. around 650-900 nm and this is best achieved by multiphoton excitation, with the excitation wavelength longer than the emission peak.[77] NIR window of 650-900 nm is required to reduce the optical absorption by the haemoglobin and water so that the light can easily penetrate in and out of the body tissues, resulting in non-invasive in vivo imaging.[73] This also minimizes the photodamage of the cells[72] and the interferences of light scattering and autofluorescence from biomolecules in the living system.[72, 74-76] Secondly, the fluorescent probe must have high photostability and longer emissive lifetime to allow a real-time whole body imaging and must have large Stokes-shifted emission for higher detection sensitivity.[74-76] Large Stokes-shifted emission decreases the interference between excitation and emission and also shifts the emission spectrum away from the sample autofluorescence.[76] Thirdly, the probe must be non-toxic, chemically inert, biocompatible, soluble and stable at various aqueous conditions such as different pHs, high salt concentrations and various buffers.[78]

Till date, organic fluorophores[79, 80] and quantum dots[81, 82] are used as fluorescent probes for labelling various nanocarriers. However, they have their own limitations – like most of the organic dyes are prone to fast photodegradation, aggregation-induced fluorescence quenching and have small Stokes-shifted emission and small two-photon absorption and excitation cross-section.[78] While some dyes though are photostable, aggregation-induced emission (AIE) active and have large Stokes-shifted emission, however, their syntheses involve multiple steps and are thus cumbersome.[75, 76] Most quantum dots are also not suitable because of the toxicity caused by release of heavy metal ions in an oxidative environment.[78]

1.4.2 Luminescent metal nanoclusters

Luminescent noble metal nanoclusters, with core sizes smaller than 2 nm, are another category of fluorescent probes used for both in vitro[83-88] (**Figure 1.6 a**) and in vivo[89-91] (**Figure 1.6 b**) imaging. Among these, bovine serum albumin

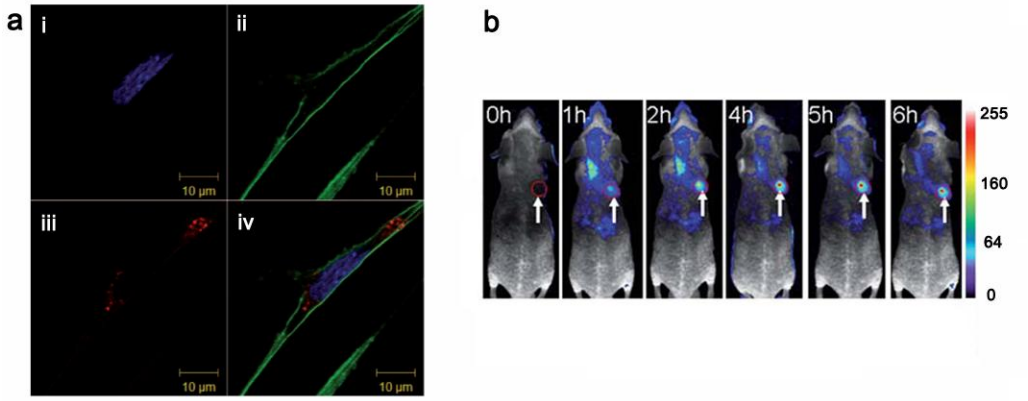

Figure 1.6 Evidences for the use of luminescent metal nanoclusters for in vitro and in vivo imaging. (a) Confocal images of the differentiated C2C12 mouse myoblasts treated with insulin–Au nanoclusters for 2 h. i) Cell nucleus stained with 4', 6-diamidino-2-phenylindole (DAPI, blue), ii) actin fiber stained with Alexa Fluor 488 phalloidin to confirm the cell boundary (green), iii) Insulin–Au nanoclusters exhibit red luminescence and iv) fluorescence image overlay of the three images. (b) Fluorescence images of MDA-MB-45 tumor bearing mice at multiple time points after intravenous injection with BSA-stabilized Au nanoclusters. Strong signal from Au nanoclusters was observed in the tumor (marked by the red circle). The arrowheads indicated the tumor. Reproduced with permission from references 86 and 89.

(BSA)-stabilized Au_{25} nanoclusters are used extensively because their emission is in the window of 650-900 nm, which is an essential requirement for in vivo imaging.[84, 85, 89, 92] Moreover, their unique optical, physicochemical and biological properties like high photostability,[89] longer emissive lifetime,[93] large Stokes-shifted emission,[94] large two-photon absorption and two-photon excitation cross sections,[94] strong X-ray absorption,[90] facile synthesis,[92] good water solubility,[91] high colloidal and chemical stability in biological system,[91] amenability to post-functionalization for active targeting,[84-85] biocompatibility,[89] low toxicity[89] and efficient urinary clearance[89] make them appropriate candidates for bio-imaging. Au_{25} nanoclusters are also known to be used for X-ray-computed tomography (CT) imaging[90] and cancer radiotherapy,[95] thus providing additional option in combination therapy.

1.5 The Present Work

1.5.1 Objectives of this thesis

The objectives of the thesis are as follows:

- As interaction of single protein with Au NPs leading to agglomeration has already been studied, my aim was to study the interaction of some of the important binary protein mixtures with Au NPs and to understand the factors that govern the interaction of an individual protein or the binary mixtures with Cit-Au NPs. The binary protein mixtures selected were α-amylase and bovine serum albumin (BSA), α-amylase and amyloglucosidase (AMG) or glucose oxidase (GOD) and peroxidase (POD). The mixture of α-amylase and BSA was selected because these are easily available proteins and the interaction of individual α-amylase or BSA with Cit-Au NPs is known. The binary mixture of α-amylase and AMG is important in the sense that it helps to convert starch to glucose via dextrins. GOD and POD binary mixture is also important as it is used for the estimation of glucose level in blood and other serums.
- As among all the proteins which are known to interact with Au NPs, Lyz forms stable nanostructures (agglomerates) with Au NPs, my next aim was to form the Au NP-Lyz agglomerates such that they meet the size criterion for possible passive targeting of tumor cells through the EPR effect and to use these agglomerates as a cancer drug delivery vehicle. My aim was also to demonstrate the utility of these agglomerates for the encapsulation of both the hydrophilic and hydrophobic anticancer drugs.
- As for oral administration of protein based nanocarriers, the protease resistivity is a must, my third aim was to make the Au NP-Lyz agglomerates stable against protease degradation by coating with a biodegradable and FDA approved polymer.
- As the usefulness of the Au NP-protein agglomerates for therapeutic application has been established, my fourth aim was to replace the Au NPs of the agglomerates with luminescent Au nanoclusters in order to have a nanotheranostic system (i.e. a nanocarrier having both the fluorescent probe

and the therapeutic drug) that could find clinical utilization. The fluorescent probe would help in better understanding the pharmacokinetics of the drug loaded nanocarrier and the therapeutic drug would help in killing the cancer cells.

1.5.2 Outline of this thesis

The present thesis describes the fabrication of Au NP-protein agglomerates and Au nanocluster-protein agglomerates and their potential applications in cancer therapeutics or imaging. The thesis is organized as follows:

1. **Chapter 1** includes the introduction and the literature review (as above). It gives a general idea about the nanocarriers used for cancer drug delivery with special reference to proteins and Au NPs. It also describes the interaction of Au NPs with proteins leading to inorganic-biomolecule hybrid nanostructures. A basic idea of the fluorescent probes is also given.
2. **Chapter 2** describes the interaction of binary protein mixtures such as – α-amylase-BSA, α-amylase-AMG and GOD-POD with Cit-Au NPs, probed by monitoring the changes in the optical properties of the NPs. It was observed that there was specificity in the interaction and the changes in optical properties of Cit-Au NPs depended on the nature, concentration and order of addition of proteins. Preferential binding of one protein compared to the other, with Cit- Au NPs was decided by the overall charge of the protein in the medium. Estimation of a protein in a binary mixture was possible only if the ratio of the areas under the extinction curve of Cit-Au NPs in the presence of binary mixture to that of Au NPs only varied linearly with concentration of either of the proteins. Interestingly, sensitivity of assay of GOD was increased in presence of POD (i.e. from 1.091 μg mL^{-1} to 45 ng mL^{-1}).
3. **Chapter 3** reports the fabrication of a versatile nanocarrier, based on the agglomerated structures of Au NP and lysozyme (Lyz), for cancer drug delivery. These agglomerates were found to be efficient in loading of both hydrophilic (doxorubicin hydrochloride, Dox) and hydrophobic (pyrene, Pyr) molecules. The interaction between the loaded molecules and the agglomerates were non-covalent. The coating of the loaded agglomerates with albumin not only

provided stability to the nanocarriers but also helped in uptake by the human cervical cancer HeLa cells. Transmission electron microscopy (TEM) and fluorescence microscopy along with flow cytometry analysis confirmed the uptake of the Dox loaded nanocarriers by the cells. XTT based cell viability assay demonstrated that the unloaded nanocarriers were not toxic to the cells whereas the Dox loaded nanocarriers killed the cells very effectively (even more than that of Dox only). Field emission scanning electron microscopy (FESEM) showed the formation of apoptotic bodies on the surface of the cells, thus confirming the release of Dox from the nanocarriers inside the cells. The nanocarriers were biocompatible and meet the size criterion (average hydrodynamic diameter was 183 nm) for enhanced permeability through the leaky vessels of the tumor vasculature. Moreover, the agglomerated Au NPs in the nanocarriers, with extinction extending to the NIR region, can possibly be used for the laser induced hyperthermia treatment of cancer.

4. **Chapter 4** describes the method acquired for increasing the stability of the drug loaded agglomerates against protease degradation in the presystemic circulation. This was done by coating of the drug loaded agglomerates with a biodegradable polymer poly(lactic-co-glycolic acid) (PLGA) via oil in water single emulsion process. The nanocarrier was also found stable in human blood serum and meets the size criterion for possible passive targeting of tumor cells through the EPR effect. Here, CPT was chosen as a model hydrophobic drug because it cannot be administered directly as it is unstable at physiological pH. The active lactone form gets hydrolyzed to inactive carboxylate form, which binds irreversibly with human serum albumin at physiological pH. The polymer coated nanocarriers were internalized by the HeLa cells, where they released their payloads, causing apoptotic cell death.

5. **Chapter 5** describes the fabrication of a nanotheranostic BSA NP having Au nanoclusters as a fluorescent probe and an anticancer drug Dox as a therapeutic agent. The Au nanoclusters (incorporated in BSA NPs) were non-toxic, highly photostable and had suitable quantum yield and large Stokes-shifted emission. Moreover, their (two-photon) excitation and emission lied in the NIR 650-900 nm window, which is an essential criterion for their use in

imaging in vivo. These NPs were proved to efficiently load and release the anticancer drug Dox to the cancer cells, leading to apoptotic cell death. The luminescence of both Au nanoclusters and Dox were found to be useful – Au nanoclusters helped in tracking the uptake of the NPs by the cancer cells; whereas, the luminescence of Dox helped in probing the release of the drug from the NPs. Thus, it can be mentioned that as the NP and the therapeutic drug were luminescent, it was easy to follow them. Interestingly, the properties of the drug loaded NPs like – retention of luminescence in human blood serum over time, suitability of size for possible passive targeting of tumor cells utilizing the EPR effect and ability to be imaged by two-photon laser make them amenable for in vivo imaging. The incorporation of Au nanoclusters in BSA NPs would help in better understanding the pharmacokinetics of the entire albumin NP based delivery vehicles.

6. **Chapter 6** includes the overview of the thesis and future prospects. In brief, I have studied the interaction of binary mixture proteins with Cit-Au NPs resulting in the formation of agglomerates, used modified forms of these agglomerates for the hydrophilic and hydrophobic drug delivery and at last fabricated a nanotheranostic BSA NP having both the fluorescent probe and the therapeutic drug.

   The Au NP-protein agglomerates in future can be used for photodynamic release of drugs. It can even be used for encapsulation and delivery of both the hydrophilic and hydrophobic drugs simultaneously, for increased efficacy and reduced toxicity. A three component system (plasmonic + magnetic + imaging) can also be fabricated by agglomerating Fe_3O_4@Au core-shell NPs with protein-stabilized luminescent nanoclusters.

CHAPTER 2

Signatures of Specificity of Interactions of Binary Protein Mixtures with Citrate-Stabilized Gold Nanoparticles

In this chapter, the specificity of interactions of binary mixtures of proteins with citrate-stabilized gold nanoparticles (Cit-Au NPs), by following the changes in the optical properties of the NPs is reported. The protein mixtures consisted of α-amylase and bovine serum albumin (BSA) or α-amylase and amyloglucosidase (AMG) or glucose oxidase (GOD) and peroxidase (POD). The results observed herein indicated that interaction between a binary protein mixture and Cit-Au NPs depended on the nature and concentration of the component proteins. For example, addition of increasing concentrations of proteins containing α-amylase and BSA consistently broadened the extinction spectrum of Cit-Au NPs. The area under the curves when plotted against the concentration of either of the proteins increased linearly. The method allowed estimation of a protein in a binary mixture, provided the concentration of the other protein is known. FTIR, fluorescence, starch agar plate assay and gel electrophoresis results indicated that both α-amylase and BSA were present in the agglomerated structures of proteins and NPs, indicating role of both the proteins in the association of NPs. On the other hand, when the mixture contained increasing concentration either of α-amylase or AMG, the broadening as well as the change in the area under the curve varied randomly rather than following any linearity. Interestingly, when the mixtures of GOD and POD were used, although broadening was observed but the change in the area was linear only for low concentrations of GOD in the medium and was very sensitive to its concentration. Transmission electron microscopy (TEM) results indicated agglomeration of the NPs in the presence of the protein mixtures as the primary reason behind the optical property change. Our observations indicated that the preferential attachment of one protein to Cit-Au NPs - in presence of the other - primarily depended on the overall charge of the protein in the medium.

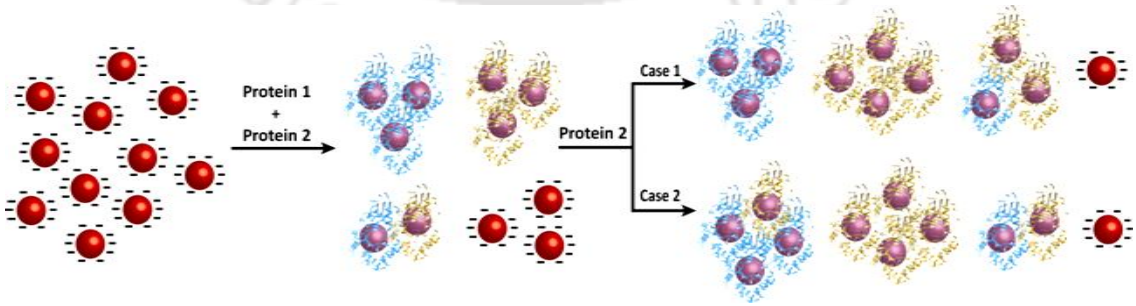

***[Rumi et al. *RSC Adv.* 2012, *2*, 5617–5628] - Reproduced by permission of The Royal Society of Chemistry**
http://pubs.rsc.org/en/Content/ArticleLanding/2012/RA/C2RA20096A#!divAbstract

2.1 Experimental Section

2.1.1 Materials

Proteins α-amylase from porcine pancreas (43.6 U/mg activity), amyloglucosidase from aspergillus niger (AMG, 59.9 U/mg activity) and peroxidase from horse radish (POD, 969.65 U/mg activity) were purchased from Fluka. Glucose oxidase from aspergillus niger (GOD, 158900 U/g activity) and hydrogen tetrachloroaurate trihydrate ($HAuCl_4.3H_2O$) were purchased from Sigma-Aidrich Co., USA. Bovine serum albumin (BSA), trisodium citrate dihydrate and all other reagents required for experiments were obtained from Merck Specialities Pvt. Ltd., India. Milli-Q grade water (>18 MΩ cm, Millipore) was used in all of the experiments.

2.1.2 Synthesis of citrate-stabilized Au NPs (Cit-Au NPs)

1.5 mL of 1.73 x 10^{-2} M $HAuCl_4$ solution was added to 60.0 mL of Milli-Q grade water and then heated to boiling under reflux condition. Then 1.0 mL of 0.857 M trisodium citrate dihydrate solution was added to the above solution (that was being stirred) all at once. The solution first turned blue and then deep red indicating the formation of Cit-Au NP dispersion. The stirring was continued for another 30 min to ensure complete reduction of Au (III) ions. The synthesis of Cit-Au NPs was confirmed by UV-visible and TEM analysis. The dispersion of Cit-Au NPs thus prepared was diluted 2x with sodium phosphate buffer (0.01 M, pH 7.0) so that the maximum extinction was ~ 1.0 and the final pH of Cit-Au NP dispersion was ~ 7.0. It may be mentioned here that treatment of phosphate buffer saline (PBS) with Cit-Au NPs led to broadening of extinction spectrum, indicating possible agglomeration. The same was not the case for using 0.01 M sodium phosphate, which was thus used in all the experiments. This diluted Cit-Au NP dispersion was used for all the experiments and Cit-Au NP dispersion refers to this diluted form hereafter in the chapter. The NP dispersion was diluted just before performing the experiments.

2.1.3 Preparation of protein solution

1.0 mg mL^{-1} solution of each protein, namely α-amylase, BSA, GOD and POD was prepared by dissolving the respective protein in 0.01 M sodium phosphate buffer of pH 7.0. For preparing 1.0 mg mL^{-1} AMG solution, sodium acetate buffer of 0.05 M and pH 4.5 was used. α-amylase being sparingly soluble in phosphate buffer was stirred for 15 min in a magnetic stirrer at room temperature and then centrifuged at 5000 rpm. The supernatant was collected and used for the experiments. Each solution was diluted 10x to obtain 0.1 mg mL^{-1} protein solution. POD and GOD solutions were further diluted 10x with phosphate buffer to obtain 0.01 mg mL^{-1} POD and GOD solutions respectively. The actual protein content in the as-prepared solution for each protein was calculated based on the Bradford test using BSA as the standard protein (refer to **Figure 2A.1**, *Appendix*). The concentration of each protein expressed hereafter in the chapter is thus the actual protein content present in the final NP-protein solution.

2.1.4 UV-visible measurements

For set I of the binary mixture of α-amylase and BSA, the following procedure was followed. 3.0 mL of Cit-Au NP dispersion was taken in a disposable plastic cuvette and its UV-visible spectrum was recorded (using a Hitachi U-2900 Double Beam spectrophotometer). To this 160.0 μL (10.0 μL BSA+10.0 μL α-amylase+140.0 μL sodium phosphate buffer, mixed beforehand in an eppendorf) of binary protein mixture was added drop by drop. The concentrations of BSA and α-amylase were 0.316 μg mL^{-1} and 0.024 μg mL^{-1} respectively in the final solution. The above solution was mixed well and kept for 5 min. UV-visible spectrum was again recorded. Similar additions of the binary protein mixture were made to Cit-Au NPs in separate cuvettes, keeping the BSA volume constant and changing the volume of α-amylase solution (and addition of buffer so as to maintain the final volume of the protein mixture at 160.0 μL).

For sets II, III, IV and V the volumes of BSA were kept constant at 20.0, 40.0, 60.0 and 80.0 μL respectively and the volumes of α-amylase and buffer solutions were changed accordingly (so that the final volume of the added binary protein mixture was 160.0 μL). The final concentrations of BSA for sets I, II, III, IV and V

were 0.316 μg mL^{-1}, 0.633 μg mL^{-1}, 1.266 μg mL^{-1}, 1.899 μg mL^{-1} and 2.532 μg mL^{-1} respectively and that of α-amylase varied from 0.024 μg mL^{-1} to 0.212 μg mL^{-1} (for sets I, II, III, and IV) and from 0.024 μg mL^{-1} to 0.188 μg mL^{-1} (for set V).

In a different set of experiment, the volume of α-amylase was kept constant at 20.0 μL (0.047 μg mL^{-1}) and that of BSA was varied from 10.0 μL to 130.0 μL (0.316 μg mL^{-1} - 4.114 μg mL^{-1}). However, the final volume of the binary protein mixture added to 3.0 mL of Cit-Au NP dispersion was 160.0 μL and this was adjusted using phosphate buffer as mentioned above. The different amounts of BSA and α-amylase solution present in the 160.0 μL binary protein mixture (used in the UV-visible measurements) are mentioned in **Table 2A.1**, *Appendix*.

In case of α-amylase-AMG mixture, the volume of AMG was kept constant at 50.0 μL (0.157 μg mL^{-1}) and that of α-amylase was varied from 10.0 μL to 110.0 μL (0.024 μg mL^{-1} - 0.259 μg mL^{-1}). The final volume of the binary protein mixture (added to 3.0 mL of Cit-Au NP dispersion) was adjusted to 160.0 μL using phosphate buffer. In a different set, the volume of α-amylase was kept constant at 50.0 μL (0.114 μg mL^{-1}) and that of AMG varied from 20.0 μL to 0.2 mL (0.046 μg mL^{-1} - 0.457 μg mL^{-1}). Here the final volume of the binary protein mixture added to 3.0 mL of Cit-Au NP dispersion was adjusted to 250.0 μL with phosphate buffer.

In case of GOD-POD mixture, three different sets of experiments were performed. In set I, the volume of GOD was kept constant at 60.0 μL (0.903 μg mL^{-1}) and that of POD was varied from 10.0 μL to 120.0 μL (0.017 μg mL^{-1} - 0.206 μg mL^{-1}). In set II, the volume of GOD was kept constant at 30.0 μL (0.045 μg mL^{-1}) and that of POD varied from 10.0 μL to 140.0 μL (0.017 μg mL^{-1} - 0.240 μg mL^{-1}). In set III, the volume of POD was kept constant at 20.0 μL (0.034 μg mL^{-1}) and that of GOD varied from 5.0 μL to 160.0 μL (0.008 μg mL^{-1} - 0.241 μg mL^{-1}). For all the three sets, the final volume of the binary protein mixture added to 3.0 mL of Cit-Au NP dispersion was 180.0 μL (volume was appropriately adjusted using phosphate buffer).

For all the above sets, the UV-visible spectra of the Cit-Au NP dispersion before and after addition of binary protein mixture were recorded for each addition and all the experiments were performed in triplicate. Ratio of area under the

extinction spectrum of Cit-Au NPs in presence of proteins to that of Cit-Au NPs only was calculated and plotted against the concentration of a protein in the final NP-protein solution. It may be mentioned here that all the UV-visible spectra were recorded in disposable plastic cuvettes with each cuvette being used for only one measurement.

2.1.5 Calculation of the average area under the UV-visible spectrum

The area under the UV-visible extinction curve was calculated using software which is a part of the operating software of the equipment. The average area (i.e. the area under the extinction curve in between the two wavelengths, divided by the range of wavelength) was calculated by selecting two wavelengths in the extinction spectrum. Further, the ratios of area in presence and absence of proteins were calculated from these average values. For calculating average areas, the extreme wavelengths were always set at 405 nm and 630 nm. A typical view of the total area under the extinction curve is shown in the **Figure 2A.2**, *Appendix*.

2.1.6 Sample preparation for TEM analysis

For TEM analysis, sample was prepared by drop casting the Cit-Au NP dispersion on a carbon-coated copper TEM grid and left overnight for drying. Similarly, samples were prepared with Cit-Au NPs containing six different protein mixtures: 0.071 μg mL^{-1} α-amylase and 0.316 μg mL^{-1} BSA, 0.071 μg mL^{-1} α-amylase and 1.899 μg mL^{-1} BSA, 0.094 μg mL^{-1} α-amylase and 1.266 μg mL^{-1} BSA, 0.118 μg mL^{-1} α-amylase and 0.157 μg mL^{-1} AMG, 0.903 μg mL^{-1} GOD and 0.051 μg mL^{-1} POD and 0.045 μg mL^{-1} GOD and 0.043 μg mL^{-1} POD. These samples were analyzed by a JEOL JEM 2100 TEM operating at a maximum accelerating voltage of 200 kV.

2.1.7 Modes of addition of component proteins to Cit-Au NP dispersion

For combination I of proteins (30.0 μL α-amylase + 20.0 μL BSA + 110.0 μL sodium phosphate buffer) the following three modes of addition of proteins to the Cit-Au NPs were used: α-amylase and BSA as a mixture, α-amylase followed by BSA, and BSA followed by α-amylase. For the first mode of addition, 3.0 mL of Cit-Au NP dispersion was taken in a plastic cuvette and its UV-visible spectrum was

recorded. To this 160.0 μL (30.0 μL α-amylase + 20.0 μL BSA + 110.0 μL buffer, mixed in an eppendorf) of binary protein mixture was added. The concentrations of BSA and α-amylase in the final solution were 0.633 μg mL^{-1} and 0.071 μg mL^{-1} respectively. The above solution was mixed well and kept for 5 min. UV-visible spectrum was again recorded and the ratio of area of the final solution to the area of the Cit-Au NP dispersion was calculated. For second mode of addition, a mixture of 30.0 μL of α-amylase and 110.0 μL of buffer was added to 3.0 mL of Cit-Au NP dispersion in a plastic cuvette, mixed well, followed by the addition of 20.0 μL of BSA, they were mixed again and kept for 5 min. The UV-visible spectrum of the Cit-Au NP dispersion was recorded before and after addition of the proteins and the ratio of area of the final solution to the area of the Cit-Au NP dispersion was noted. For third mode, the order of addition of α-amylase and BSA was reversed, keeping the other conditions same. For combination II, the volumes of α-amylase and BSA were changed to 50.0 μL (0.118 μg mL^{-1}) and 60.0 μL (1.899 μg mL^{-1}) respectively in 160.0 μL binary protein mixture. All the three modes of protein addition as discussed for combination I were followed.

For combination III, the mixture of 50.0 μL α-amylase (0.118 μg mL^{-1}), 50.0 μL AMG (0.157 μg mL^{-1}) and 60.0 μL phosphate buffer was used. Three modes of addition of binary proteins to Cit-Au NPs were also applied here: α-amylase and AMG as a mixture, α-amylase followed by AMG and AMG followed by α-amylase.

For combination IV, the mixture of 30.0 μL (0.045 μg mL^{-1}) GOD, 25.0 μL (0.043 μg mL^{-1}) POD and 125.0 μL phosphate buffer was used. Three modes of addition of proteins applied were: GOD and POD as a mixture, GOD followed by POD and POD followed by GOD. All the experiments were performed in triplicates.

2.1.8 Sodium dodecyl sulphate polyacrylamide gel electrophoresis (SDS-PAGE) analysis

A mixture of 2.8 mL of 7.4 μg mL^{-1} α-amylase, 1.6 mL of 0.1 mg mL^{-1} BSA, and 2.0 mL of sodium phosphate buffer was added to 120.0 mL of Cit-Au NP dispersion, mixed well and kept for 5 min. The final concentrations of α-amylase and BSA were 0.165 μg mL^{-1} and 1.266 μg mL^{-1} respectively. The above solution was centrifuged at 22000 rpm and 4 °C for 30 min. The supernatant was discarded and

the pellet was re-suspended in sodium phosphate buffer. The NP-protein composite was recovered again by centrifugation under the same conditions. The composite was re-suspended in 150.0 μL of phosphate buffer. Protein loading buffer (final 1x concentration) was added to each of NP-protein solution, 0.074 mg mL^{-1} α-amylase solution, 0.1 mg mL^{-1} BSA solution, Cit-Au NP dispersion, and protein molecular weight marker (14.3 kDa – 97.4 kDa, Bangalore Genei). These solutions were boiled for 5 min and an equal volume was loaded in 12 % polyacrylamide gel. Gel electrophoresis was performed at 100V for about 2 hours, until the dye front reached at the end of the gel. The gel was stained using silver staining method and then photographed.

2.1.9 Enzymatic assay of α-amylase

Starch agar solution (3 %) was prepared in Milli-Q grade water, autoclaved, and poured into a petri plate. After solidification of agar, five distinct wells were punctured into the agar plate and filled with 200 μL of sodium phosphate buffer, 7.4 μg mL^{-1} α-amylase solution, 0.1 mg mL^{-1} BSA solution, Cit-Au NPs only, and NP-protein composite (having the same concentration as in SDS-PAGE) respectively. The plate was incubated at 37 °C overnight and α-amylase activity was tested by flooding the plate with iodine solution and observing zone of clearance around the wells. The same experiment was also repeated with three different combinations of α-amylase and BSA. The concentrations of α-amylase and BSA used were 1.266 μg mL^{-1} BSA and 0.094 μg mL^{-1} α-amylase, 1.266 μg mL^{-1} BSA and 0.165 μg mL^{-1} α-amylase and 1.2666 μg mL^{-1} BSA and 0.235 μg mL^{-1} α-amylase.

2.1.10 Fluorescence measurements

3.0 mL of sodium phosphate buffer solution was taken in a fluorescence cuvette and to it 160.0 μL (50.0 μL α-amylase + 50.0 μL BSA + 60.0 μL buffer) of binary protein mixture was added and its emission spectrum was recorded using a Fluoromax 4 spectrofluorometer with a xenon lamp. The concentrations of BSA and α-amylase in the final solution were 1.582 μg mL^{-1} and 0.118 μg mL^{-1} respectively. Excitation wavelength was set at 280 nm. The excitation and emission slit widths were fixed at 5 nm. Similarly, the emission spectrum of 160.0

μL of the above mentioned binary mixture of proteins in the presence of 3.0 mL of Cit-Au NP dispersion was recorded, the protein mixture being added drop wise to the Cit-Au NPs. Before recording the spectrum the sample was mixed well and left for 5 min. The emission spectra of the above mentioned binary protein mixture were also recorded in presence of 3.0 mL Cit-Au NPs following the addition of the individual proteins one after the other (rather than mixing them together before addition). In one case α-amylase was added before BSA and in another case the order of addition was reversed. The emission spectrum of 0.118 μg mL^{-1} α-amylase in presence of 3.0 mL Cit-Au NP dispersion was recorded and compared with its emission spectrum in absence of Cit-Au NPs (i.e. in buffer only). Similarly emission spectra of 1.582 μg mL^{-1} BSA in presence and absence of 3.0 mL Cit-Au NP dispersion were recorded. The above mentioned binary mixture of proteins was added drop wise to 3.0 mL of Cit-Au NP dispersion and the time-dependent fluorescence measurement was made. Spectra were recorded after 1, 3, 5, and 10 min from the time of addition of binary mixture of proteins to Cit-Au NP dispersion.

2.1.11 Sample preparation for FTIR measurements

The dispersion of Cit-Au NPs containing 0.118 μg mL^{-1} α-amylase and 1.899 μg mL^{-1} BSA was centrifuged at 22000 rpm and 4 °C for 30 min. The supernatant was discarded and the pellet was lyophilized (using Christ Alpha 1-4 LD lyophilizer). Dispersion of Cit-Au NP only was also lyophilized after centrifugation. The lyophilized products were analyzed by FTIR. FTIR spectra of trisodium citrate dihydrate, α-amylase, BSA, and the above lyophilized products were recorded, by forming disc with KBr, using a Perkin Elmer Spectrum One Spectrometer. The scan was performed in the range of 400-4000 cm^{-1} in transmittance mode.

2.1.12 Dynamic light scattering (DLS)-based particle size measurements

DLS measurements were carried out for GOD and POD mixture. Cit-Au NP dispersion was taken in a quartz cuvette and its particle size distribution was measured using a Zetasizer Nano ZS90 (Model No ZEN3690). To this mixture 0.045 μg mL^{-1} GOD and 0.017 μg mL^{-1} POD was added, mixed well and kept for 5 min. The particle size distribution of this solution was recorded again. Similar

addition of GOD and POD binary mixture were made to fresh Cit-Au NPs keeping the concentration of GOD constant and varying the concentration of POD from 0.017 μg mL^{-1} to 0.240 μg mL^{-1}. In a different set the concentration of GOD was fixed at 0.903 μg mL^{-1} and POD was varied from 0.017 μg mL^{-1} to 0.206 μg mL^{-1}. The particle size distribution was recorded after the addition of each binary mixture to Cit-Au NP dispersion. Measurements were carried out at 25 °C using a sample volume of 1.5 mL. Each sample was measured in duplicate and the wavelength of the HeNe laser used for the DLS instrument was 633 nm.

2.2 Results and Discussion

It is known that addition of proteins like α-amylase or BSA to a dispersion of Cit-Au NP leads to agglomeration of the NPs, which is accompanied by broadening of the UV-visible extinction spectrum.[67] Also, the area under the extinction curve varies linearly with the concentration of the protein when the concentration is sufficiently small. On the other hand, the slope of the curve varies depending on the nature of the protein and its conformation (native versus denatured). A natural extension of this idea would be to elucidate the effect of a binary mixture of proteins on the NPs. The results reported here points out interesting consequences depending on the nature of the proteins and their concentrations in the mixture. For example, upon addition of α-amylase and BSA mixture to Cit-Au NPs, the deep red color of the dispersion changed to pink at low total protein concentration. The color changed to purple when the total concentration of proteins was increased. There were observable changes in the surface plasmon resonance (SPR) extinction spectrum of Cit-Au NPs in the presence of mixture of α-amylase and BSA. UV-visible spectra of Cit-Au NPs in absence and presence of binary mixture of proteins (having different fractional content of α-amylase and BSA) are shown in **Figure 2.1**. Quantitatively, when a mixture of 0.316 μg mL^{-1} BSA and 0.024 μg mL^{-1} α-amylase was added to 3.0 mL of Cit-Au NP dispersion, the spectrum broadened with a slight red shift from 522 nm to 524 nm in the SPR peak of Cit-Au NPs. The broadening increased further upon increasing the concentration of α-amylase (up until 0.165 μg mL^{-1} of protein), while keeping the

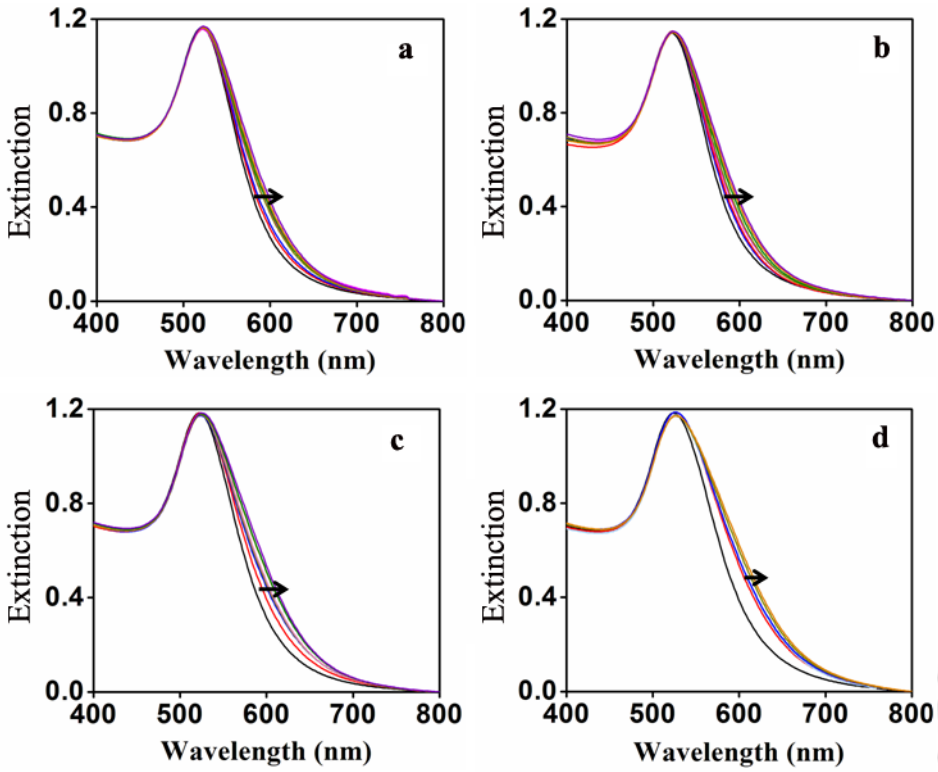

Figure 2.1 SPR extinction spectra of Cit-Au NP dispersion before and after addition of binary protein mixtures having different fractional content of α-amylase and BSA. Concentration of α-amylase was varied in the range of 0.024 μg mL^{-1} - 0.165 μg mL^{-1} (for a-c) and from 0.024 μg mL^{-1} - 0.118 μg mL^{-1} (for d), keeping the concentration of BSA constant at (a) 0.316 μg mL^{-1}, (b) 0.633 μg mL^{-1}, (c) 1.266 μg mL^{-1} and (d) 1.899 μg mL^{-1}. The arrows in the figures show the increase in broadening of the SPR spectrum of Cit-Au NPs with increasing concentration of α-amylase.

concentration of BSA constant at 0.316 μg mL^{-1}. At a concentration of α-amylase higher than 0.165 μg mL^{-1}, no further broadening of the SPR peak was observed. Also, when keeping the concentration of BSA constant at 0.633 μg mL^{-1} and changing the concentration of α-amylase, broadening of the SPR peak of Cit-Au NP dispersion was observed to increase and further spectral broadening was no longer observed beyond a concentration of 0.165 μg mL^{-1} α-amylase. When the concentration of BSA was kept constant at 1.266 μg mL^{-1} and 1.899 μg mL^{-1}, saturation occurred after addition of 0.165 μg mL^{-1} and 0.118 μg mL^{-1} α-amylase respectively. However, when the concentration of BSA was kept constant at 2.532 μg mL^{-1} and that of α-amylase was changed from 0.024 μg mL^{-1} - 0.188 μg mL^{-1}, broadening increased systematically up to a concentration of 0.071 μg mL^{-1} α-amylase only and beyond that the change in broadening was not systematic

(**Figure 2A.3**, *Appendix*). On the other hand, when the concentration of α-amylase was kept constant at 0.047 μg mL^{-1} and that of BSA was varied from 0.316 μg mL^{-1} to 4.114 μg mL^{-1} in the Cit-Au NP dispersion, then also broadening of the SPR peak of Cit-Au NPs increased (up to a BSA concentration of 2.215 μg mL^{-1}) (**Figure 2.2**). At a concentration of BSA higher than 2.215 μg mL^{-1}, saturation occurred and no further increase in broadening was observed.

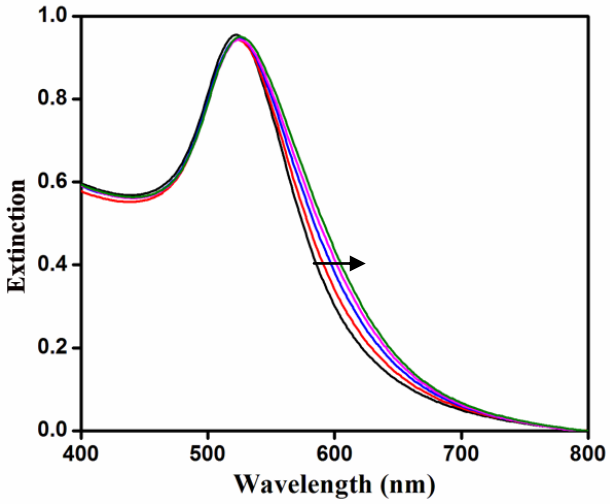

Figure 2.2 SPR spectra of Cit-Au NP dispersion before and after addition of binary protein mixtures having different fractional content of α-amylase and BSA. Concentration of BSA was varied from 0.316 μg mL^{-1} to 2.215 μg mL^{-1}, keeping the concentration of α-amylase constant at 0.047 μg mL^{-1}. The arrow in the figure shows the increase in broadening of the SPR spectrum of Cit-Au NPs with increasing concentration of BSA.

Further, when the α-amylase-AMG mixtures having constant concentration of AMG (0.157 μg mL^{-1}) and varying concentration of α-amylase (0.024 μg mL^{-1} to 0.259 μg mL^{-1}) were added to Cit-Au NP dispersion, broadening was also observed. However with an increase in concentration of α-amylase, there was no consistent change in broadening (**Figure 2.3**). For example, when 0.047 μg mL^{-1} of α-amylase was present in the mixture the spectrum was broadened; whereas when the mixture contained 0.071 μg mL^{-1} of α-amylase there was broadening but less than that in presence of 0.047 μg mL^{-1}. On the other hand, when 0.094 μg mL^{-1} α-amylase containing protein mixture was added to the dispersion then there was broadening again and that was higher than that in presence of 0.047 μg mL^{-1}. Further, when the concentration of α-amylase was kept constant at 0.114 μg

mL^{-1} and that of AMG was varied from 0.046 μg mL^{-1} - 0.457 μg mL^{-1} results were similar.

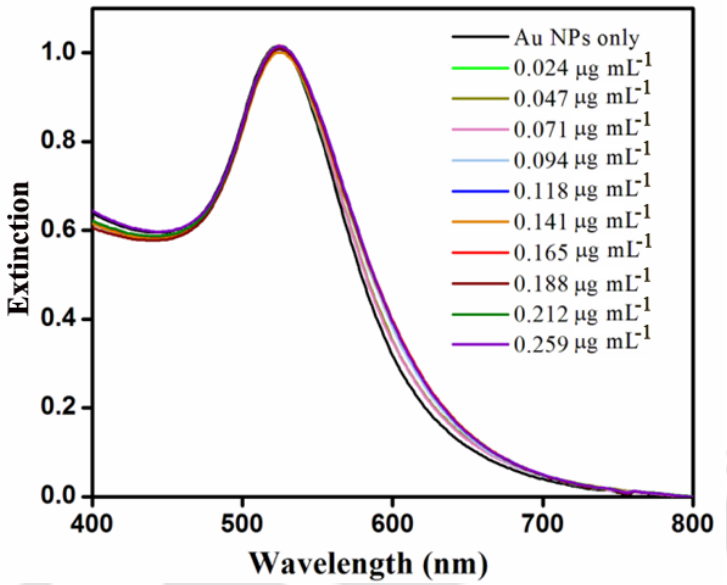

Figure 2.3 SPR spectra of Cit-Au NP dispersion before and after addition of binary protein mixtures having different fractional content of α-amylase and AMG. Concentration of α-amylase was varied from 0.024 μg mL^{-1} to 0.259 μg mL^{-1} (the legends refer to different concentrations), keeping the concentration of AMG constant at 0.157 μg mL^{-1}.

On the other hand, the results with respect to a mixture of GOD and POD were dependent on the concentration of GOD. For example, when a mixture of 0.903 μg mL^{-1} GOD and 0.017 μg mL^{-1} POD was added to Cit-Au NP dispersion, broadening of the SPR peak was observed. However, with increase in concentration of POD, the broadening was observed not to change consistently (**Figure 2.4 a**). For example, when 0.017 μg mL^{-1} of POD was present in the mixture the spectrum was broadened; whereas when the mixture contained 0.034 μg mL^{-1} of POD there was broadening but less than that in presence of 0.017 μg mL^{-1}. On the other hand, when 0.051 μg mL^{-1} POD containing protein mixture was added to the dispersion then there was broadening again, which was higher than that in presence of 0.017 μg mL^{-1}. Interestingly, when the concentration of GOD was fixed at 0.045 μg mL^{-1} (lower than the sensitivity range of individual GOD; see the discussion below) and that of POD was varied, broadening was observed to increase consistently with an increase in concentration (up to 0.146 μg mL^{-1}) of POD (shown in **Figure 2.4 b**).

However, when the concentration of POD was kept constant at 0.034 μg mL^{-1} and that of GOD was varied from 0.008 μg mL^{-1} - 0.241 μg mL^{-1}, no systematic change in broadening was observed.

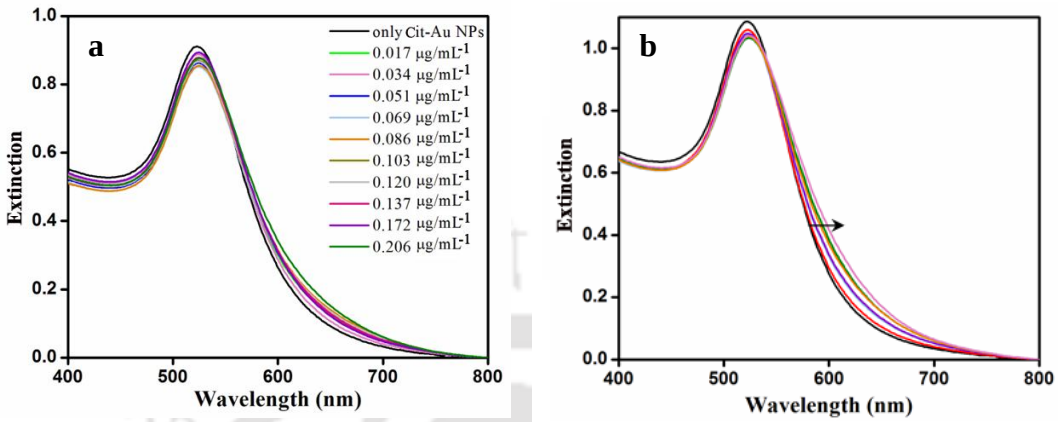

Figure 2.4 SPR spectra of Cit-Au NP dispersion before and after addition of binary protein mixtures having different fractional content of GOD and POD. Concentration of POD was varied from 0.017 μg mL^{-1} - 0.206 μg mL^{-1} (for a) and from 0.017 μg mL^{-1} - 0.146 μg mL^{-1} (for b), keeping the concentration of GOD constant at (a) 0.903 μg mL^{-1} and (b) 0.045 μg mL^{-1}.

TEM investigations of the Cit-Au NPs in the presence of mixtures of proteins indicated that the origin of the spectral broadening may be attributed to the agglomerations of the NPs. It may be mentioned here that TEM of the as-synthesized Cit-Au NPs (i.e. in absence of protein) indicated no such agglomeration and the particle size distribution of Cit-Au NPs was found to be 10.0 ± 1.0 nm (**Figure 2.5**). On the other hand, Cit-Au NPs in presence of mixtures

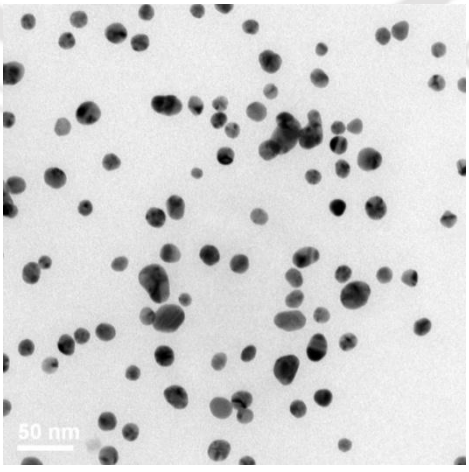

Figure 2.5 TEM micrograph of Cit-Au NPs. Scale bar is 50 nm.

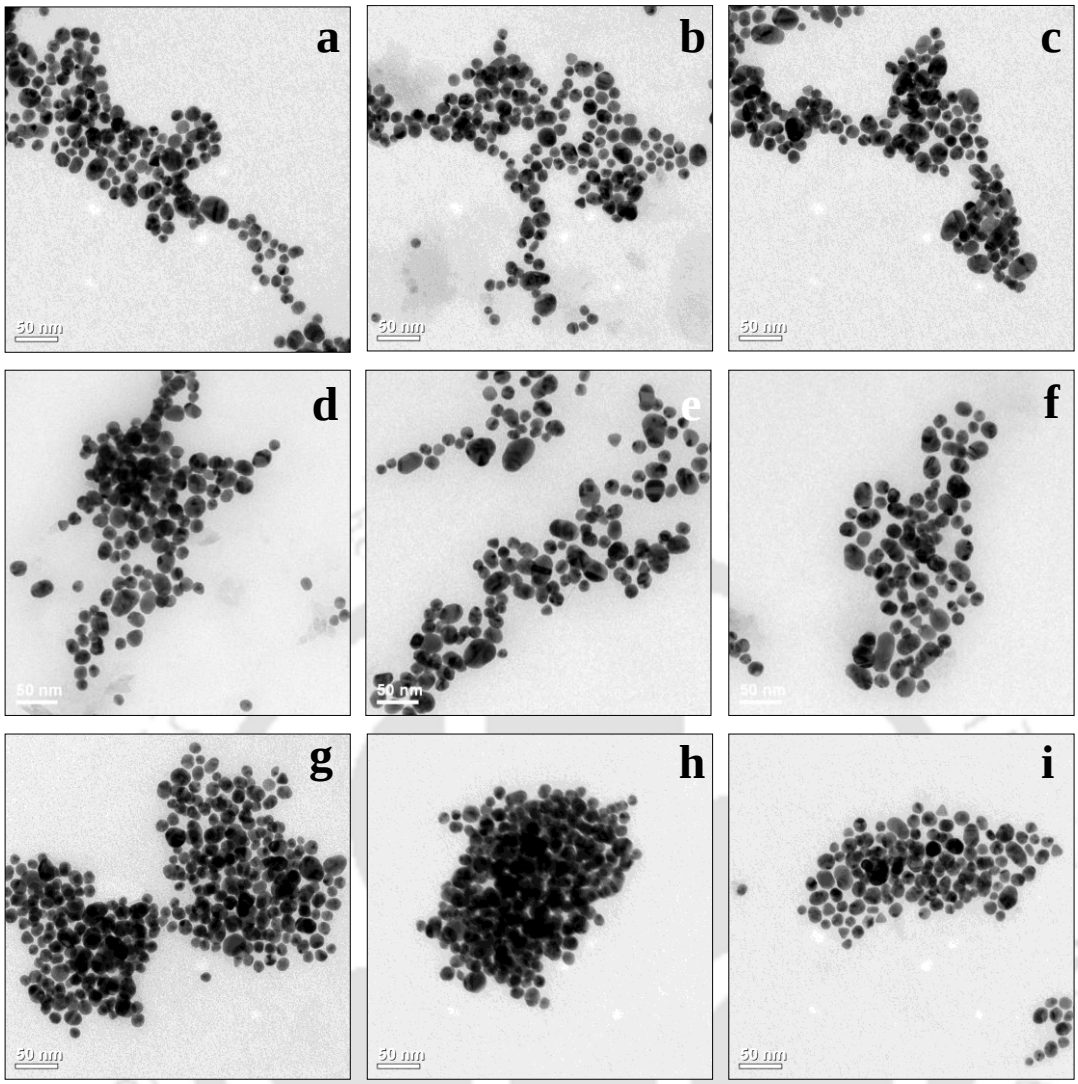

Figure 2.6 TEM micrographs of (a-c) Cit-Au NPs in presence of 0.071 μg mL^{-1} α-amylase and 0.316 μg mL^{-1} BSA, (d-f) Cit-Au NPs in presence of 0.071 μg mL^{-1} α-amylase and 1.899 μg mL^{-1} BSA and (g-i) Cit-Au NPs in presence of 0.094 μg mL^{-1} α-amylase and 1.266 μg mL^{-1} BSA. Scale bar is 50 nm in all.

of mixtures of 0.071 μg mL^{-1} α-amylase and 0.316 μg mL^{-1} BSA (**Figure 2.6 a-c**), 0.071 μg mL^{-1} α-amylase and 1.899 μg mL^{-1} BSA (**Figure 2.6 d-f**), 0.094 μg mL^{-1} α-amylase and 1.266 μg mL^{-1} BSA (**Figure 2.6 g-i**), 0.118 μg mL^{-1} α-amylase and 0.157 μg mL^{-1} AMG (**Figure 2.7 a-c**), and 0.045 μg mL^{-1} GOD and 0.043 μg mL^{-1} POD (**Figure 2.7 d-f**) exhibited significant agglomeration of the NPs. Interestingly, when mixture of 0.903 μg mL^{-1} GOD and 0.051 μg mL^{-1} POD was added to Cit-Au NP dispersion agglomeration was present but less significant (shown in **Figure 2.7 g-i**). This indicates that an increase in the concentration of GOD (in the presence of POD) in the solution led to a lowering of the extent of NP

agglomeration. Thus, the presence of the mixture of proteins in the dispersion of Cit-Au NP led to agglomeration of the NPs which caused the broadening of the extinction spectrum. Further, the extent of the broadening of the spectrum and agglomeration of the NPs were dependent not only on the nature of the protein but also on their content in the mixture.

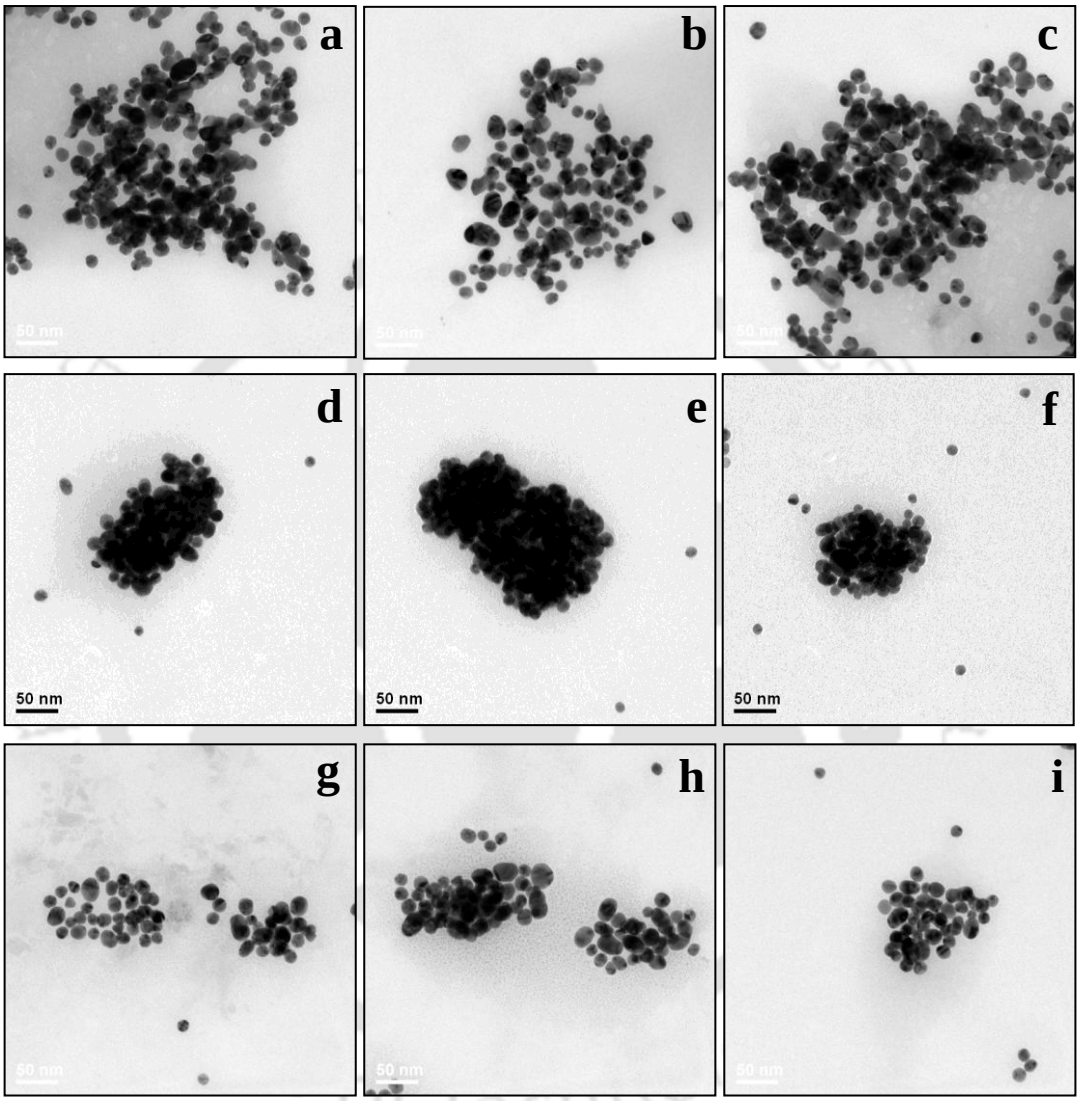

Figure 2.7 TEM micrographs of (a-c) Cit-Au NPs in presence of mixture of 0.118 μg mL^{-1} α-amylase and 0.157 μg mL^{-1} AMG, (d-f) Cit-Au NPs in presence of mixture of 0.045 μg mL^{-1} GOD and 0.043 μg mL^{-1} POD and (g-i) Cit-Au NPs in presence of mixture of 0.903 μg mL^{-1} GOD and 0.051 μg mL^{-1} POD. Scale bar is 50 nm in all.

It has previously been observed that a more quantitative understanding of the interaction between proteins and Cit-Au NPs could be achieved if the area under the extinction curve (related to oscillator strength) was plotted against the concentration of protein.[67] This turned out to be quite useful for assay of

individual proteins with distinction of conformations. It can be expected that similar analyses would throw new light on the interactions of proteins and NPs in the presence of a second protein. The results of such analyses involving a binary mixture of α-amylase and BSA are shown in **Figure 2.8**. The ratio of the area under the curve in the presence of a particular mixture of proteins to that in their absence was plotted against the concentration of a particular protein, while keeping the other one constant. The concentration range of component proteins was chosen preferably from the linear region of area under the extinction curve

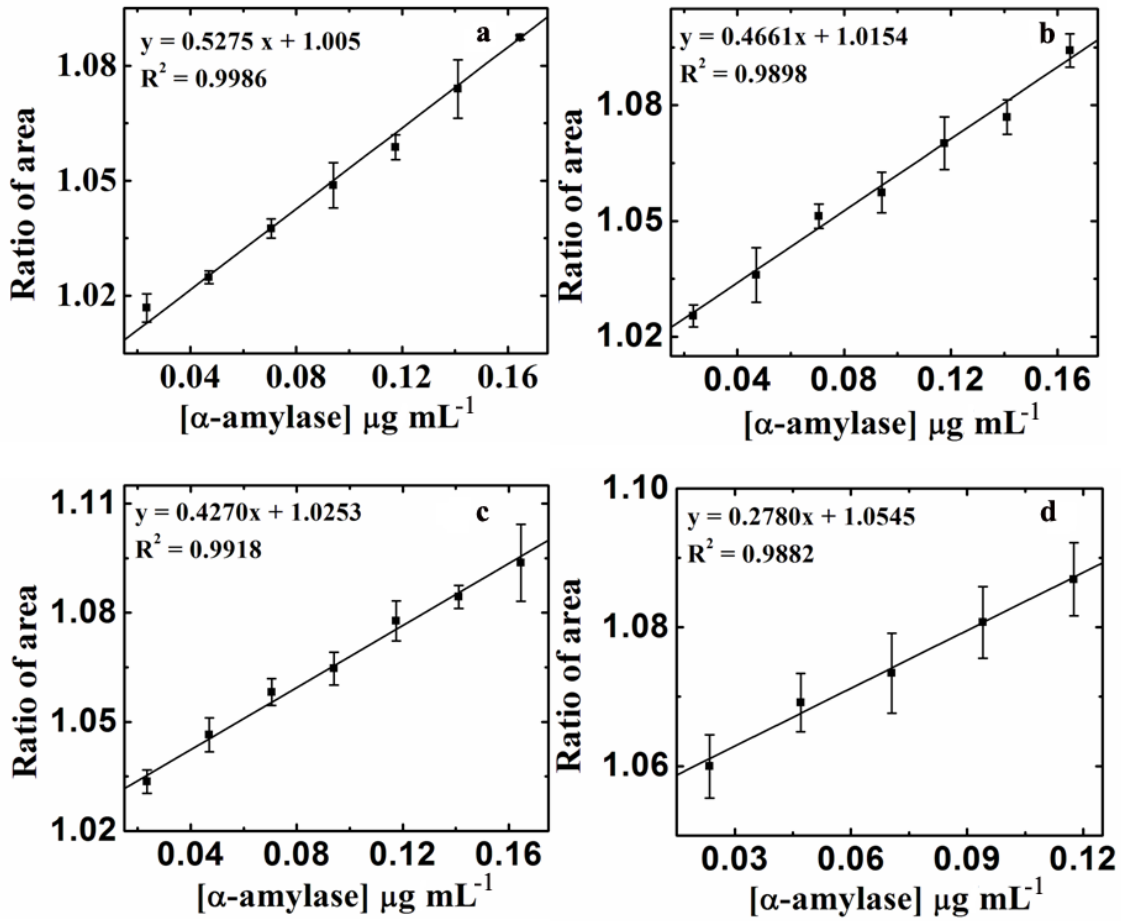

Figure 2.8 Ratio of area under the UV-visible spectrum of Cit-Au NPs in presence of different fractional content of α-amylase and BSA to that of Cit-Au NPs only, plotted against α-amylase concentration (μg mL^{-1}). The areas were calculated based on the results in Figure 2.1. Concentration of α-amylase was varied keeping the concentration of BSA constant in the final solution. Concentrations of BSA were (A) 0.316 μg mL^{-1}, (B) 0.633 μg mL^{-1}, (C) 1.266 μg mL^{-1} and (D) 1.899 μg mL^{-1}. The error bars were calculated from the results of three independent experiments.

versus concentration plot, obtained from the spectra when individual proteins were added to Cit-Au NPs.[67] It is interesting to observe that the ratio of the area under the UV-visible spectrum of Cit-Au NPs (in the presence of a binary mixture of α-amylase and BSA) to that of Cit-Au NPs only, increased linearly with the increase in concentration of one of the component proteins (until a certain concentration). For example, when the concentration of BSA was kept constant at 0.316 μg mL^{-1}, linearity was observed for the change in concentration of α-amylase from 0.024 μg mL^{-1} to 0.165 μg mL^{-1} (**Figure 2.8 a**). Additionally, for constant concentrations of BSA being 0.633 μg mL^{-1}, 1.266 μg mL^{-1} and 1.899 μg mL^{-1}, linearity was observed from 0.024 μg mL^{-1} up to 0.165 μg mL^{-1}, 0.165 μg mL^{-1} and 0.118 μg mL^{-1} of α-amylase concentration respectively (**Figure 2.8 b-d**). The plot of ratio of area versus α-amylase concentration (μg mL^{-1}), when the concentration of BSA was kept constant at 2.532 μg mL^{-1} is shown in **Figure 2A.4**, *Appendix*. At this concentration of BSA, the linearity was observed up to an α-amylase concentration of 0.071 μg mL^{-1}. However at higher concentrations – while broadening was significant – clear linearity with an increase in concentration of α-amylase was not apparent (**Figure 2A.4**, *Appendix*). On the other hand, when the α-amylase concentration was fixed at 0.047 μg mL^{-1} and that of BSA was varied, then linearity was also observed for changes in concentration of BSA from 0.316 μg mL^{-1} - 2.215 μg mL^{-1} (**Figure 2.9**). At several other concentrations of α-amylase, the linearity was maintained with respect to increases in the concentration of BSA. A three-dimensional representation of the results of areas of the extinction spectra of Cit-Au NPs in the presence of binary mixtures of α-amylase and BSA is depicted in **Figure 2.10**. Clearly the figure indicates that the area ratio was linear in the concentration range of α-amylase being 0.024 μg mL^{-1} to 0.165 μg mL^{-1}, while that of BSA was from 0.316 μg mL^{-1} to 1.899 μg mL^{-1}. A schematic representation of the process of agglomeration of the NPs in the presence of a binary mixture of α-amylase and BSA is shown in **Scheme 2.1 b** (Case 1). An important point that needs to be noted here is the concentration of individual protein at which agglomerates formed. It was observed that even in the mixture the concentration of α-amylase required for agglomeration was less in

comparison to that of BSA. Earlier works from our laboratory indicated that when only α-amylase was used the concentration of the protein required for

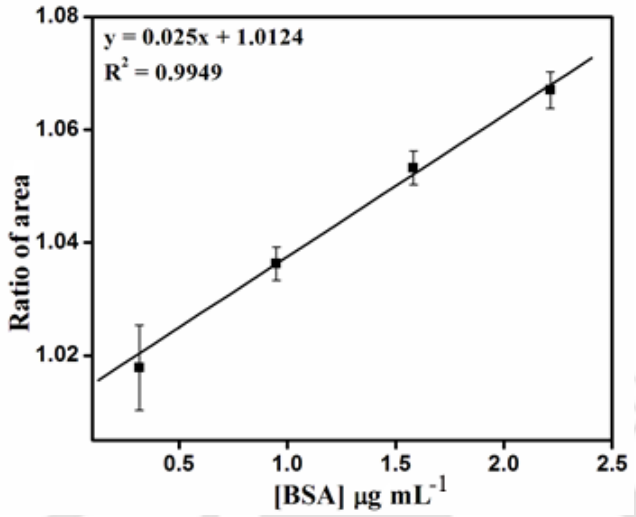

Figure 2.9 Ratio of area under the UV-visible spectrum of Cit-Au NPs in presence of different fractional content of α-amylase and BSA to that of Cit-Au NPs only plotted against BSA concentration (μg mL^{-1}). Concentration of BSA was varied from 0.316 μg mL^{-1} to 2.215 μg mL^{-1}, keeping the concentration of α-amylase constant at 0.047 μg mL^{-1}. The error bars were calculated from the results of three independent experiments.

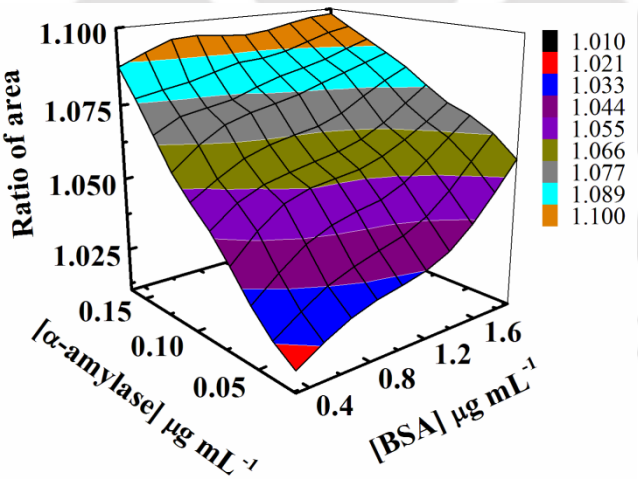

Figure 2.10 Three-dimensional plot of ratio of area as a function of α-amylase concentration (μg mL^{-1}) in x-axis and BSA concentration in y-axis (μg mL^{-1}).

agglomeration was less in comparison to that when only BSA was used.[67] Thus the trend in concentration-dependent agglomeration in the binary mixture was commensurate with the behavior in the presence of individual proteins. Further, the linear increase in area under the extinction curve with concentration of either

of the proteins indicated that this could be a facile method for estimation of proteins in a binary mixture at least when the concentration of one is known.

Further, the results from the study involving α-amylase and AMG mixtures did not clearly exhibit linearity in the increase in area, under the extinction spectrum, with concentration of either of the proteins. As an example, for a mixture of α-amylase and AMG where the concentration of AMG was fixed at 0.157 μg mL^{-1} and that of α-amylase was varied from 0.024 μg mL^{-1} to 0.259 μg mL^{-1}, the ratio of area under the UV-visible spectrum of Cit-Au NPs and proteins solution to that of Cit-Au NPs only did not change linearly with increase in concentration of α-amylase (**Figure 2.11**). Additionally, when the concentration of α-amylase was kept constant at 0.114 μg mL^{-1} and that of AMG varied from 0.046 μg mL^{-1} - 0.457 μg mL^{-1} results were similar.

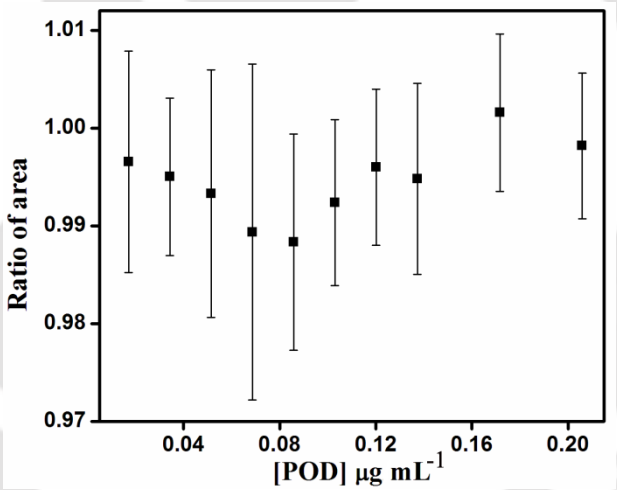

Figure 2.11 Ratio of area under the UV-visible spectrum of Cit-Au NPs in presence of different fractional content of α-amylase and AMG to that of Cit-Au NPs only plotted against α-amylase concentration (μg mL^{-1}). Concentration of α-amylase was varied from 0.024 μg mL^{-1} to 0.259 μg mL^{-1}, keeping the concentration of AMG constant at 0.157 μg mL^{-1}. The error bars were calculated from the results of three independent experiments.

In case of GOD-POD mixture when the concentration of GOD was kept constant at 0.903 μg mL^{-1} and that of POD varied from 0.017 μg mL^{-1} - 0.206 μg mL^{-1}, the change in the ratio of area versus POD concentration was not linear (**Figure 2.12 a**). However, when changing the concentration of GOD to 0.045 μg mL^{-1} (which is lower than the sensitivity range of individual GOD; see the discussion below) and then varying the concentration of POD, a linear increase in the ratio of area was

observed in the concentration range 0.017 μg mL^{-1} - 0.146 μg mL^{-1} of POD (**Figure 2.12 b**). Interestingly, when the concentration of POD was kept constant at 0.034 μg mL^{-1} and that of GOD varied from 0.008 μg mL^{-1} - 0.241 μg mL^{-1}, again no linearity was observed. The results indicated that linearity was maintained at a low concentration of GOD in the solution. The processes of agglomeration in case of α-amylase – AMG (Case 2) and GOD – POD (Case 1, at low GOD concentration and Case 2, at high GOD concentration) mixtures are depicted in **Scheme 2.1 b**.

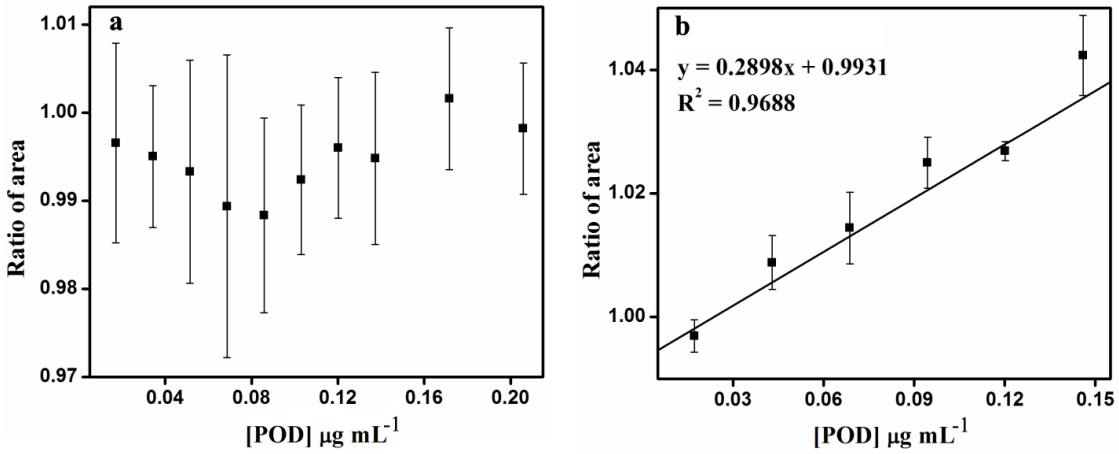

Figure 2.12 Ratio of area under the UV-visible spectrum of Cit-Au NPs in presence of different fractional content of GOD and POD to that of Cit-Au NPs only plotted against POD concentration (μg mL^{-1}). Concentration of POD was varied from 0.017 μg mL^{-1} - 0.206 μg mL^{-1} (for a) and from 0.017 μg mL^{-1} - 0.146 μg mL^{-1} (for b), keeping the concentration of GOD constant at (a) 0.903 μg mL^{-1} and (b) 0.045 μg mL^{-1}. The error bars were calculated from the results of three independent experiments.

Further, DLS-based particle size analysis indicated that for Cit-Au NPs, the maximum of the particle size distribution curve was at 18 nm. In the presence of a low concentration GOD (0.045 μg mL^{-1}), when POD was added increasingly from 0.045 μg mL^{-1} to 0.240 μg mL^{-1}, the maximum gradually shifted from 22 nm to 37 nm (**Figure 2A.5 a**, *Appendix*). A closer analysis of the distribution curves (shown in **Figure 2A.5 b**, *Appendix*) revealed that upon addition of binary protein mixtures (GOD and POD) to Cit-Au NPs, the number of particles in the region 9 nm – 24 nm decreased whereas the number of particles in the region 24 nm – 72 nm increased, indicating association of particles to form agglomerated structures. Moreover, significant peaks at higher sizes (166 nm – 4936 nm) appeared on addition of the proteins. On the other hand, at a higher concentration of GOD,

when POD amount was increased from 0.017 μg mL^{-1} to 0.206 μg mL^{-1}, the number of smaller particles decreased and that of larger particles increased. However, the maxima of the distribution curves did not vary consistently. For example, in the presence of 0.903 μg mL^{-1} of GOD when 0.017 μg mL^{-1}, 0.086 μg mL^{-1} and 0.120 μg mL^{-1} of POD were added the maxima of the distribution curves were at 28 nm, 24 nm and 28 nm respectively. In general the maximum of the particle size distribution curves varied between 28 nm and 24 nm; however, the changes were not consistent with the protein concentrations (shown in **Figure 2A.6 a**, *Appendix*). Peaks corresponding to higher particle size distribution also appeared (shown in **Figure 2A.6 b**, *Appendix*); and their behaviors were similar. The results indicated that in the presence of higher concentration of GOD, addition of POD changed the particle sizes but there was no simple correlation between them. In other words, although there were agglomerations they did not follow any simple behaviour. Moreover, in the presence of one protein the assay sensitivity of the second protein in the mixture could be improved in the case where linearity is observed. For example, as shown in **Figure 2A.7 and Figure 2A.8**, *Appendix*, the sensitivity of detection of POD and GOD (in their individual protein solutions) could be as low as 0.009 μg mL^{-1} and 1.091 μg mL^{-1} respectively. On the other hand, in the presence of a binary mixture of them the sensitivity of detection of GOD could be even higher with a value as low as 0.045 μg mL^{-1}. Thus, this indicates an additional advantage of assay of binary protein mixture with improved sensitivity which may otherwise be not feasible using a single protein in the current method.

It has been demonstrated that proteins upon attachment with the NPs get unfolded and interact with excess proteins in the solution leading to agglomeration.[59] The interactions between colloidal particles in a medium have traditionally been addressed by DLVO theory.[96] In this case the Coulombic forces and van der Waals interactions play major roles in the stability as well as agglomeration behaviors of the colloids. On the other hand, it has been reported lately that in the presence of high salt concentrations, i.e. 0.1 M or higher, the DLVO theory fails to explain the stability and agglomeration behaviors of colloidal particles.[97] In the present case, a clearer understanding of the phenomena based

on DLVO theory may not be easy, as the concentration of citrate and other salts are rather high (6.5 M). The agglomeration of the NPs in the presence of proteins could be due to a combination of electrostatic and van der Waals interactions, hydrogen bonding, steric, entropic and hydrophobic interactions (following unfolding of proteins attached to the NPs). A clear and quantitative understanding of these forces is out of bound of the present context as the focus here is on the consequences of aggregation rather than its origin. Thus we shall restrict our conclusions based on a more qualitative analysis of the effect of agglomeration.

Considering the observations described above it can be speculated that when a binary mixture of proteins interacts with Cit-Au NPs, the composites of the NPs and proteins could form structures with three different kinds of components molecules (as depicted in **Scheme 2.1 b**) – Au NPs plus protein 1 (*P1*), Au NPs plus protein 2 (*P2*) and Au NPs plus *P1* and *P2*. Each of these aggregates would contribute to the broadening of the spectrum. The contribution of each of the aggregate to the overall broadening could be accounted for by invoking the broadening (and accompanying shift in the peak position) of the spectral line for each constituents. For a colloidal solution with N particles per unit volume the extinction of light could be written as follows:[98]

$$A = \log_{10}\frac{I_O}{I} = \frac{NQ_{ext}l}{2.303} \qquad (2.1)$$

Here I_O and I are the intensities of incident and transmitted light, l is the path length and Q_{ext} is the extinction coefficient of a single particle.

$$Q_{ext}(\lambda) = \frac{8\pi^2 R^3 \sqrt{\varepsilon_m}}{\lambda} \mathrm{Im}\left\{\frac{(\varepsilon_2 - \varepsilon_m)(\varepsilon_1 + 2\varepsilon_2) + (1-g)(\varepsilon_1 - \varepsilon_2)(\varepsilon_m + 2\varepsilon_2)}{(\varepsilon_2 + 2\varepsilon_m)(\varepsilon_1 + 2\varepsilon_2) + (1-g)(\varepsilon_1 - \varepsilon_2)(2\varepsilon_2 - 2\varepsilon_m)}\right\} \qquad (2.2)$$

Here R is the radius of the spherical NP, λ is the wavelength of the light, ε_m is the dielectric function of the medium, ε_1 and ε_2 are the complex dielectric functions of the particle core and the surface coating and g is the volume fraction occupied by the surface coating. The extinction of light integrated over wavelengths (i.e. the area under the extinction curve) could be expressed as,

$$\int A_{total}(\lambda)d\lambda = \int A_{NP}(\lambda)d\lambda + \int A_{P1}(\lambda)d\lambda + \int A_{P2}(\lambda)d\lambda + \int A_{P1P2}(\lambda)d\lambda \qquad (2.3)$$

Here $A_{total}(\lambda)$ is the wavelength-dependent extinction of light by Cit-Au NPs in the presence of proteins, $A_{NP}(\lambda)$ is the wavelength-dependent extinction of light by Cit-Au NPs which remain free and do not form agglomerate, $A_{P1}(\lambda)$ is the wavelength-dependent extinction of light by $P1$ agglomerated Au NPs, $A_{P2}(\lambda)$ is the wavelength-dependent extinction of light by $P2$ agglomerated Au NPs and $A_{P1P2}(\lambda)$ is the wavelength-dependent extinction of light by Au NPs agglomerated with both $P1$ and $P2$. Further, the integrated extinction of light could be rewritten as,

$$\int A_{total}(\lambda)d\lambda = \frac{l}{2.303}\left[\int N_{NP}Q_{extNP}(\lambda)d\lambda + \int N_{P1}Q_{extP1}(\lambda)d\lambda + \int N_{P2}Q_{extP2}(\lambda)d\lambda + \int N_{P1P2}Q_{extP1P2}(\lambda)d\lambda\right] \quad (2.4)$$

Here, $N_{total} = N_{NP} + N_{P1} + N_{P2} + N_{P1P2}$, where N_{total} is the total number of Au NPs present in the medium, N_{NP} is the number of Cit-Au NPs which are free, N_{P1} is the number of Au NPs agglomerated with $P1$, N_{P2} is the number of Au NPs agglomerated with $P2$ and N_{P1P2} is the number of Au NPs agglomerated with both $P1$ and $P2$, all measured at the same instant of time. It has been observed earlier[67] and also reported herein that interaction of a single protein with Cit-Au NPs led to the formation of agglomerated structures for which the change in the area of extinction was linear with the concentration of protein. Thus it can be approximated that the number of particles associated with the composite formation linearly depended on the concentration of protein. In other words, $N_P = kC_P$, where C_P is the concentration of the protein involved and k is the proportionality constant. So far as the composite with two proteins is concerned one can write the number of NP involved as $N_{P1P2} = f(P1, P2)$. For the integrated extinction of light to be linear with either of the protein concentrations (while the second is kept constant), the following condition needs to be satisfied: $N_{P1P2} = k_3C_{P1} + k_4C_{P2}$ and the integrated extinction of light could be written as,

$$\int A_{total}(\lambda)d\lambda = \frac{l}{2.303}\left[N_{total}\int Q_{extNP}(\lambda)d\lambda + \left\{k_2\left(\int Q_{extP2}(\lambda)d\lambda - \int Q_{extNP}(\lambda)d\lambda\right) + k_4\left(\int Q_{extP1P2}(\lambda)d\lambda - \int Q_{extNP}(\lambda)d\lambda\right)\right\}C_{P2}\right.$$

$$\left. + \left\{k_1\left(\int Q_{extP1}(\lambda)d\lambda - \int Q_{extNP}(\lambda)d\lambda\right) + k_3\left(\int Q_{extP1P2}(\lambda)d\lambda - \int Q_{extNP}(\lambda)d\lambda\right)\right\}C_{P1}\right] \quad (2.5)$$

In different sets of preparations of Cit-Au NPs there are variations in the size and distribution of Au NPs and this will be reflected in the extinction spectra. Thus the total area under the curve would vary from sample to sample. If the variation is sufficiently small then the associated changes could be accommodated by dividing both sides of equation 5 by $\int A_{NP}(\lambda)d\lambda$. The resultant equation could be written as,

$$\frac{\int A_{total}(\lambda)d\lambda}{\int A_{NP}(\lambda)d\lambda} = 1 + \frac{l}{2.303\int A_{NP}(\lambda)d\lambda}\left[\left\{k_2\left(\int Q_{extP2}(\lambda)d\lambda - \int Q_{extNP}(\lambda)d\lambda\right) + k_4\left(\int Q_{extP1P2}(\lambda)d\lambda - \int Q_{extNP}(\lambda)d\lambda\right)\right\}C_{P2}\right.$$

$$\left. + \left\{k_1\left(\int Q_{extP1}(\lambda)d\lambda - \int Q_{extNP}(\lambda)d\lambda\right) + k_3\left(\int Q_{extP1P2}(\lambda)d\lambda - \int Q_{extNP}(\lambda)d\lambda\right)\right\}C_{P1}\right] \qquad (2.6)$$

Therefore, the ratio of area under the extinction curve would vary linearly with either of the protein concentration provided the concentration of second protein is kept constant. The linear increase in the area under the curve with respect to concentrations of one of the proteins while keeping the other constant may at first indicate that interactions between the proteins and Cit-Au NPs could possibly be independent events. In other words, each protein could interact independently with the NPs and there is no secondary interaction between the two proteins involved. However, it could also be possible that the interactions between these two proteins and Cit-Au NPs were identical even when present as a mixture. In other words, if agglomeration took place with increasing concentration of one protein the behavior would be similar for the other protein. Thus the extent of agglomeration in the presence of increasing concentration of either of the proteins, while that of the other being kept constant, was similar. Essentially, a mixture of proteins would behave like that of a single protein, with the protein whose concentration is being increased leading the nature of the agglomerate. This would mean increasing concentration of α-amylase (with keeping BSA constant) would have a different slope than that of increasing concentration of BSA (keeping α-amylase constant). That the slopes were different (**Figures 2.8, 2.9 and 2.10**) support the above. Also, the concentration ranges where the linearity was maintained were similar to the results when individual proteins were used instead of a mixture.[67] On the other hand, when the area is not linearly dependent on any of the protein concentration then the expression could be

written as,

$$\frac{\int A_{total}(\lambda)d\lambda}{\int A_{NP}(\lambda)d\lambda} = 1 + \frac{l}{2.303\int A_{NP}(\lambda)d\lambda}\Big[k_2\Big(\int Q_{extP2}(\lambda)d\lambda - \int Q_{extNP}(\lambda)d\lambda\Big)C_{P2} + k_1\Big(\int Q_{extP1}(\lambda)d\lambda - \int Q_{extNP}(\lambda)d\lambda\Big)C_{P1}$$

$$+\Big(\int Q_{extP1P2}(\lambda)d\lambda - \int Q_{extNP}(\lambda)d\lambda\Big) f(P1,P2)\Big] \qquad (2.7)$$

Thus, when one of the protein concentrations is sufficiently low and hence the last term involving the concentrations of both the proteins is small, the dependence is again linear with either of the protein concentration. It is important to mention here that the extinction coefficients of agglomerated structures have been assumed to be invariant with an increase in the extent of agglomeration upon serial addition of proteins. In other words, with increase in protein concentrations, although the number of agglomerated structures and extent of agglomeration increased, the environment surrounding each NP might not have changed further in the higher agglomerated structures. Thus any change in extinction coefficient (i.e. complex dielectric function of the surface coating and the volume fraction occupied by the surface coating) might be assumed to be minimal.

The **Scheme 2.1 a** shows that in case of single protein the agglomeration increases systematically and thus the area under the curve increases linearly with concentration of the protein. In case of binary mixtures if the Au NPs agglomerated systematically with both P1 and P2 (as depicted in **Scheme 2.1 b** Case 1), the area under the curve would vary linearly. However, if the interaction of Au NPs with both P1 and P2 changes agglomeration abruptly (as depicted in **Scheme 2.1 b**, Case 2), the area under the curve would vary non-linearly.

A binary mixture of proteins may interact with the Cit-Au NPs present in the medium leading to partial or complete replacement of the stabilizers (citrate). It is likely that both the proteins would be attached simultaneously; however, their population ratio in each particle may be decided by the properties of individual protein especially its affinity toward the NP. Thus the equilibrium population of the proteins attached to a particle would not only be decided by their concentrations in the medium but also their three-dimensional structures with

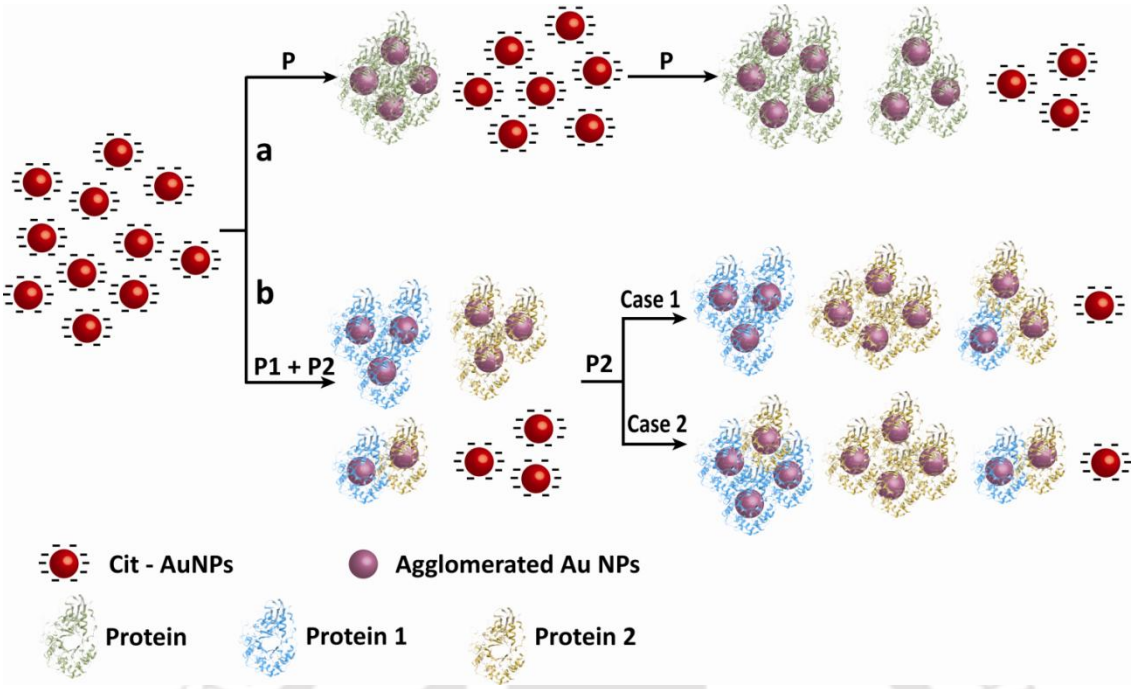

Scheme 2.1 A schematic representation of the process of agglomeration of the NPs in the presence of (a) single protein and (b) binary mixtures of proteins.

constituent amino acids especially those exposed to the medium.[99] This specificity has been observed in the interaction between a protein and Cit-Au NP, as reflected in the difference in changes of optical property of Cit-Au NPs in the presence of different mixtures of proteins. However, the interaction between a binary protein mixture and Cit-Au NP would not only depend on the specificity but also on the relative affinity. For example, one may ask the question whether change in the area under the extinction curve would depend on the method of protein addition to the NPs. In other words, what would be possible differences if proteins were added as a mixture versus in sequence? In this regard, when the binary mixture of α-amylase and BSA was added to 3.0 mL of Cit-Au NPs, with the final concentrations being 0.071 μg mL^{-1} and 0.633 μg mL^{-1} respectively, broadening of the SPR peak of Cit-Au NPs was observed and the ratio of area under the UV-visible spectrum of Cit-Au NP-protein solution to that of Cit-Au NPs only was found to be 1.028 + 0.010. Peak broadening was also observed upon addition of 0.633 μg mL^{-1} BSA to 3.0 mL of Cit-Au NPs already containing 0.071 μg mL^{-1} of α-amylase, and the ratio of area under the spectra was observed to be 1.025 + 0.003. On the other hand, addition of 0.071 μg mL^{-1} of α-amylase to 3.0

mL of Cit-Au NPs already containing 0.633 μg mL^{-1} of BSA not only broadened the spectrum but also lead to a comparatively significant increase in the ratio of the area under the spectra (to a value of 1.043 + 0.008). The above results are from experiments performed in triplicates and the concentrations of the proteins refer to concentrations of the final solution. It could be noted that the ratio of area under the spectra for the first and second mode of addition of proteins to Cit-Au NPs were similar suggesting that the mechanism of interaction of proteins with Cit-Au NPs in these two cases were similar. However, the different value of the ratio of area under the spectra for the third mode of addition indicated the involvement of different kind of mechanism of interaction between the proteins and Cit-Au NPs. Similar results were obtained for a dispersion of Cit-Au NPs containing 0.118 μg mL^{-1} α-amylase and 1.899 μg mL^{-1} BSA. The ratios of area corresponding to different sequences of addition of proteins to the NP dispersion to reach the final mixture are shown in **Tables 2A.2 and 2A.3**, *Appendix*. The UV-visible graphs are shown in **Figure 2A.9**, *Appendix*.

The above experiments were also carried out for a mixture of 0.157 μg mL^{-1} AMG and 0.118 μg mL^{-1} α-amylase as well as for a mixture of 0.045 μg mL^{-1} GOD and 0.043 μg mL^{-1} POD. In case of α-amylase and AMG (**Tables 2A.4**, *Appendix*), when mixture of 0.157 μg mL^{-1} AMG and 0.118 μg mL^{-1} α-amylase was added to 3.0 mL of Cit-Au NPs, the ratio of area under the curves was found to be 1.032 ± 0.004. On addition of 0.157 μg mL^{-1} AMG to 3.0 mL of Cit-Au NPs already containing 0.118 μg mL^{-1} α-amylase, the ratio of area was found to be 1.037 ± 0.006. On the other hand when 0.118 μg mL^{-1} α-amylase was added to 3.0 mL of Cit-Au NPs already containing 0.157 μg mL^{-1} AMG, the ratio of area was observed to be 1.087 ± 0.014. For GOD and POD (**Tables 2A.5**, *Appendix*), when 0.045 μg mL^{-1} GOD and 0.043 μg mL^{-1} POD was added as a mixture to Cit-Au NPs, the ratio of area was noted to be 1.001 ± 0.004. Additionally, when 0.045 μg mL^{-1} GOD was added to 3.0 mL of Cit-Au NPs already containing 0.043 μg mL^{-1} POD, the ratio of area was almost same (1.001 ± 0.001). However, when 0.043 μg mL^{-1} POD was added to 3.0 mL of Cit-Au NPs already containing 0.045 μg mL^{-1} GOD, the ratio of area changed to 1.017 ± 0.004.

The dependence of ratio of area on the sequence of addition indicated different affinities of proteins for their attachment to the NPs as well as their tendencies for forming agglomerates. For example, between α-amylase and BSA, α-amylase may not only have higher affinity for the NPs but also have higher tendency for agglomeration. Thus when present as a mixture or α-amylase being added initially the preferential attachment of the protein in combination with lower tendency of BSA (for agglomeration) leads to the same final structure. Thus the changes upon addition of BSA following α-amylase would be too feeble to lead to further agglomeration. On the other hand, when BSA is added initially there is a lower level of agglomeration occurring upon attachment of the protein to the NPs. However, following subsequent addition of α-amylase while some of the BSA molecules attached to the NPs may be replaced, further agglomeration would occur without disrupting the initial agglomerates. In other words, in the presence of BSA alone (at its low concentration) the level of agglomeration would be low and there may be considerable presence of NPs without agglomeration even if they contained the protein. Upon subsequent addition, α-amylase would not only replace the BSA (at least partially) present in non-agglomerated structures but would also enhance aggregation thus increasing the overall agglomeration. This would lead to increased broadening of the spectrum as observed. An important factor that would decide the attachment of the protein to Cit-Au NP as well as higher tendency for agglomeration could be the overall charge of the protein present in the medium. The net charge of a protein present in a medium is dependent on the isoelectric point (pI) of the protein. For example, pI values of α-amylase, BSA, AMG, GOD and POD are 6.5, 4.7, 4.35, 4.2, and 7.2 respectively.[100-103] This means BSA, AMG and GOD would be present in the solution (at pH 7.0) with overall negative charge. On the other hand, α-amylase and POD are expected to be present close to their zwitter ionic form in the solution. When the proteins are present close to their zwitter ionic form it might be that they would interact with negatively charged Cit-Au NPs either with exposed thiol group or positively charged functional groups present in the protein. On the other hand, the proteins with overall negative charge might tend to be repelled from the negatively charged Cit-Au NPs. However, if any of those proteins contain exposed thiol group, in addition, the interaction could be due to the thiol moiety, as thiol groups are

known to have higher affinity for Au NPs in comparison to other functional groups in proteins.[104] Further, it could be possible that with time the negatively charged protein molecules might replace the negatively charged citrate ions from the NP. The electrostatic stabilization of NPs by citrate could involve dynamic exchanges of citrate ions present in the solution in absence of proteins. Thus likewise proteins with overall negative charge could also be exchanged. Once attached to the NPs the proteins might partially unfold and lead to agglomeration with additional proteins and NPs present in the medium. In case of binary mixture, thus overall interaction would involve preferential attachment of one protein over the other with subsequent agglomeration in the presence of both. This would depend on the overall charge and amino acid residues of both the proteins. It may also be dependent on the partially unfolded structure of the protein attached to the NP. Thus, in case of α-amylase-BSA mixture, α-amylase being close to their zwitter ionic form and having two exposed thiol groups[105] would bind preferentially to Cit-Au NPs over BSA, with the latter being present as a negatively charged moiety. As a result when α-amylase and BSA were added as a mixture to Cit-Au NPs, the ratio of area was similar to that when α-amylase was added followed by BSA to Cit-Au NPs. Similar was the case for α-amylase and AMG mixture. Moreover, in case of GOD-POD mixture, POD (having no thiol group[105]; pI 7.2) interacted with Cit-Au NPs preferentially over GOD (although having exposed thiol groups[106]; pI 4.2). This might be due to the presence of its zwitter ionic form which leads to the preferential attachment of the protein over GOD to the NPs. This indicated that overall charge of the protein in the solution may play a pivotal role in interaction with Cit-Au NPs. However, the role of exposed thiol groups cannot be ruled out completely.

Since among the combinations of binary mixture of proteins mentioned above the linearity of increase of area under the extinction curve of Cit-Au NPs versus the protein concentration was clearly observed for α-amylase and BSA, the interactions between the two proteins and Cit-Au NPs were investigated in more detail. This was further pursued by SDS-PAGE, enzymatic activity assay of α-amylase, photoluminescence, and FTIR studies. SDS-PAGE analysis (**Figure 2.13 a**) revealed the presence of a major band around 66 kDa, corresponding to BSA

(Lane 2). In case of pure α-amylase, a band around 50 kDa was evident corresponding to the expected size of porcine pancreatic α-amylase (Lane 3). It could also be seen that other minor bands were visible in both Lanes 2 and 3 and presumably were due to degradation products of pure proteins in the presence of the denaturing gel. In case of composite of Cit-Au NPs (Lane 4), an upper band was observed whose mobility coincided with that of pure BSA (indicated by line 'a' in Lane 4). Likewise, a band of lesser intensity was observed corresponding to the size of α-amylase (indicated by line 'b' in Lane 4). This confirmed the presence of both α-amylase and BSA in the NP-protein composite. The fact that the bands migrated separately in the gel indicates that the proteins dissociated from the composite and migrated as individual proteins in denaturing gel conditions. The bands were less intense due to a smaller amount of proteins present in the NP-protein composite. The other minor bands in the composite (Lane 4) were likely the degradation products of the original proteins as observed in Lanes 2 and 3. No band was observed in Lane 5, which corresponded to Cit-Au NPs only.

For enzymatic activity of α-amylase, starch agar plate assay was performed (**Figure 2.13 b**). Around wells i and iii (corresponding to pure α-amylase and composite respectively), clear zones were observed which indicated the presence of α-amylase with observable retention of activity. As seen from the figure, the zone of clearance for the composite was smaller than for pure α-amylase. This could be because of limited diffusion of Au NP-protein composite in the solid medium compared to that of the free enzyme. Moreover, the amount of enzyme associated with the composite was less compared to that of the added free enzyme. On the other hand, no such clearing zone was observed around wells ii, iv, and v (corresponding to phosphate buffer, BSA, and Cit-Au NPs respectively). Further experiments were performed with three different concentrations of the protein mixtures (1.266 μg mL^{-1} BSA and 0.094 μg mL^{-1} α-amylase, 1.266 μg mL^{-1} BSA and 0.165 μg mL^{-1} α-amylase and 1.266 μg mL^{-1} BSA and 0.235 μg mL^{-1} α-amylase). All of them exhibited enzyme activity. Thus not only the α-amylase was present in the mixture its activity was also considerably retained (**Figure 2A.10**, *Appendix*).

It is known that when protein is mixed with Cit-Au NPs the fluorescence due to tryptophan residue occurring at 360 nm gets quenched, indicating the attachment of the protein to the NP.[107] In the present set of experiments the emission peak at 360 nm, for α-amylase, BSA, and the mixture of the two, disappeared in the presence of Cit-Au NPs. The fluorescence spectroscopic results are shown in **Figure 2.13 c**. The loss of fluorescence of the mixture of proteins in the presence of Cit-Au NPs indicated that both of them possibly were attached to the NPs at the total protein concentration. Interestingly, when BSA (1.582 μg mL^{-1}) was added to α-amylase (0.118 μg mL^{-1}) treated Cit-Au NPs, its fluorescence was also quenched. This indicates that even in the presence of α-amylase, at its sufficiently low concentration, BSA interacted with Cit-Au NPs. Similar observation was made

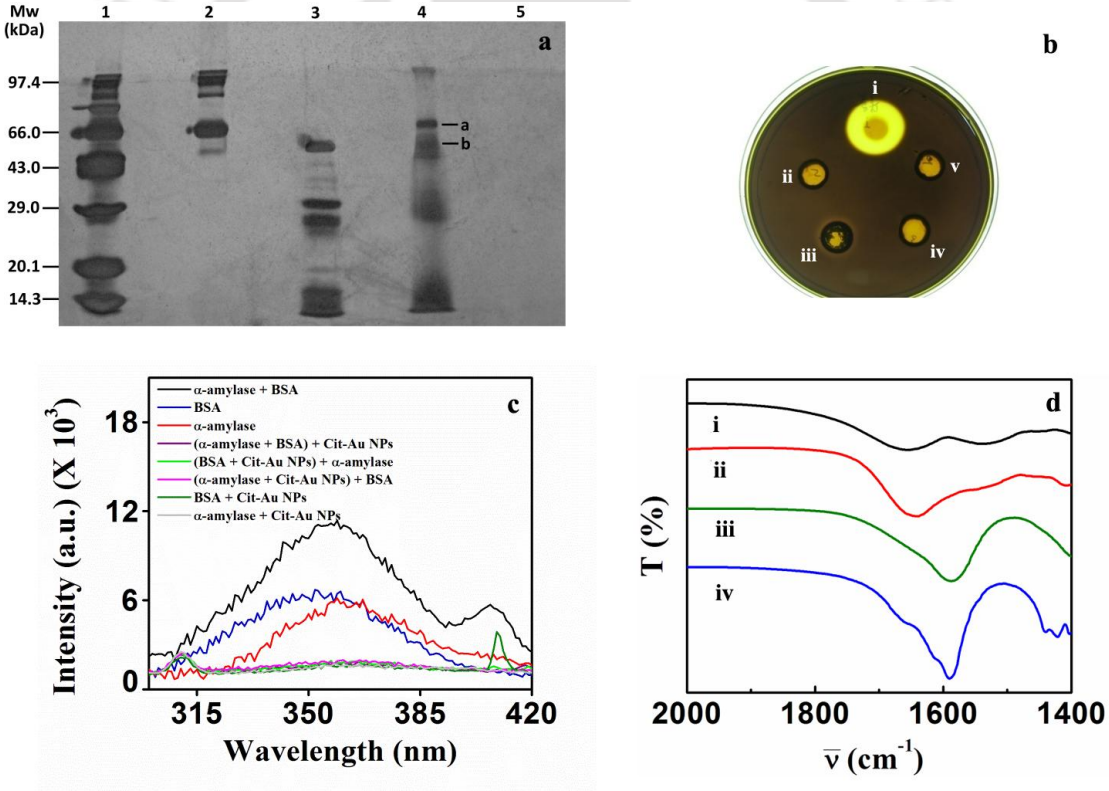

Figure 2.13 (a) SDS-PAGE analysis of Au NP-protein composite. Wells correspond to (1) Protein Marker, (2) BSA, (3) α-amylase, (4) α-amylase-BSA-Au NP composite and (5) Cit-Au NPs only. (b) Starch agar plate assay for enzymatic activity of (i) pure α-amylase, (ii) phosphate buffer, (iii) α-amylase-BSA-Au NP composite, (iv) BSA and (v) Cit-Au NPs only. (c) Fluorescence spectra of α-amylase and BSA in the presence and absence of Cit-Au NPs and (d) FTIR spectra of (i) BSA, (ii) α-amylase, (iii) Cit-Au NPs only and (iv) Cit-Au NPs in presence of a mixture of 0.118 μg mL^{-1} α-amylase and 1.899 μg mL^{-1} BSA.

when α-amylase (0.118 μg mL^{-1}) was added to Cit-Au NPs containing BSA (1.582 μg mL^{-1}). The time-dependent study of Cit-Au NPs in the presence of 0.118 μg mL^{-1} α-amylase and 1.582 μg mL^{-1} BSA (**Figure 2A.11**, *Appendix*) indicated that within 1 min of mixing the proteins with the NPs the fluorescence was quenched. This indicated that the proteins were attached to the NPs immediately upon addition.

FTIR spectroscopy is also an important tool to study the interaction between a biomolecule and NP.[105] For example, it has been used to study the conformational changes in the secondary structure of proteins upon interacting with Au NPs.[108] There are three types of amide linkages in proteins – amide I, amide II, and amide III – of which amide I absorbs between 1600-1700 cm^{-1}.[109] For BSA as well as α-amylase (**Figure 2.13 d i and ii**), the FTIR band observed in the region 1625-1700 cm^{-1} is due to amide I linkage whereas for Cit-Au NPs (**Figure 2.13 d iii**), the band around 1589 cm^{-1} is due to the presence of acidic C=O group of citrate (**Figure 2A.12 i**, *Appendix*) on its surface. In the NP-protein composite containing 0.118 μg mL^{-1} α-amylase and 1.899 μg mL^{-1} BSA (**Figure 2.13 d iv**), a broad band in the region 1500-1750 cm^{-1} was observed and it appears to be a combination of three bands. The band around 1589 cm^{-1} matched with that of Cit-Au NPs and the appearance of a shoulder at around 1663 cm^{-1} indicated the presence of proteins on the surface of Au NPs, in addition to citrate. This also supports the partial replacement of trisodium citrate by proteins.[67] Further, the occurrence of an additional peak at 1615 cm^{-1} indicated interaction between the protein and Au NP. The proteins on interacting with Au NP possibly adopt a more incompact conformational state as such changes at both the secondary and tertiary structure levels are known to occur.[108] The appearance of this band can also be due to H-bonding of the amide C=O with water molecules.[110] As the protein structure becomes more flexible on interacting with Cit-Au NPs, the amide linkages become more prone to H-bonding with water molecules, possibly as a result the band downshifts. The above experiment along with SDS-PAGE, enzymatic activity assay of α-amylase, and fluorescence results indicated that both α-amylase and BSA interacted with Cit-Au NPs. Thus when binary mixtures of α-amylase and BSA were added to Cit-Au NPs not only both proteins were attached to the NPs but they were also part of the composite of the proteins and NPs, which led to systematic spectral broadening.

2.3 Conclusions

In summary, we have been able to demonstrate that there is specificity in the interaction of a binary mixture of proteins with Cit-Au NPs and the interactions could be different from those with individual proteins or simple summation of interactions of the component proteins. While a mixture of α-amylase and BSA consistently changed the level of agglomeration with an increase of one in the presence of other; the mixture of α-amylase and AMG behaved completely differently. However for GOD-POD mixture, the consistent increase in agglomeration of NPs depended on the concentration of GOD in the solution. High concentrations of GOD led to lowering of agglomeration of Cit-Au NP-protein mixture, while that at low concentrations gave rise to systematic agglomeration. Thus it is not necessary that the presence of proteins will lead to significant agglomeration of Cit-Au NP; however, that would be dependent on the nature of proteins and their concentrations. In case of individual proteins, the area under the SPR spectrum of Cit-Au NPs changed consistently with increase in concentration of the protein.[67] In case of α-amylase-BSA and GOD-POD (at low concentrations of GOD) mixture the trend was maintained but not in case of α-amylase-AMG mixture as well as in case of high concentrations of GOD in the GOD-POD mixture. Interestingly, the results also suggested that a particular protein may preferentially bind with Cit-Au NPs over another one, depending on the overall charges of the proteins in a solution. These behaviors were also reflected in the optical properties of the Cit-Au NPs in the presence of the mixtures of the proteins.

Finally, the present investigations indicated the possibility of a rich and diverse nature of interactions between Cit-Au NPs and a mixture of proteins. Thus, when Au NPs would be present inside a living cell, their interactions with the biomolecules in the milieu would possibly be more than the sum of their interactions with individual molecules of the cell. Further, the study also points out that in order to understand and address the issue of the persistent presence of nanomaterials in living beings and in the environment, it is imperative that efforts may be made to probe the complexity of the interactions rather than assuming them to be a simple summation of individual interactions.

CHAPTER 3

Gold Nanoparticle-Protein Agglomerates as Versatile Nanocarriers for Drug Delivery

As Chapter 2 described the formation of NP-protein agglomerates, this chapter demonstrates the use of agglomerates as a versatile nanocarrier for cancer drug delivery. The carriers exhibited efficient loading capacities for both hydrophilic (doxorubicin) and hydrophobic (pyrene) molecules. The nanocarriers were finally coated with an albumin layer to render them stable and also facilitated their uptake by cancer cells. The interaction between agglomerated structures and the payloads was non-covalent. Cell viability assay in vitro showed that the nanocarriers by themselves were non-cytotoxic, whereas the doxorubicin loaded ones were cytotoxic, with efficiencies higher than that of the free drug. Transmission electron microscopy (TEM) and fluorescence microscopy along with flow cytometry analysis confirmed the uptake of the drug loaded nanocarriers by a human cervical cancer HeLa cell line. Field emission scanning electron microscopy (FESEM) revealed the formation of apoptotic bodies leading to cell death, confirming the release of the payloads from the nanocarriers into the cell. Overall, the findings suggested the fabrication of novel Au NP-protein agglomerate-based nanocarriers having efficient drug loading and releasing capabilities, enabling them to act as multimodal drug delivery vehicles.

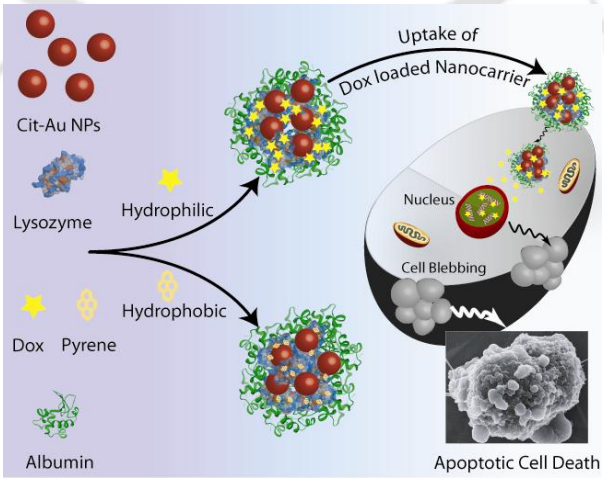

[Rumi et al. *Small* 2013, *9*, 3494–3505] - Reproduced by permission of Wiley http://onlinelibrary.wiley.com/doi/10.1002/smll.201203095/abstract

3.1 Experimental Section

3.1.1 Materials

Hydrogen tetrachloroaurate trihydrate ($HAuCl_4.3H_2O$), pyrene (Pyr) and 2,3-Bis(2-methoxy-4-nitro-5-sulfophenyl)-2H-tetrazolium-5-carboxanilide (XTT) were purchased from Sigma-Aidrich Co., USA. The hen egg white lysozyme (Lyz) was purchased from Sisco Research Laboratories Pvt. Ltd. (SRL), India. Doxorubicin hydrochloride (Dox) was manufactured by Parental Drugs (India) Ltd and was purchased from commercial source. Bovine serum albumin (BSA), trisodium citrate dihydrate and all other reagents required for experiments were obtained from Merck Specialities Pvt. Ltd., India. Milli-Q grade water (>18 MΩ cm, Millipore) was used in all experiments.

3.1.2 Synthesis of citrate-stabilized Au NPs (Cit-Au NPs)

The dispersion of Au NPs was prepared using the well-known citrate reduction of $HAuCl_4$, which was slightly modified.[111] Briefly, Milli Q grade water (100 mL) containing trisodium citrate dihydrate (0.0034 M) was refluxed under stirring condition. When the solution started boiling, $HAuCl_4$ (1 mL of 1.73 x 10^{-2} M) was added all at once. The color of the solution immediately changed to blue and then to bright red, indicating the formation of dispersion of Cit-Au NPs. The reaction was continued for another 30 min for complete reduction of the salt. The synthesis of Cit-Au NPs was confirmed by recording the extinction spectrum and analyzing the sample under a TEM.

3.1.3 Generation and characterization of Dox/Pyr loaded Au NP-Lyz nanocarriers

The nanocarriers were generated based on agglomeration of Au NPs and Lyz. The Cit-Au NP dispersion (15 mL) was incubated with Lyz solution (2.5 mL of 0.01 mg mL^{-1}) for 30 min. After this, Dox solution (1 mL of 16.4 μg mL^{-1}, which is the actual content of Dox in the as-prepared solution) or aqueous Pyr solution (600 μL of 2 μg mL^{-1}), prepared from 0.2 mg mL^{-1} Pyr solution in ethanol, was added to the above solution and was incubated for another 30 min in the dark. Then, BSA solution (2.1 mL of 1 %, w/v) along with sodium phosphate buffer (0.01 M, pH

7.4) was added such that the final concentrations of Lyz, Dox, Pyr and BSA were 1.19 μg mL^{-1}, 0.78 μg mL^{-1}, 0.057 μg mL^{-1} and 1 mg mL^{-1} respectively. The above solution was centrifuged at 20000 relative centrifugal force (rcf) and 4 °C for 15 min. The supernatant was discarded and the pellet was washed using BSA solution (0.1 %, w/v). Finally, the pellet obtained was re-suspended in BSA solution (3 mL of 0.1 %, w/v) by sonication in a water bath for 1 min.

UV-visible measurements were performed using a Hitachi U-2900 double beam spectrophotometer. Particle size analysis was carried out by a dynamic light scattering (DLS)-based technique using a Zetasizer Nano ZS90 instrument fitted with a 633 nm red laser (Model No. ZEN3690, Malvern). The emission spectra were recorded using a Fluoromax 4 spectrofluorometer having a xenon lamp. Excitation wavelength was set at 480 nm for samples containing Dox and at 334 nm for samples containing Pyr. The excitation and emission slit widths were fixed at 5 nm. TEM samples were prepared by drop-casting the sample on carbon-coated copper TEM grids, which were left overnight for drying. Those samples were then analyzed under a JEOL JEM 2100 transmission electron microscope, operating at a maximum accelerating voltage of 200 kV.

3.1.4 Stability test of Dox or Pyr loaded Au NP-Lyz nanocarriers and sodium dodecyl sulphate polyacrylamide gel electrophoresis (SDS-PAGE) analysis

The stability of Dox or Pyr loaded nanocarriers was checked by following UV-visible spectra of Au NPs. The Dox or Pyr loaded nanocarriers were prepared as described earlier and were diluted with BSA solution (0.1 %, w/v) such that the maximum extinction was ~1.0. The sample was then stored at 4 °C. Then the extinction spectra of the respective nanocarriers were recorded at predetermined time points (after the samples were brought to room temperature) for up to 48 h. For SDS-PAGE analysis, the pellet of Dox loaded nanocarriers (after washing for several times following centrifugation) was dissolved in sodium phosphate buffer (15 μL) by sonication. The samples were mixed with protein loading buffer and boiled for 5 min in water bath. Next, the samples were loaded in polyacrylamide gel (12 %) and electrophoresis was carried out at 120 V for about 2 h. The gel was stained in coomassie blue staining solution (45 % methanol, 10 % glacial acetic acid and 0.25 % (w/v) coomassie brilliant blue R-250) for 1 h and then destained

in methanol (15 %) and glacial acetic acid solution (10 %) overnight. The SDS-PAGE experiment was repeated for which the gel was silver-stained instead. The gels were observed under Gel Logic 212 PRO Imaging System (Carestream).

3.1.5 Loading efficiency of the Au NP-Lyz nanocarriers for Dox or Pyr and their in vitro release

To quantitatively determine the amount of Dox or Pyr loaded in the nanocarriers, the Cit-Au NP dispersion (15 mL) was incubated with Lyz solution (2.5 mL of 0.01 mg mL^{-1}) for 30 min. To this, Dox solution (1 mL of 16.4 μg mL^{-1}) or aqueous Pyr solution (600 μL of 2 μg mL^{-1}) was added and incubated for another 30 min in the dark. Then BSA solution (2.1 mL of 1 %, w/v) along with sodium phosphate buffer was added and the dispersion was centrifuged at 20000 rcf and 4 °C for 15 min. The supernatant was collected and its emission spectrum was recorded using a spectrofluorometer at an excitation wavelength of 480 nm (for Dox loaded nanocarriers) or 334 nm (for Pyr loaded nanocarriers). The emission intensity at 595 nm (for Dox loaded nanocarriers) or 396 nm (for Pyr loaded nanocarriers) was noted and using the respective standard curves, the amount of free Dox or Pyr in the supernatant was calculated. All the measurements were performed in triplicates.

The loading efficiency (L.E) was then calculated as:

$$L.E.\ \% = \frac{Dox_i - Dox_s}{Dox_i} X100 \qquad (3.1)$$

where, $[Dox]_i$ is the concentration of Dox initially added and $[Dox]_s$ is the concentration of Dox in the supernatant. The L.E. for Pyr was also calculated in the same way.

Standard curves of Dox or Pyr for loading efficiency studies

Fluorescence intensity of Dox is a function of pH; it is reported that fluorescence intensity decreases with increase in pH.[112] Therefore, for determining the concentrations of free Dox or Pyr, the standard curves were made by dissolving different amount of Dox or Pyr in the supernatant, obtained after centrifugation of nanocarriers only (Dox free). The emission spectra of the samples were recorded

and the intensities at 595 nm (for Dox samples) or 396 nm (for Pyr samples) were used for the preparation of standard curves.

The in-vitro release of Dox or Pyr from the nanocarriers was studied in acetate (0.02 M, pH 4.0) and phosphate (0.02 M, pH 7.4) buffers for 24 h. For this, Dox or Pyr loaded nanocarriers (0.3 mL) were mixed with acetate or phosphate buffer (1.2 mL) in different 2 mL vials and were incubated in a shaking water bath at 37 °C. At different time intervals (up to 24 h), the samples were collected and centrifuged at 20000 rcf and 4 °C for 15 min. The supernatant was used for spectral analysis. The emission intensity of supernatant at 595 nm (for Dox loaded nanocarriers) or 396 nm (for Pyr loaded nanocarriers) was recorded. The amount of Dox or Pyr released in the supernatant was calculated using the standard curves of Dox or Pyr (the procedure of which is mentioned below) and the cumulative release (C.R.) was calculated by the following formula:

$$C.R.\ \% = \frac{Dox_{s}}{Dox_{l}} X100 \qquad (3.2)$$

where, $[Dox]_s$ is the concentration of Dox released in the supernatant and $[Dox]_l$ is the concentration of Dox loaded in the nanocarriers. The C.R. for Pyr was also calculated using the same formula.

Standard curves of Dox or Pyr for in vitro release studies

For determining the concentrations of Dox or Pyr released, standard curves of Dox or Pyr were generated by preparing Dox free nanocarriers (3 mL) and mixing with acetate or phosphate buffer (12 mL), as applicable. The dispersion was centrifuged and the supernatant was used for preparing the Dox or Pyr solutions of different concentrations. The emission spectra of the samples were recorded and the intensities at 595 nm (for Dox samples) or 396 nm (for Pyr samples) were used for drawing the standard curves. It may be mentioned here that all of the above experiments were performed in triplicates.

3.1.6 TEM and FESEM analysis of the untreated and treated cells

Human cervical cancer HeLa cell lines were maintained in the Dulbecco's Modified Eagle Medium supplemented with fetal bovine serum (10 %, v/v), penicillin (50

units mL^{-1}) and streptomycin (50 mg mL^{-1}) in a humidified atmosphere containing 5 % CO_2 at 37 °C. For TEM and FESEM analysis, HeLa cells were seeded in a 35 mm cell culture plate and grown for 24 h. After that the medium was removed, the cells were washed with phosphate buffered saline (PBS; 0.01 M, pH 7.4) and the serum free medium containing Dox loaded nanocarriers was added to the cells. For control sample, serum free medium without nanocarriers was added to the cells. The cells were incubated for 4 h and then washed with PBS several times. Next, the cells were trypsinized, centrifuged and fixed in glutaraldehyde solution (2 %) for 4 h. The cells were dehydrated in graded ethanol solutions and finally suspended in absolute ethanol. For TEM sample preparation, the cell suspension (10 μL) was drop-cast on carbon-coated copper TEM grid and left for air drying. The grid was then analyzed under transmission electron microscope. For FESEM analysis, the cell suspension (15 μL) was deposited on a glass slide (wrapped with an aluminium foil), dried and then coated with a gold film (using SC7620 "Mini", Polaron Sputter Coater, Quorum Technologies, Newhaven, England). The sample was analyzed under ΣIGMA, Carl Zeiss field emission scanning electron microscope. It is to be mentioned here that the serum free medium was used throughout the cell experiments in order to avoid the interaction of serum proteins with nanocarriers, which can influence the cellular uptake as well as toxicity.[113] However, BSA (0.1 %, w/v) was added to the serum free medium (before the addition of nanocarriers) to avoid further agglomeration in the cell medium.[114]

3.1.7 Flow cytometry analysis

HeLa cells were seeded in a 6 well plate (2×10^5 cells $well^{-1}$) and grown for 24 h. The serum medium was then removed and the serum free medium containing Dox loaded nanocarriers (0.15 mg mL^{-1}) was added to the cells. After 4 h of incubation, the medium was removed and the cells were washed with PBS for several times. The cells were trypsinized, centrifuged and the cell pellet was re-suspended in 1 mL of PBS. The same treatment was also done to HeLa cells incubated with nanocarriers (0.15 mg mL^{-1}) and Dox (0.64 μg mL^{-1}) respectively. The cells were finally analyzed using a FACS Calibur flow cytometer. For each of the samples, the analysis was done in triplicates. The uptake of the Dox loaded nanocarriers and

Dox only by the HeLa cells with time was also monitored for 6 h using the same technique.

3.1.8 Fluorescence microscopy

HeLa cells were seeded in a 6 well plate (2×10^5 cells $well^{-1}$) and grown for 24 h. The serum medium was then removed and the serum free medium containing Dox loaded nanocarriers (0.15 mg mL^{-1}), nanocarriers (0.15 mg mL^{-1}) and Dox (0.64 μg mL^{-1}) were added separately to the different sets of cells. After 4 h of incubation, the medium was removed and the cells were washed with PBS for several times. Then the cells were observed under fluorescence microscope (Nikon eclipse Ti) and the images were recorded using a Qdot 655 filter.

3.1.9 Cell viability assay

For cell viability assay, cells (10^4 cells $well^{-1}$) were seeded in a 96 well microplate and grown overnight. Then the serum medium was removed and serum free medium containing varying concentrations of Dox loaded nanocarriers (0.05 mg mL^{-1} – 0.2 mg mL^{-1}) was added to the cells. After 24 h of incubation, the cells were washed with PBS and finally XTT based cell viability assay was carried out according to the manufacturer's protocol. As a control the same experiment was carried out with varying concentrations of Dox (0.22 μg mL^{-1} – 0.84 μg mL^{-1}) and with varying concentrations (0.05 mg mL^{-1} – 0.2 mg mL^{-1}) of nanocarriers. For each of the samples, the assay was carried out in triplicates.

3.2 Results and Discussion

3.2.1 Generation and characterization of Dox or Pyr loaded Au NP-Lyz nanocarriers

The colloidal Cit-Au NPs have overall negative charge due to the presence of citrate ions over the surfaces of NPs stabilizing them. On the other hand, Lyz is cationic at pH 7.4 (in a buffer medium). The opposite charges could account for the observed agglomeration of an aqueous mixture containing the NPs and the proteins. Experimentally, when Lyz was added to Cit-Au NP dispersion and incubated for 30 min, the color of the medium changed from bright red to purple.

UV-visible extinction spectrum of the Cit-Au NP dispersion consisted of a surface plasmon resonance (SPR) peak in the visible region with a maximum extinction (0.83) at 521 nm (**Figure 3.1 a and b**). On the other hand, in the presence of 1.43 μg mL^{-1} Lyz, the maximum extinction (with a value of 0.59) was observed at 598 nm (**Figure 3.1 a and b**). The changes in color and the extinction maximum (λ_{max}) are typical signatures of formation of agglomerates consisting of Au NPs and the protein, the details of which are available elsewhere.[59, 67-69]

Further, these agglomerated structures were treated with either Dox (hydrophilic) or Pyr (hydrophobic) molecules and then incubated in dark for 30 min. Addition of Dox further shifted the λ_{max} of SPR by 19 nm, while addition of Pyr led to a change of λ_{max} by 12 nm. The changes in the extinction wavelengths are indicative of interaction of the agglomerates with the added molecules (**Figure 3.1 a and b**). Additionally, the smallness of the change in the SPR spectra also indicated that there were no major alterations of the agglomerated structures present in the medium and these structures may be robust. However, their long term stability needs to be achieved in order for their use in therapy. In order to address the issue of stability of the loaded agglomerates, albumin (BSA) was added and the dispersion was pelleted and redispersed in 0.1 % (w/v) BSA solution after wash. On the addition of albumin to Dox loaded agglomerates or Pyr loaded agglomerates, the extinction spectra changed by 1 nm or 2 nm respectively (**Figure 3.1 a and b**). This could be due to change in extinction coefficient (i.e. dielectric function of the medium, complex dielectric function of the surface coating and the volume fraction occupied by the surface coating) of the agglomerated Au NPs.[98] Further, it is important to note that addition of BSA and centrifugation and then redispersion did not seem to change the basic structure of the agglomerates. This is quite important not only for their robustness but also for their utility.

DLS-based particle size analysis indicated that addition of Lyz to Cit-Au NPs led to shifting of the particle size distribution curve significantly, representing higher average size of the resultant particles (**Figure 3.1 c and d**). For example, the average hydrodynamic diameter of the as-synthesized Cit-Au NPs was measured to be about 19 nm. Addition of Lyz resulted in an average size of about 116 nm. On

addition of Dox the curve shifted further, indicating additional increase in the particle size. The average hydrodynamic diameter after Dox loading was found to be 195 nm. On the other hand, such change in particle size was not significant when Pyr was added to the dispersion medium. The average hydrodynamic diameter after Pyr loading was measured to be 110 nm. It is important to mention here that Dox as well as Pyr was added prior to addition of albumin. The DLS results indicated that the nanostructures consisting of agglomerates of Cit-Au NPs and Lyz behaved differently in the presence of hydrophilic and hydrophobic molecules. In other words, in the presence of hydrophilic molecules, the overall particle size of the Au NP-Lyz agglomerates increased significantly; however, in the presence of hydrophobic molecules changes in the sizes were minimal. That their resultant sizes were different possibly indicated different way of incorporation of hydrophilic and hydrophobic molecules.

A closer analysis of the distribution curves (**Figure 3.1 c and d**) revealed that upon addition of Dox to Au NP-Lyz agglomerates, the particle sizes representing the distribution increased by a constant factor of 1.62. In other words, the individual particle sizes representing the Dox loaded Au NP-Lyz agglomerates were simple multiple of individual particle sizes representing the Au NP-Lyz agglomerates. This indicated that the increase in the particle sizes, upon addition of Dox, was not due to the formation of larger agglomerates from smaller ones; however, this was due to changes in the volumes of the Au NP-Lyz agglomerated particles in the presence of Dox. Interestingly, constant and proportionate change in the volume also indicated that uptake of Dox by the Au NP-Lyz agglomerates was proportional to its volume. On the other hand, Pyr possibly entered the hydrophobic pockets which did not alter the size of the Au NP-Lyz agglomerates. However, the observed shift in the λ_{max} of SPR could be due to closer packing of the Au NPs within the same agglomerated structure, following interaction of Au NP-Lyz agglomerates with Dox or Pyr. Upon addition of albumin, no significant shift in the particle size distribution was observed (**Figure 3.1 c and d**) and the average hydrodynamic diameters were found to be 214 nm (for Dox loaded nanocarriers) and 125 nm (for Pyr loaded nanocarriers). However, after

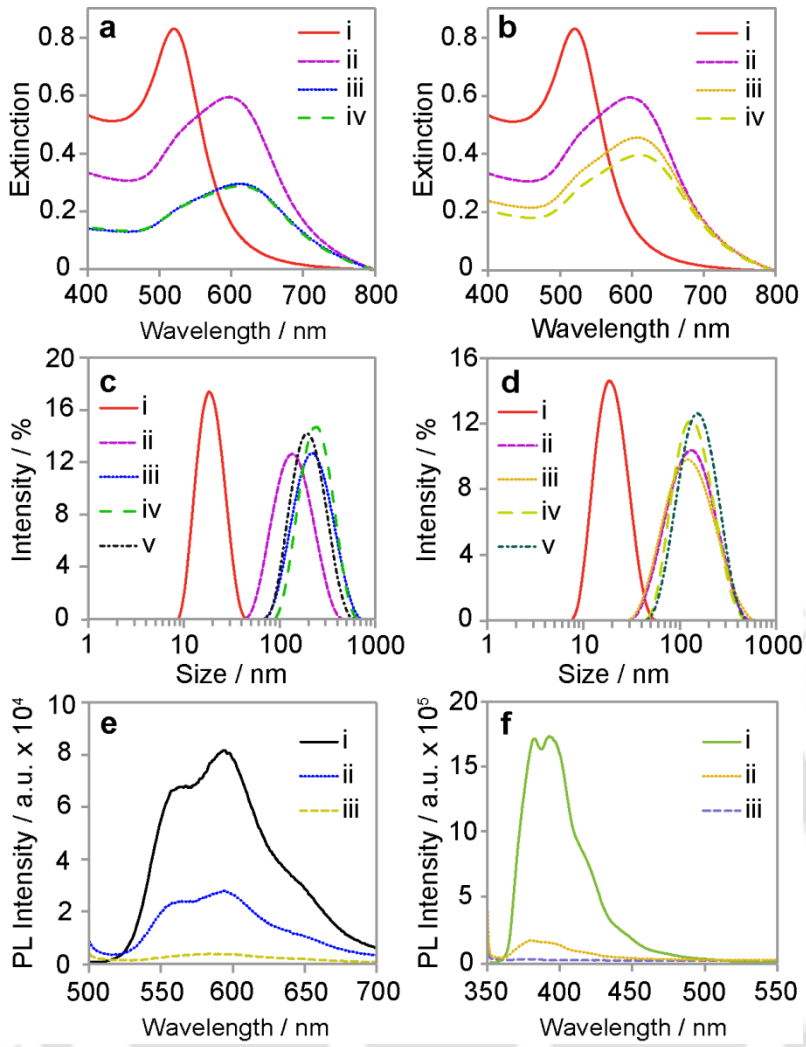

Figure 3.1 Characterization of Dox/Pyr loaded Au NP-Lyz nanocarriers. (a) UV-visible extinction spectra of (i) Cit-Au NPs, (ii) Cit-Au NPs + Lyz, (iii) Cit-Au NPs + Lyz + Dox and (iv) Cit-Au NPs + Lyz + Dox + BSA. (b) UV-visible extinction spectra of (i) Cit-Au NPs, (ii) Cit-Au NPs + Lyz, (iii) Cit-Au NPs + Lyz + Pyr and (iv) Cit-Au NPs + Lyz + Pyr + BSA. (c) DLS-based particle size distribution curves of (i) Cit-Au NPs, (ii) Cit-Au NPs + Lyz, (iii) Cit-Au NPs + Lyz + Dox, (iv) Cit-Au NPs + Lyz + Dox + BSA (before centrifugation) and (v) Cit-Au NPs + Lyz + Dox + BSA (after centrifugation). (d) DLS-based particle size distribution curves of (i) Cit-Au NPs, (ii) Cit-Au NPs + Lyz, (iii) Cit-Au NPs + Lyz + Pyr, (iv) Cit-Au NPs + Lyz + Pyr + BSA (before centrifugation) and (v) Cit-Au NPs + Lyz + Pyr + BSA (after centrifugation). (e) Emission (λ_{ex} = 480 nm) spectra of (i) Dox, (ii) Dox + Cit-Au NPs + Lyz and (iii) Dox + Cit-Au NPs. (f) Emission (λ_{ex} = 334 nm) spectra of (i) Pyr, (ii) Pyr + Cit-Au NPs + Lyz and (iii) Pyr + Cit-Au NPs.

centrifugation, the average hydrodynamic diameters of the Dox loaded nanocarriers and Pyr loaded nanocarriers, both stabilized by BSA, shifted to 183 nm and 128 nm respectively. Thus, we have a nanocarrier where the agglomeration of Cit-Au NPs and Lyz formed the basis of the structures, which

could incorporate hydrophilic and hydrophobic molecules. The attachment of hydrophilic molecules to the nanostructures led to their volume changes, while the incorporation of hydrophobic molecules did not change the volume. The albumin present in the medium provided stability to the structures without changing their diameters. Importantly, it has been reported that nanocarriers (such as liposomes) of less than 400 nm can easily extravasate through the leaky regions of the tumor vasculature,[115] although there are reports of higher extravasation efficiency for particles of less than 200 nm in diameters.[1] In the present system, DLS-based particle size measurements showed that ~98 % of the drug loaded nanocarriers were below 400 nm in sizes (**Figure 3.1 c**), with average hydrodynamic diameter being 183 nm, as mentioned before. Hence, our reported nanocarriers also meet the size criterion of efficient extravasation for favorable delivery of drugs to tumor cells.

Fluorescence spectroscopic investigations indicated specificity of interactions between the Au NP-Lyz agglomerated structures and the hydrophilic and hydrophobic molecules. For example, when excited by 480 nm light Dox emits at 560, 595 and 650 nm (**Figure 3.1 e**). In the presence of Au NP-Lyz agglomerates (containing 1.29 nM Cit-Au NPs and 1.43 μg mL^{-1} Lyz) the intensity of all the emissions decreased by about 66 % (**Figure 3.1 e**). The Dox concentration used was 0.89 μg mL^{-1}. On the other hand, Pyr has prominent emission peaks at 375, 396, 416 and 444 nm, when excited by 334 nm light (**Figure 3.1 f**). The intensity of all the peaks was reduced by nearly 92 % in the presence of the agglomerates (**Figure 3.1 f**). The relatively more significant decrease in the presence of Pyr in comparison to that in the presence of Dox indicated specificity of interactions. Dox is hydrophilic and highly soluble in water and Pyr being hydrophobic is lowly soluble. Dox, having both the hydrophilic and hydrophobic (aromatic hydroxyanthraquinone ring) groups, may interact with both the hydrophilic and hydrophobic sites of the proteins in the agglomerated structures.[116, 117] As a result, some of the Dox molecules may interact with the exposed hydrophilic sites and some may be buried inside the hydrophobic site. However, Pyr - having only hydrophobic interactions - may be buried deep inside the hydrophobic regions.[118] This means Dox molecules would primarily be further away from Au

NPs, which would be buried inside, while Pyr would be closer to the NPs. Since, Au NPs are efficient in quenching fluorescence of both the species (**Figure 3.1 e and f**) the difference in extent of quenching by the same amount of Au NPs in the agglomerates clearly evidenced different interactions owing possibly to differences in the distance between Au NPs and the fluorophore.

TEM measurements further supported the formation of agglomerated nanostructures as the basis of the nanocarriers. First of all, that the individual well-separated NPs of Au (**Figure 3.2 a**) were agglomerated in the presence of protein (Lyz) was evident from the TEM image shown in **Figure 3.2 b**. While the average individual particle sizes were 15.4 ± 1.4 nm, the agglomerated structures consisting of several particles appeared to be more than 200 nm. However, since the observed structures were obtained after evaporation of the dispersion, it is plausible that in the liquid medium the sizes were much less in diameters. On the other hand, TEM images of Dox and Pyr loaded agglomerates, followed by

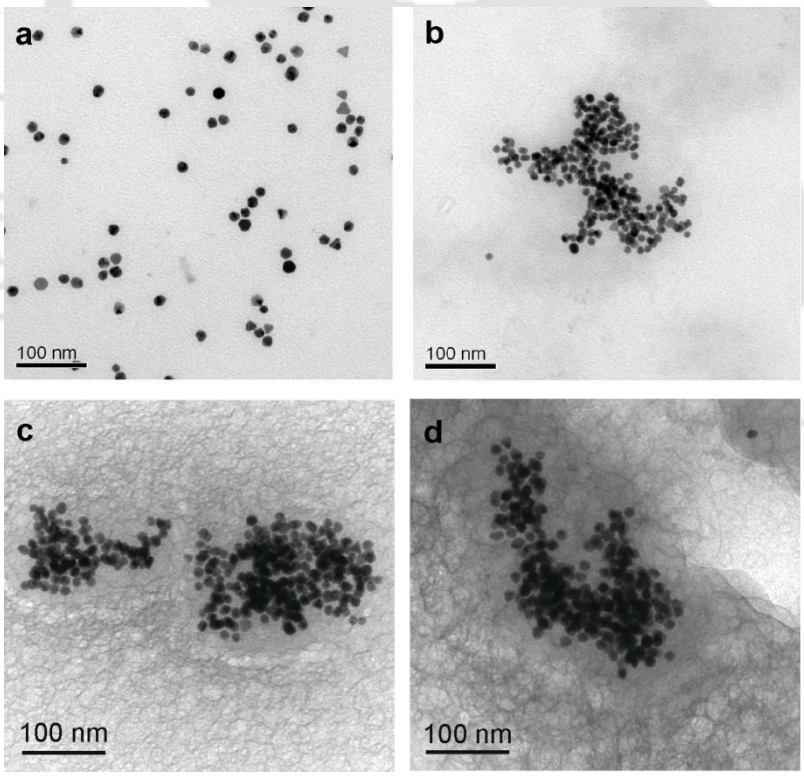

Figure 3.2 TEM micrographs of (a) as-synthesized Cit-Au NPs, (b) Cit-Au NPs in presence of Lyz (c) Dox loaded Au NP-Lyz nanocarriers and (d) Pyr loaded Au NP-Lyz nanocarriers.

albumin treatment also retained the basic structures, indicating the presence of nanostructures in the medium (**Figure 3.2 c and d**). Overall, TEM studies revealed the presence of agglomerated structures at various steps of nanocarrier fabrication. The presence of nanoscale agglomerates of Au NPs in the final structures evidenced the basis of the nanocarrier development consisting of various components.

UV-visible and fluorescence spectroscopy along with DLS – as detailed above – clearly indicated that the loaded nanocarriers contained Au NPs and Dox or Pyr, whichever was introduced into the medium. In order to have a clearer picture of the structure of the nanocarrier it was deemed important to probe the presence of proteins which were used in their fabrication. The presence of Lyz and albumin in the nanocarriers was confirmed by SDS-PAGE. The results are shown in **Figure 3.3.** Lane 3 in the picture corresponds to the nanocarrier sample. As is clear from the figure, there are two prominent bands in Lane 3; one is due to 14.3 kDa protein (when compared with that in Lane 2), while the other one is due to 66.4 kDa protein (when compared with that in Lane 4). The sample in Lane 2 corresponded to Lyz and that in Lane 4 was BSA. Further, the appearance of additional bands in Lane 3, below the legitimate protein bands, could be due to fragments owing to proteolytic cleavage in the presence of Au NPs in the nanocarriers. The nanocarrier sample (containing Au NPs and proteins) was treated with different denaturing agents and was boiled before running the gel; this could result in degradation of proteins to smaller fragments especially in the presence of Au NPs. The bands corresponding to lower molecular weights were observed with better clarity in the silver-stained gel (**Figure 3A.1,** *Appendix*). Further, no band was observed in Lanes 5 and 6, corresponding to that of Cit-Au NPs and Dox respectively. Overall, spectroscopic, light scattering, TEM and electrophoretic analysis indicated that the fabricated nanocarriers consisted of Au NP-Lyz agglomerates, BSA and the payload (Dox or Pyr) which was incorporated in them. The results also match with an idealized picture of the loaded nanocarrier as depicted in **Scheme 3.1 a** i.e. firstly the agglomerated nanostructures of Au NPs and Lyz were formed in the medium; which was followed by incorporation of the payload and then finally capped with a stabilizer albumin. The presence of excess albumin in the medium also added to the stability of the nanocarriers.

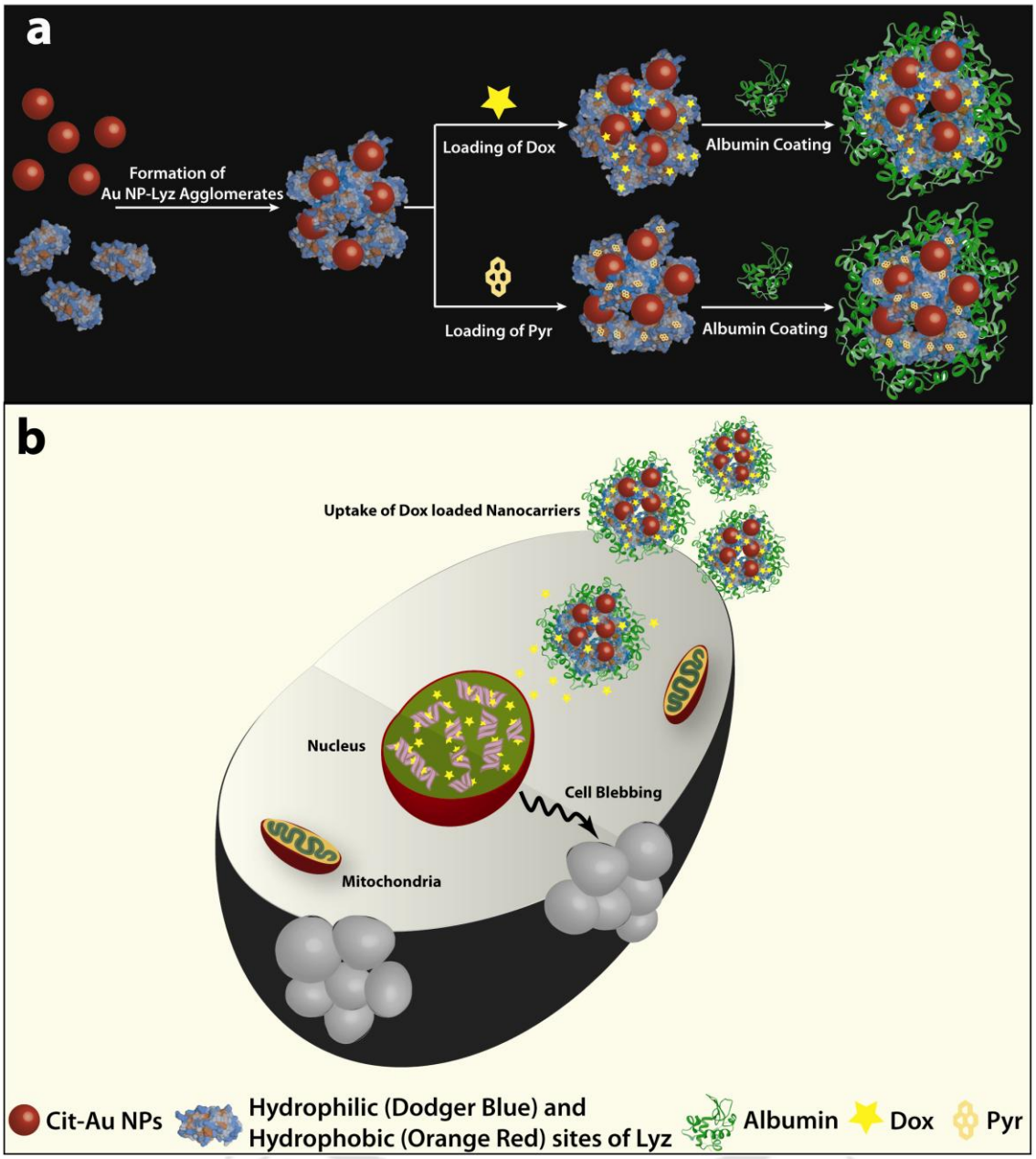

Scheme 3.1 A schematic representation of the generation of Dox/Pyr loaded nanocarriers, their uptake followed by release of the payload inside the cancerous cell leading to apoptosis. (a) Dox/Pyr loaded nanocarriers were generated following three steps – formation of Au NP-Lyz agglomerates, loading of hydrophilic Dox or hydrophobic Pyr molecules and finally coating with an albumin layer to stabilize the nanostructures. The structure of Lyz (PDB ID: 1HEL) was imported from RCSB Protein Data Bank and the hydrophilic and hydrophobic sites were marked using Chimera 1.5.3 software and (b) Representation of internalization of Dox loaded nanocarriers by the HeLa cell and the release of payload subsequently triggering apoptosis by DNA damage leading to cell blebbing.

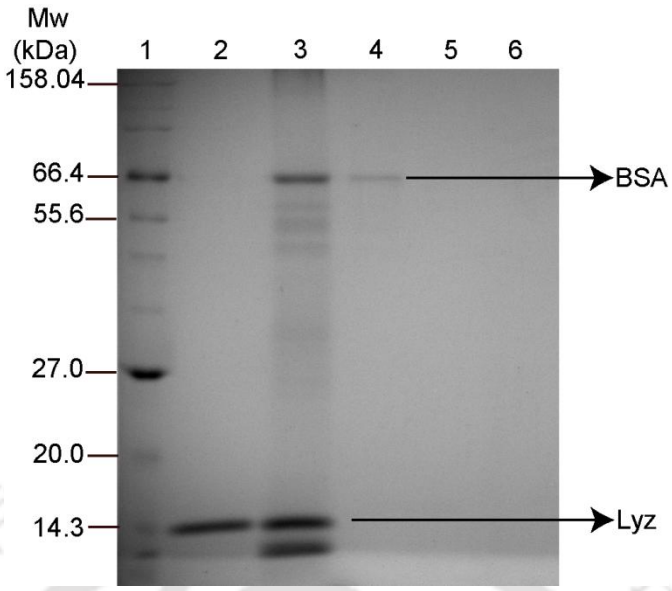

Figure 3.3 SDS-PAGE analysis of nanocarrier. Lanes corresponding to 1: New England Biolabs Protein marker; 2: Lyz; 3: Nanocarrier; 4: BSA; 5: Cit-Au NPs and 6: Dox. The molecular weights of the proteins in the marker used are reported on the left for reference.

Although DLS studies clearly substantiated the formation of nanocarrier in the presence of its payload, its stability is also of paramount importance for practical usage. The temporal stability of the Dox or Pyr loaded Au NP-Lyz nanocarrriers was investigated by UV-visible spectroscopy. The UV-visible spectra of the nanocarriers in 0.1 % (w/v) BSA solution were recorded at several time intervals for a period of 48 h and the results are shown in **Figure 3.4 a and b** for Dox and Pyr loaded carriers respectively. As shown in the figures there were no significant changes in the extinction spectra of the loaded carriers with time (for 48 h) for both the samples. Plots (**insets of Figure 3.4 a and b**) of extinction at 598 nm (for Dox loaded sample) and 586 nm (for Pyr loaded sample) indicated virtually constant extinction at values 1.0 for Dox-containing carriers and 1.1 for Pyr loaded carriers respectively. The results clearly indicated stability of the nanocarriers in the presence of both the hydrophilic and hydrophobic molecules and no further agglomeration, as would have been indicated by changes in the extinction spectra, was observed. Also, there was no observable precipitation from the medium, further supporting stability of the nanocarrier.

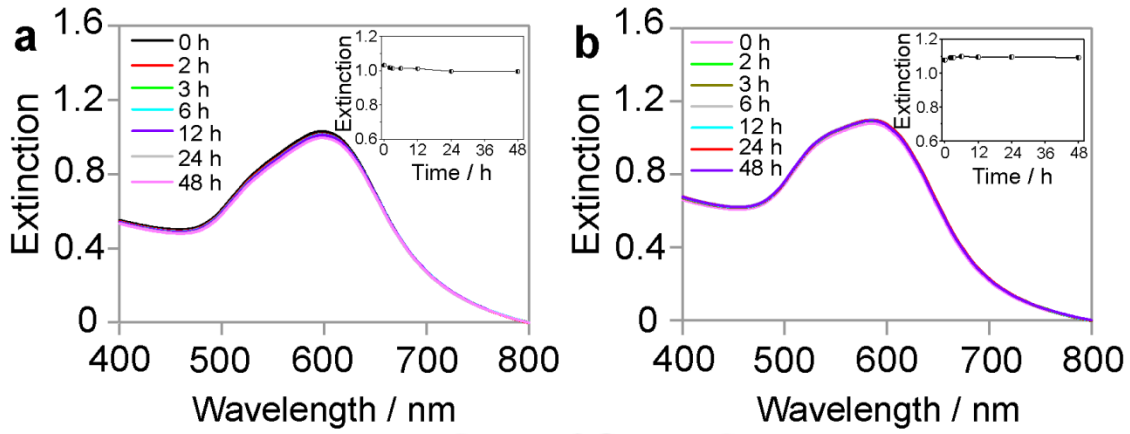

Figure 3.4 UV-visible extinction spectra of (a) Dox loaded nanocarriers and (b) Pyr loaded nanocarriers recorded at different intervals of time, as mentioned in the legends. The insets show the time dependence of extinction at 598 nm for Dox loaded nanocarriers and at 586 nm for Pyr loaded nanocarriers.

3.2.2 Loading efficiency and in vitro release of Dox/Pyr from loaded Au NP-Lyz nanocarriers

An important criterion of an efficient nanocarrier is its ability to incorporate drug molecules with high efficiency. The results described above indicated that the nanocarriers were able to incorporate both hydrophilic and hydrophobic molecules. In order to estimate the loading efficiency, fluorescence spectroscopy was used, where the emissions from Dox and Pyr were used as the probe. The results indicated that the nanocarriers loaded Dox with as much as 76.9 % and Pyr with 68.8 % efficiencies, at the Dox and Pyr concentrations in the media being 0.78 μg mL^{-1} and 0.057 μg mL^{-1}, respectively. The typically high loading efficiency for both the hydrophilic and hydrophobic molecules indicated high potential of the nanocarriers for both kinds of drugs. Proteins have both the hydrophilic and hydrophobic sites which are expected to be retained in the agglomerated structures even if there was partial unfolding of them in the presence of the NPs. Moreover, a collection of proteins in the associated structures would provide larger volumes of 'containers' for hydrophilic and hydrophobic sites, thus augmenting drug loading capacity. The ability of the nanocarriers to incorporate both types of molecules also indicated their potential to be used for combinatorial therapy, which would be of great advantage in practical applications.[119] It is noteworthy that earlier reported nanocarriers showed higher loading efficiency

for either hydrophilic or hydrophobic molecules,[35-40, 62, 119] whereas, the current nanocarriers could be loaded with both kinds with considerable capacity, pointing towards their significance in drug delivery.

The important parameter other than loading efficiency for an efficient nanocarrier would be the ability to release the drug efficiently at the target. The in vitro release studies of Dox and Pyr from the nanocarriers was pursued using the fluorescence spectroscopy. Dox as well as Pyr release was followed in acetate buffer (pH 4.0) and phosphate buffer (pH 7.4) for 24 h at 37 °C. The results of time-dependent cumulative release from Dox loaded nanocarriers are shown in **Figure 3.5 a and b**. The results indicated that cumulative release of Dox from the carriers in 24 h was 35 % at pH 4.0, while that at pH 7.4 was 27 %. The drug doxorubicin is sold as a hydrochloride salt, which is highly soluble in water. Thus

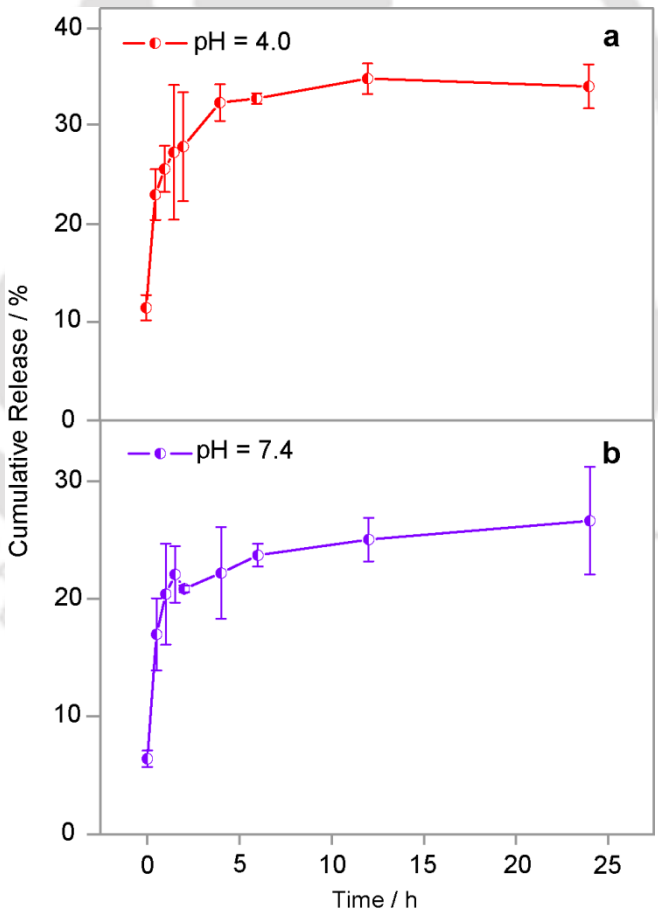

Figure 3.5 Quantitative analyses of the in vitro release of Dox at 37 °C from Dox loaded Au NP-Lyz nanocarriers over 24 h. Plots of the cumulative release (in percentage) of Dox against time (a) at pH 4.0 in acetate buffer and (b) at pH 7.4 in phosphate buffer. Data are represented as mean ± standard deviation (S.D.) of three individual experiments.

it is possible that non-covalent nature of binding between the drug and protein makes it possible for release in the medium. At lower pH the increased solubility may lead to higher release of the drug. The extent of release also indicated strong binding between the drug and the nanostructures containing Au NPs and Lyz. This would facilitate in the internalization of more amount of drug inside the cancer cells along with the nanocarriers. Interestingly, no release of Pyr was observed from the Pyr loaded nanocarriers in both the buffers (data not shown). This could be due to strong binding of Pyr in the hydrophobic regions of Au NP-Lyz agglomerates. Further, Pyr itself being hydrophobic in nature has low solubility in water. Thus the release would be low in aqueous medium when encapsulated in the nanocarrier. This is consistent with the observed results.

3.2.3 Uptake of Dox loaded nanocarriers by cancer cells

In passive as well as targeted drug delivery the uptake of drug by cells and its release from the cargo in vivo constitute the primary success of the carrier. In the present case, the uptake of the drug loaded nanocarriers was studied in vitro by incubating the HeLa cells with Dox loaded carriers for 4 h and then following the cells by TEM, flow cytometry and fluorescence microscopy. The TEM image of a treated HeLa cell (**Figure 3.6 a**) demonstrated the internalization of the

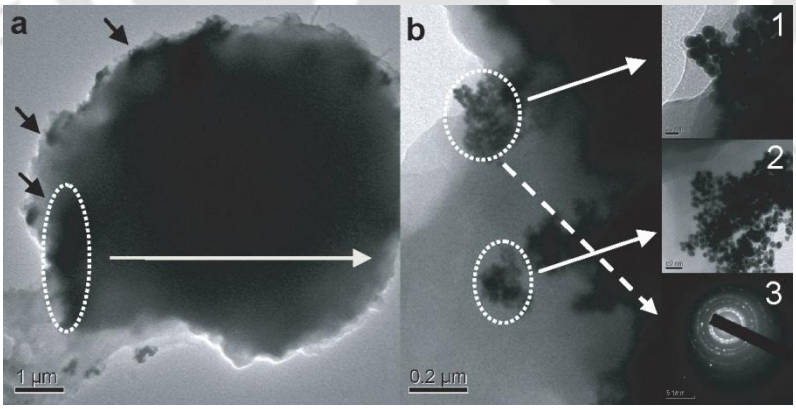

Figure 3.6 TEM micrographs showing the uptake of the Au NP-Lyz nanocarriers by the HeLa cells. (a) TEM image of a HeLa cell (treated with Dox loaded Au NP-Lyz nanocarriers for 4 h) confirming the internalization of the nanocarriers at several sites (indicated by black arrows) of the cell and (b) Magnified view of the internalized nanocarriers. The insets 1 and 2 show the further magnified view of the nanocarriers, indicating clearly the presence of NPs in the agglomerates inside the cell and inset 3 shows the SAED pattern of the nanocarriers.

nanocarriers by the cells.[40, 62] A magnified view of the carriers inside the cell (marked with a oval) is shown in **Figure 3.6 b**. On further magnification, agglomerated structures of NPs could be seen clearly (**Figure 3.6 b**, **insets 1 and 2**). The selected area electron diffraction (SAED) pattern (**Figure 3.6 b**, **inset 3**) confirmed the presence of Au NPs in the agglomerated structures present within the cells. It may be mentioned here that no such agglomerated structures or NPs were seen in the TEM image of an untreated HeLa cell (**Figure 3A.2,** *Appendix*). Interestingly, a closer analysis of **Figure 3.6 a** indicated that more than one agglomerated structures were internalized by the same cell. The results point to efficient internalization of the nanocarriers inside the cancer cells.

Flow cytometric analysis further confirmed the uptake of the Dox loaded nanocarriers by the cells. This was pursued by incubating the cells with nanocarriers and Dox loaded nanocarriers for 4 h. As Dox emits at 595 nm, the FL2 (occurring at 585 ± 21 nm) fluorescence intensity in the cytometer was monitored. For the cells incubated with 0.15 mg mL^{-1} of nanocarriers, there was no shift in the fluorescence intensity in comparison to the cells only (**Figure 3.7**). Whereas, for cells incubated with 0.15 mg mL^{-1} of Dox loaded nanocarriers (containing 0.64 μg mL^{-1} of Dox), there was a significant shift in the fluorescence intensity (**Figure 3.7**), indicating the presence of Dox inside the cells and confirming the uptake of the Dox loaded nanocarriers by the cells. Quantitative

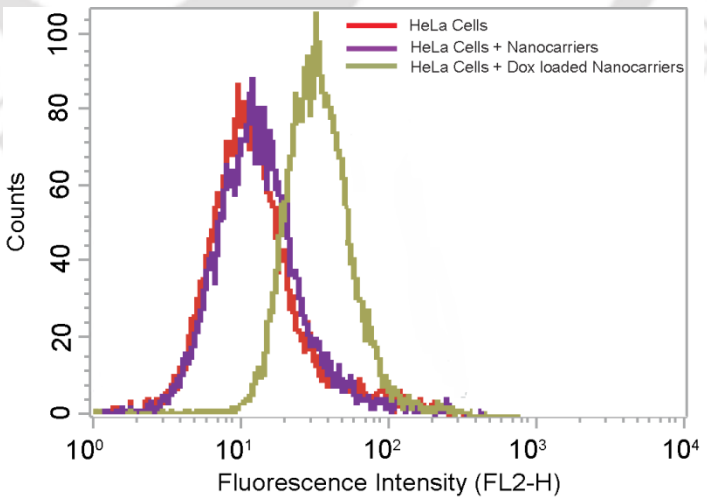

Figure 3.7 Flow cytometry results showing the FL2 fluorescence intensity of HeLa cells after incubation with nanocarriers and Dox loaded nanocarriers for 4 h.

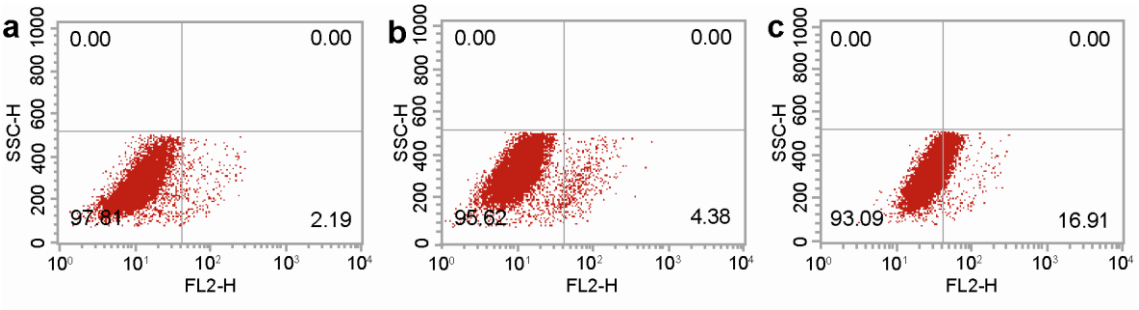

Figure 3.8 FACS results. Dot plots of (a) HeLa cells only, (b) HeLa cells incubated with nanocarriers for 4 h and (c) HeLa cells incubated with Dox loaded nanocarriers for 4 h, with percentage of gated cell population in each quadrant. All data were gated on a population of live cells determined by side scatter vs forward scatter.

cellular uptake studies using FACS are shown in **Figure 3.8**. In the second quadrant (which is FL2 positive), the percentage of gated cell population increased from 2.2 to 4.4 when the HeLa cells were treated with nanocarriers (**Figure 3.8 a and b**). Whereas, for HeLa cells treated with Dox loaded nanocarriers, the percentage of gated cell population in the second quadrant increased to 16.9 (**Figure 3.8 c**). This demonstrates that almost 14.7 % of cells were Dox positive as compared to HeLa cells only. That the nanocarriers were internalized by the cells and the drug Dox was present in those carriers were evident from the cytometry studies.

Further, fluorescence microscopic studies revealed the presence of Dox in the HeLa cells after treatment with Dox loaded nanocarriers for 4 h. Red fluorescence, corresponding to emission from Dox, was observed in the whole cell encompassing cytoplasm and nucleus (**Figure 3.9 a-c**). However, understanding of detailed mechanism of uptake of the carriers by the cells and release of the drug from the nanocarriers needs further investigations, which is beyond the scope of the present study. It is plausible that Dox was released from the nanocarriers into the cytoplasm and subsequently was localized in the nucleus. Indentations, indicative of early apoptotis, were observed in the Dox loaded nanocarrier treated HeLa cells. This was further corroborated by FESEM results as discussed subsequently. Thus the microscopy studies indicated possible internalization of the Dox in the nucleus in 4 h. Similarly, red fluorescence was also observed for the HeLa cells treated with Dox only (**Figure 3.9 d-f**), indicating its possible

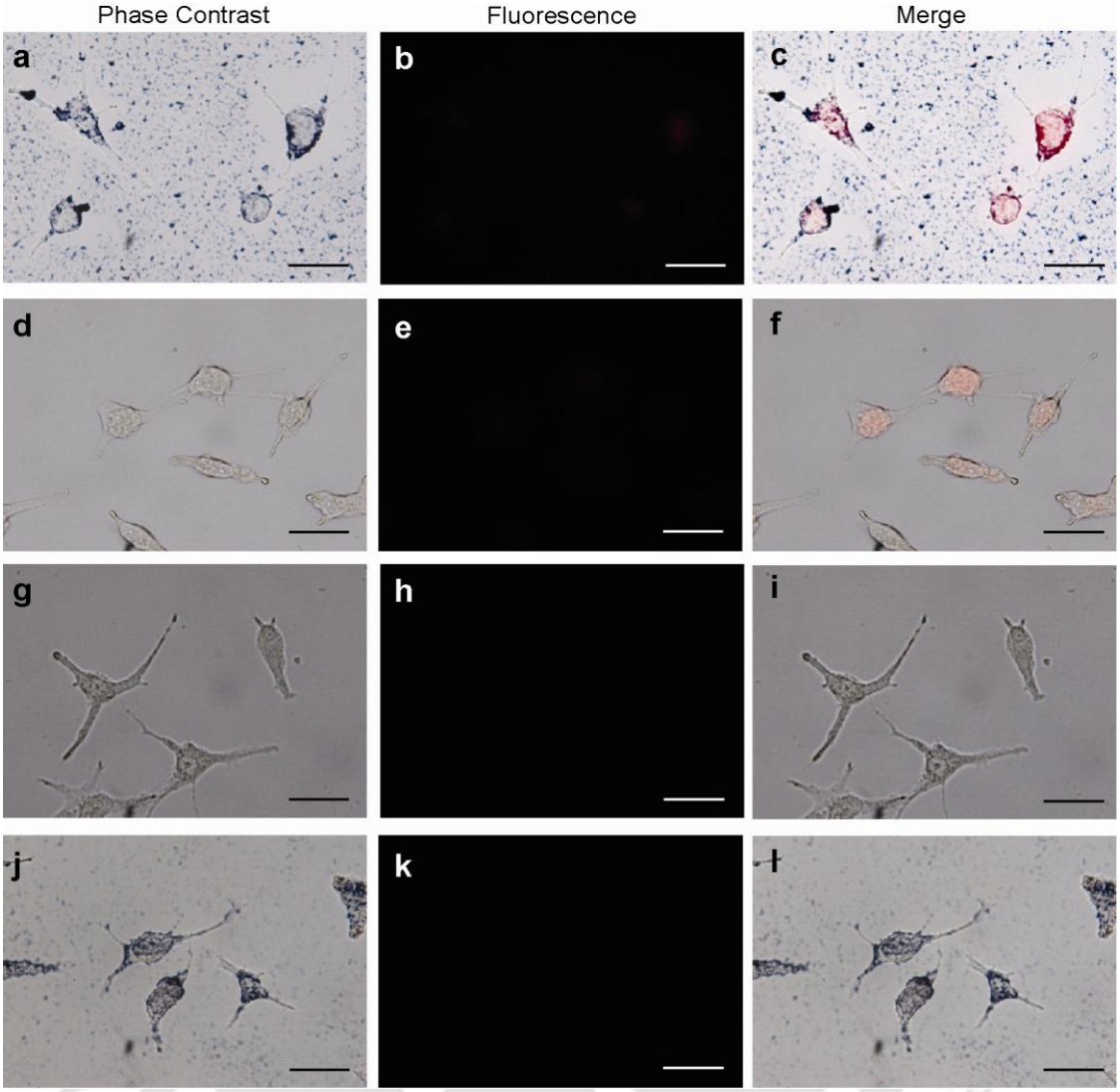

Figure 3.9 Microscopic images of (a, b, c) HeLa cells treated with Dox loaded nanocarriers for 4 h, (d, e, f) HeLa cells treated with Dox only for 4 h, (g, h, i) untreated HeLa cells and (j, k, l) HeLa cells treated with nanocarriers for 4 h. Scale bar: 50 μm.

internalization. However, no such emission was observed for the untreated HeLa cells (**Figure 3.9 g-i**) and HeLa cells treated with nanocarriers (**Figure 3.9 j-l**). The results confirmed the uptake of the Dox loaded nanocarriers by the HeLa cells and the release of the drug into the cells.

3.2.4 Consequence of the drug release from the drug loaded nanocarriers

The consequence of the drug release from the drug loaded nanocarriers inside the cells was investigated by cell viability assay and FESEM. For cell viability assay, HeLa cells were incubated with nanocarriers, Dox only and Dox loaded

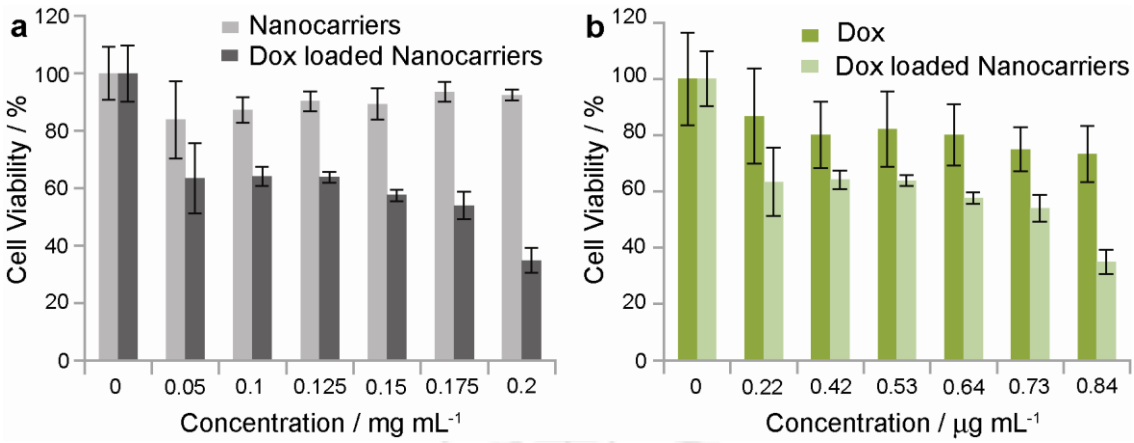

Figure 3.10 XTT based cell viability assay of HeLa cells after 24 h treatment with (a) Au NP-Lyz nanocarriers and Dox loaded Au NP-Lyz nanocarriers at varying concentrations of the nanocarriers and (b) free Dox and Dox loaded nanocarriers at varying doxorubicin concentrations. Data are represented as mean ± S.D. of three individual experiments.

nanocarriers for 24 h. **Figure 3.10 a** shows the cell viability assay at varying concentration of nanocarriers and Dox loaded nanocarriers. It was observed that, when the cells were incubated with 0.2 mg mL^{-1} of the nanocarriers, more than 90 % of the cells were viable, indicating that the nanocarrier itself was non-toxic in nature. Whereas, after treating the HeLa cells with Dox loaded nanocarriers, the cell viability decreased to 63 % even at 0.05 mg mL^{-1} nanocarriers. At the highest concentration of 0.2 mg mL^{-1} of loaded nanocarriers, the cell viability drastically decreased to 35 %. These results proved that the non-toxic nanocarriers, when loaded with the drug Dox, were able to kill cancer cells efficiently. In order to compare the effect of free Dox and the Dox loaded nanocarriers, cell viability assay at varying concentration of Dox was performed. **Figure 3.10 b** shows the comparative account of the effect of free Dox and the Dox loaded nanocarriers on the cancer cells. At the 0.64 µg mL^{-1} concentration of free Dox, the cell viability reduced only to 80 %, whereas, at the same concentration of Dox loaded in the nanocarriers, were able to reduce the viability to 57 %. Additionally, at the highest concentration of Dox (0.84 µg mL^{-1}) used in the present case, free Dox was able to reduce the viability to ~74 %, whereas, the loaded nanocarriers (with equivalent concentration of Dox i.e. 0.84 µg mL^{-1}) showed efficient killing of cells with viability of 35 %. This drastic decrease in the cell viability compared to Dox only indicated the enhanced killing of cancer cells by the Dox loaded nanocarriers and

confirming the release of Dox from the nanocarriers in the cellular environment. The above results also suggested that the nanocarrier itself was non-cytotoxic and the Dox loaded nanocarrier was more cytotoxic as compared to equivalent concentration of Dox (only) as loaded in the nanocarrier. This could be due to effective concentration of Dox, carried to the cells upon loading in the nanocarrier; in comparison to Dox (only) added to the cell culture medium. Moreover, as reported previously by Zhang et al., the synergy of Au NPs and the drug, could contribute to the overall increase in cell death efficiency when delivered through the carrier.[40] The internalization of loaded nanocarriers probably helped in releasing more amount of Dox inside the cells.

The morphological changes, as a result of drug release into the cells, were observed by FESEM measurements. Dox is known to interact with DNA by intercalation between base pairs and it inhibits macromolecular biosynthesis causing cell death.[120] The FESEM image of a HeLa cell treated with Dox loaded nanocarriers for 4 h (**Figure 3.11 a**) showed the formation of apoptotic bodies, which is indicative of apoptotic cell death caused by Dox.[121] No such apoptotic bodies were seen in the FESEM image of an untreated HeLa cell (**Figure 3.11 b**). It is to be mentioned here that all the cell experiments were performed using Dox loaded nanocarriers unless otherwise mentioned. The observations with respect to uptake of the drug loaded nanocarriers by the HeLa cell and consequent release of Dox into the cells match well with the scheme as shown in **Scheme 3.1 b**.

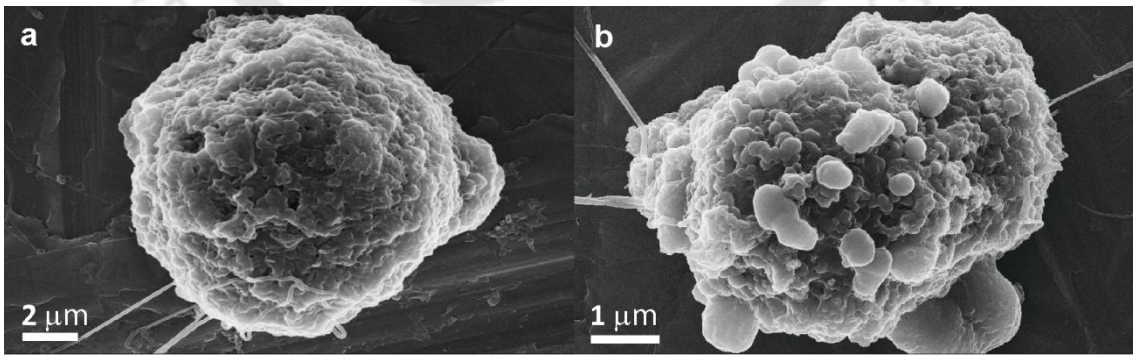

Figure 3.11 FESEM images of (a) untreated HeLa cell and (b) Dox loaded Au NP-Lyz nanocarriers treated (for 4 h) HeLa cell.

3.3 Conclusions

In summary, we have been able to develop a novel nanocarrier for efficient drug delivery to cancer cells, based on Au NP-Lyz agglomerated structures - which were coated with albumin. The nanocarrier was biocompatible and non-toxic to the cells. The carrier was able to load both hydrophilic and hydrophobic molecules with high efficiency. Experiments in vitro revealed that the nanocarriers were internalized by the cancer cells and at the same time they released their payloads within the cells leading to cell death, which was more efficient than by using drug molecule only. The incorporation of albumin points to its potential utility in facilitating intratumor accumulation of albumin bound nanocarriers. The presence of agglomerated Au NPs, in the nanocarriers, with extinction extending to NIR, can further be exploited for the photodynamic release of the payloads from the carriers. Also, their versatility in encapsulating both hydrophilic and hydrophobic molecules can potentially be applicable for combinatorial therapy.


NANO
small
MICRO
Nanocarriers
The fabrication of a versatile nanocarrier, based on agglomeration of Au nanoparticle and lysozyme in aqueous medium, is reported on page 3494 by A. Chattopadhyay and co-workers. The nanocarrier is biocompatible, stable, and can incorporate hydrophilic as well as hydrophobic molecules with high efficacy via non-covalent interactions, rendering it a valuable drug delivery vehicle. Coating with an albumin layer not only increases the stability but also facilitates its uptake by cancer cells. A cell viability assay in vitro demostrates that the anticancer drug doxorubicin can be delivered to HeLa cells with high efficiency, in comparison to the free drug, for achieving apoptotic cell death. Overall, the capability of the nanocarrier for drug loading and release makes it a promising candidate for multimodal drug delivery, with the possibility of photodynamic therapy.
20/2013
WILEY-VCH
Gold Nanoparticle–Protein Agglomerates as Versatile Nanocarriers for Drug Delivery
A. Chattopadhyay and co-workers

CHAPTER 4

Polymer coated Gold Nanoparticle-Protein Agglomerates as Nanocarriers for Hydrophobic Drug Delivery

While Chapter 3 described the use of gold nanoparticle (Au NP)-lysozyme (Lyz) agglomerates for hydrophilic drug delivery, this chapter focuses on the utilization of the agglomerates for hydrophobic drug delivery along with increasing the stability of the drug loaded Au NP-Lyz agglomerates against protease degradation in the presystemic circulation. This was done by coating of the drug loaded agglomerates with a biodegradable polymer poly(lactic-co-glycolic acid) (PLGA) via oil in water single emulsion process. The nanocarrier was also found stable in human blood serum and meets the size criterion for the enhanced permeability and retention (EPR) effect even after having a coating of polymer around the agglomerates. Here, the encapsulation and delivery of the hydrophobic drug camptothecin (CPT) – which is otherwise difficult to deliver as a stable species – using the Au NP-protein agglomerates is demonstrated. The internalization of these nanocarriers was proved using transmission electron microscopy (TEM) and confocal microscopy. MTT based cell viability assay confirmed that the nanocarriers (non-loaded) themselves were not significantly toxic to the HeLa cells, but when loaded with the drug CPT, killed the cancer cells efficiently through apoptosis. These nanocarriers have the potentiality to find use in clinical applications.

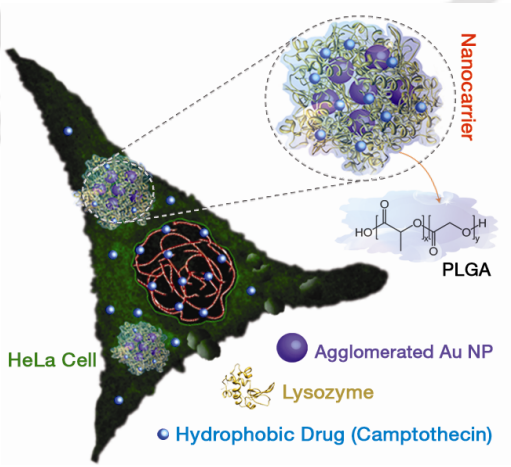

*[Rumi et al. *J. Mater. Chem. B* 2014, *2*, 6472–6477] - Reproduced by permission of The Royal Society of Chemistry
http://pubs.rsc.org/en/Content/ArticleLanding/2014/TB/c4tb00800f#!divAbstract

4.1 Experimental Section

4.1.1 Materials

Hydrogen tetrachloroaurate trihydrate, $HAuCl_4.3H_2O$ (Sigma-Aidrich Co., USA), (S)-(+)-camptothecin (CPT; Sigma-Aidrich Co., China), poly(D,L-lactide-co-glycolide), acid terminated, 50:50, MW: 7000-17000 Da (PLGA; Sigma-Aidrich Co., Germany), hen egg white lysozyme (Lyz; SRL, India), 3-(4,5-dimethylthiazol-2-yl)-2,5-diphenyltetrazolium bromide (MTT; Himedia, India), Proteinase K (Bioline, UK), calcein AM (Fluka, USA) and trisodium citrate dihydrate (Merck, India) were purchased and used as received without any further purification. Milli-Q ultrapure water (>18 MΩ cm, Millipore) was used in all the experiments.

4.1.2 Synthesis of citrate-stabilized Au NPs (Cit-Au NPs)

The dispersion of Cit-Au NPs was obtained via citrate reduction of $HAuCl_4$.[111] Briefly, Milli Q grade water (100 mL) containing trisodium citrate dihydrate (0.0034 M) was refluxed under stirring condition. When the solution started boiling highly, $HAuCl_4$ (1 mL of 1.73×10^{-2} M) was added and the reaction was allowed to continue for another 30 min. This resulted in the formation of dispersion of Cit-Au NPs. The concentration of Cit-Au NPs formed at this stage was calculated to be 1.51 nM, assuming that complete reduction of $HAuCl_4$ has occurred. In order to separate out the larger particles, the above dispersion was centrifuged at 2000 rcf and 10 °C for 15 min. The supernatant (referred as Cit-Au NPs hereafter in this chapter) was collected and used in all the experiments, as applicable.

4.1.3 Development and characterization of PLGA coated nanocarriers

The dispersion of Cit-Au NPs (15 mL) was mixed with Lyz (1.2 mL of 0.01 mg mL^{-1}) and incubated for 30 min. The Lyz solution was prepared in sodium phosphate buffer (0.01 M) of pH 7.4. The pH of the resulting Au NP-Lyz dispersion was found to be ~6.9. To this, the solution of CPT in DMSO (0.04 mL of 0.5 mg mL^{-1}) was added and incubated in dark for another 1 h. After this, the above solution was emulsified with PLGA (pK_a 3.85) in DCM (1 mL of 5 mg mL^{-1}), using the microtip probe sonicator (UP200S ultrasonic processor, hielscher), set at cycle 0.5 and amplitude 40 % for 2 min, to form oil in water single emulsion. The

emulsified solution was allowed to mix gently in a rocker for 4 h and then the DCM was evaporated using the water bath maintained at 40 °C for 2 h. Finally, the dispersion was centrifuged (20000 rcf, 4 °C for 15 min) and the pellet was washed twice. The resulting pellet was redispersed in water using an ultrasonic bath.

The characterization of the nanocarriers was done using the double beam UV-visible spectrophotometer (Hitachi U-2900), DLS-based particle size analyzer (Zetasizer Nano ZS90, Model No. ZEN3690, Malvern) and transmission electron microscope (JEOL JEM 2100, maximum accelerating voltage 200 kV).

4.1.4 Stability tests against proteases

The stability of the nanocarriers against protease degradation was tested via SDS-PAGE and TEM analysis. PLGA coated nanocarriers were prepared in duplicate, centrifuged, washed and both the pellets were redispersed together in 60 μL of water. As a control, Au NP-Lyz agglomerates (without PLGA coating) and albumin coated nanocarriers (as mentioned in Chapter 3) were also prepared and the pellet after centrifugation and several washings were redispersed in 30 μL of water separately. The solutions of PLGA coated nanocarriers, albumin coated nanocarriers, Lyz and albumin were mixed individually with Proteinase K and incubated at 37 °C in a shaking water bath for 1 h. After this, the solutions were immediately boiled for 10 min to stop the reaction. The above solutions along with the solutions which were not subjected to protease treatment were boiled again with loading buffer for 5 min and then loaded in polyacrylamide gel (16 %). After the completion of electrophoresis, the gel was stained (using coomassie brilliant blue R-250), destained and then photographed (using Gel Logic 212 PRO Imaging System, Carestream). The details of the samples used in different lanes of **Figure 4.4 a**, **Figure 4.4 b** and **Figure 4.4 c** are given in **Table 4A.1**, **4A.2** and **4A.3** (*Appendix)* respectively. The PLGA coated nanocarriers or albumin coated nanocarriers with (500 ng) and without protease treatment were also observed under transmission electron microscope.

4.1.5 Stability of the PLGA coated nanocarriers in human blood serum and in water

The concentrated dispersion of PLGA coated nanocarriers were equally diluted

with human blood serum as well as with water and their extinction spectra were recorded at different time intervals. It is important to mention here that the nanocarriers diluted with serum were stored at 37 °C and nanocarriers diluted with water were stored at 4 °C.

4.1.6 Encapsulation efficiency (E.E.) and in-vitro cumulative release (C.R.) study

The PLGA coated nanocarriers were prepared, centrifuged (at 20000 rcf and 4 °C for 15 min) and the pellet was washed twice. The supernatant of the initial step was mixed with the supernatants of the washing steps and its emission spectrum was recorded in a HORIBA Jobin Yvon FluoroMax-4 spectrofluorimeter by exciting at 370 nm. The emission at 434 nm was noted and the concentration of the CPT in the supernatant was calculated using the standard curve of CPT. Then the E.E. was calculated using the formula:

$$E.E.\ \% = \frac{CPT_i - CPT_s}{CPT_i} \text{x}100 \qquad (4.1)$$

where, $[CPT]_i$ is the initial concentration of CPT and $[CPT]_s$ is the concentration of CPT in the supernatant.

Generation of standard curve of CPT for E.E. study

Considering that the supernatant may contain moieties which may have influence on the fluorescence profile of CPT, the standard curve for calculating $[CPT]_s$ (the concentration of CPT in the supernatant) was made by dissolving different concentrations of CPT in the supernatant (obtained after the centrifugation and washing of non-loaded nanocarriers) and recording their emission spectrum by excitation at 370 nm. The intensity at 434 nm was noted and the standard curve of emission intensity vs concentration was obtained.

For in vitro cumulative release study, the PLGA coated nanocarriers were prepared, centrifuged and washed. Finally the pellet was redispersed in acetate buffer (0.02 M, pH 4.0), phosphate buffer (0.02 M, pH 7.4) and DMSO, separately respectively. Then the respective dispersion of nanocarriers were equally distributed in different centrifuge tubes and incubated in a shaking water bath

maintained at 37 °C for 24 h. At different intervals of time, the centrifuge tubes were taken out, centrifuged and the supernatants were collected whose emission intensities were measured at 434 nm, by exciting the samples at 370 nm in a fluorimeter. By knowing the emission intensities, the concentrations of CPT released in the supernatants were calculated using the standard plot of CPT. Then, the cumulative release were obtained using the formula:

$$C.R.\ \% = \frac{CPT_{s}}{CPT_{l}} \text{X}100 \qquad (4.2)$$

where, $[CPT]_s$ is the concentration of CPT released in the supernatant and $[CPT]_l$ is the concentration of CPT encapsulated in the nanocarriers. Similarly the cumulative releases in phosphate buffer and in DMSO were calculated.

Generation of standard curve of CPT for C.R. study

The non-loaded nanocarriers were centrifuged and washed, similar to CPT loaded nanocarriers. The pellet was resuspended in acetate buffer (0.02 M, pH 4.0) and again centrifuged. The supernatant obtained was used for preparing CPT solutions of different concentrations. The emission spectra of the respective solutions were recorded and the intensities at 434 nm were noted. These intensities were plotted against CPT concentrations to have a CPT standard curve in acetate buffer. The standard curve of CPT in phosphate buffer and DMSO were made by dissolving the non-loaded nanocarrier pellet in phosphate buffer (0.02 M, pH 7.4) and DMSO respectively and then following the same procedure as above.

4.1.7 TEM and FESEM analysis of the treated HeLa cells

For TEM and FESEM analysis, the HeLa cells were seeded in a 35 mm cell culture plate and were then allowed to grow overnight. Then the serum medium was removed, washed with phosphate buffer saline (PBS) and the fresh serum medium containing CPT loaded nanocarriers was added to the cells. The cells were incubated in a humidified atmosphere containing 5 % CO_2 at 37 °C for 5 h. Then the medium was removed, washed with PBS for two times, trypsinized and centrifuged. The cell pellet obtained was resuspended in 2 % glutaraldehyde and incubated at room temperature for 3 h. The fixed cells were then dehydrated with

graded ethanol solutions and finally resuspended in absolute ethanol. Similarly the suspension of HeLa cells without treatment was also prepared. These cell suspensions were used for TEM and FESEM analysis. The cell suspension was drop-cast on a carbon-coated copper TEM grid for TEM analysis and on a glass slide (wrapped with an aluminium foil) for FESEM analysis.

4.1.8 Confocal laser scanning microscopic analysis

For confocal analysis, 200000 cells well^{-1} were seeded onto coverslips in a 6 well plate and allowed to grow overnight. Then the medium was removed, washed with PBS and fresh media containing CPT loaded nanocarriers (0.45 mg mL^{-1}), CPT (1.3 μg mL^{-1}) or non-loaded nanocarriers (0.45 mg mL^{-1}) were added to separate wells. The cells were incubated for 5 h and then following washing with PBS, the cells were counterstained with calcein AM at 37 °C for 15 min. The cells were again washed with PBS and fixed using freshly prepared 4 % paraformaldehyde solution at room temperature for 15 min. Finally the cells were washed and the cover slips were mounted on glass microscopic slide with a drop of mounting agent. The coverslips were sealed and then analysed under Leica TCS-SP8 confocal microscope. The calcein and CPT were excited by 488 nm and 404 nm lasers respectively.

4.1.9 Cell viability assay

10000 cells well^{-1} were seeded in a 96 well microplate and grown overnight. Then the medium was removed and fresh media containing varying concentrations of non-loaded nanocarriers (0.05 mg mL^{-1} – 0.45 mg mL^{-1}) or CPT loaded nanocarriers (0.05 mg mL^{-1} – 0.45 mg mL^{-1}) or CPT (0.15 μg mL^{-1} – 1.3 μg mL^{-1}) were added to the cells. After 24 h incubation, MTT based cell viability assay was carried out and the absorbance of the formed formazan in DMSO was recorded at 550 nm using a Bio-Rad 680 microplate reader.

4.2 Results and Discussion

4.2.1 Development and characterization of PLGA coated nanocarriers

The principle of synthesis of the PLGA coated nanocarriers and their delivery to human cervical cancer HeLa cells resulting into apoptosis are shown in **Scheme 4.1**. There are three steps, all of which involve non-covalent interactions between the participating entities: (i) formation of Au NP-Lyz agglomerates induced by electrostatic interaction between the negatively charged Cit-Au NPs and the positively charged Lyz (pI 10.7) at pH ~6.9 (as mentioned in Chapter 3); (ii) loading of the CPT in the agglomerates using primarily hydrophobic interactions of CPT with Lyz[122] and (iii) formation of PLGA shell surrounding the agglomerates via oil in water single emulsion process, driven by the electrostatic interaction between the positively charged Lyz (pI 10.7) of the agglomerates and the negatively charged carboxylic acid end-groups in PLGA (pK_a 3.85).[123]

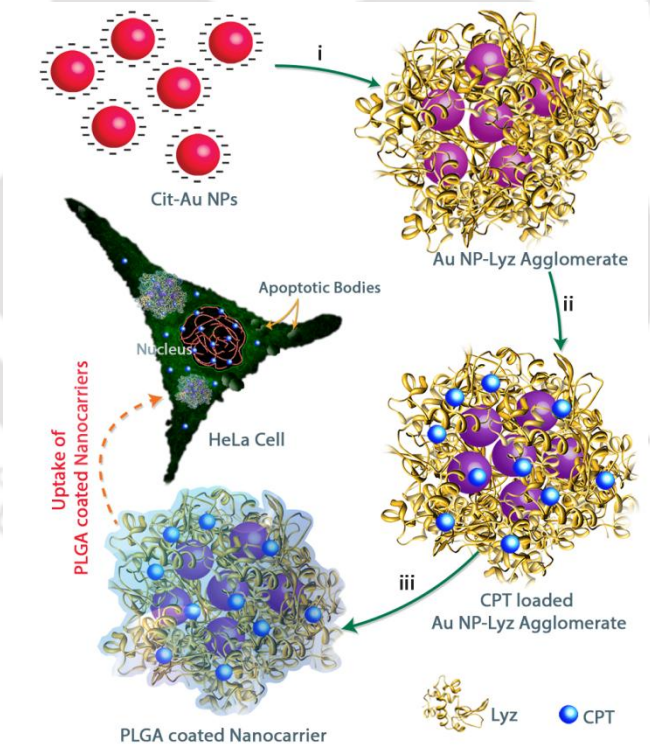

Scheme 4.1 A schematic illustration of the development of PLGA coated nanocarriers and their uptake by the HeLa cells followed by release of the blue fluorescent hydrophobic drug CPT, leading to apoptotic cell death. The key steps involved in the development of the nanocarriers are (i) the formation of Au NP-Lyz agglomerates, (ii) loading of CPT in the agglomerates and (iii) formation of PLGA shell surrounding the agglomerates.

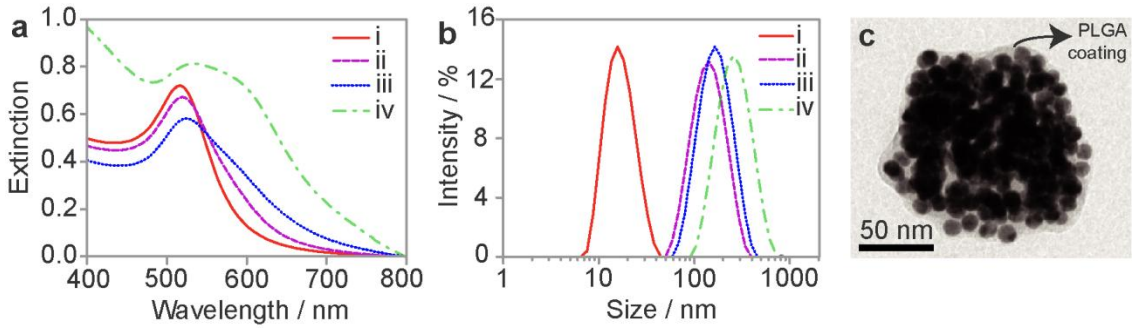

Figure 4.1 The characterization of PLGA coated nanocarriers. (a) UV-visible extinction spectra of (i) Cit-Au NPs, (ii) Cit-Au NPs + Lyz, (iii) Cit-Au NPs + Lyz + CPT and (iv) Cit-Au NPs + Lyz + CPT + PLGA. (b) Particle size distribution curves of (i) Cit-Au NPs, (ii) Cit-Au NPs + Lyz, (iii) Cit-Au NPs + Lyz + CPT and (iv) Cit-Au NPs + Lyz + CPT + PLGA as determined by DLS. (c) Representative TEM micrograph of a PLGA coated nanocarrier.

During the preparation of the nanocarriers, the change in the extinction spectrum of the Au NPs, occurring at each step, was monitored using UV-visible spectroscopy. Upon addition of 0.74 μg mL^{-1} of Lyz to Cit-Au NPs, the color of the colloidal gold changed from ruby red to pinkish purple, accompanied by broadening of the peak and shifting of extinction maximum (λ_{max}) from 516 nm to 519 nm (**Figure 4.1 a**). These indicated the formation of Au NP-Lyz agglomerates. When 1.2 μg mL^{-1} of CPT was added to these agglomerates and incubated for 1 h in the dark, the color changed to bluish purple and the extinction spectrum further broadened and the peak shifted to 524 nm (**Figure 4.1 a**), suggesting additional agglomeration. Emulsification of these CPT loaded agglomerates (in water) with PLGA (in DCM), followed by evaporation of the organic solvent and then centrifugation resulted in the formation of PLGA coated nanocarriers having a broad extinction spectrum with λ_{max} at 533 nm (**Figure 4.1 a**). Further, dynamic light scattering (DLS)-based particle size analysis indicated that addition of Lyz to Cit-Au NPs significantly shifted the particle size distribution with the Z_{avg} from 17.4 ± 0.3 nm to 109.6 ± 2.6 nm, indicating the formation of larger particles in the dispersion (**Figure 4.1 b**). Addition of CPT further shifted the distribution curve and the Z_{avg} was found to be 151.2 ± 3.2 nm (**Figure 4.1 b**), representing formation of even larger particles. Importantly, PLGA coating resulted in additional shifting of the particle size distribution curve with Z_{avg} of 215.5 ± 3.8 nm (**Figure 4.1 b**). Literature report suggests that the size of the coated

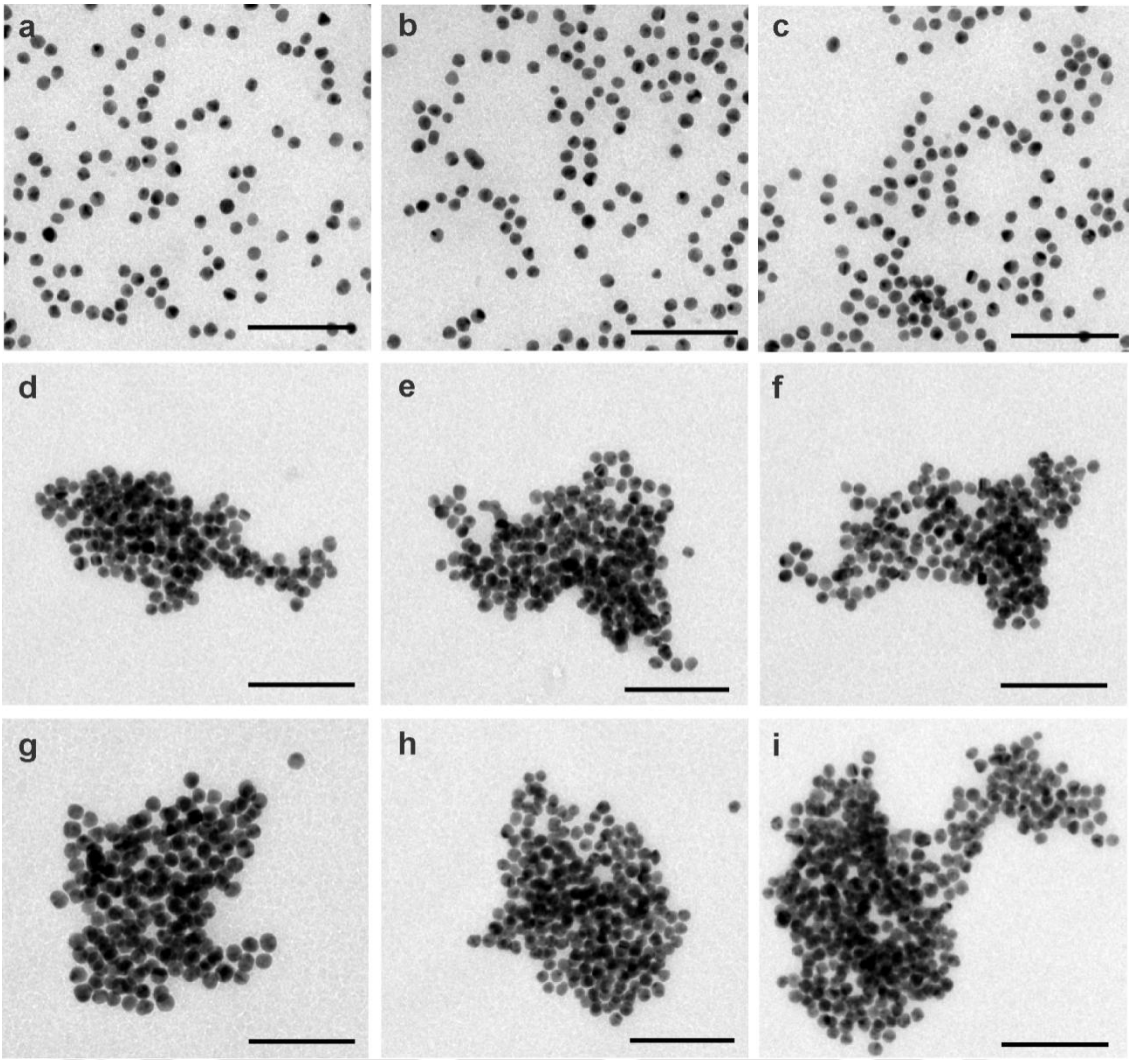

Figure 4.2 TEM micrographs of (a-c) Cit-Au NPs, (d-f) Au NP-Lyz agglomerates and (g-i) CPT loaded Au NP-Lyz agglomerates. Scale bar is 100 nm.

nanocarriers would allow their extravasation through the leaky vessels of the tumor vasculature.[1, 115] TEM micrograph of the PLGA coated nanocarrier (**Figure 4.1 c**) evidenced the presence of organic coating surrounding a large number of assembled Au NPs; the appearance of these particles are distinctly different from Cit-Au NPs (**Figure 4.2 a-c**), Au NP-Lyz agglomerates (**Figure 4.2 d-f**) or CTP loaded Au NP-Lyz agglomerates (**Figure 4.2 g-i**). The average particle size of these PLGA coated nanocarriers, calculated from a few TEM images, was found to be 157 ± 15 nm. This is close to the measured value obtained from DLS-based particle size measurement. The difference could be due to evaporation induced shrinkage of the nanocarriers. The zeta potential of the nanocarriers at 25 °C in water was found to be -53.55 ± 1.66 mV, which prevented the nanocarriers from flocculating.[124] Overall, the process led to the generation of stable nanocarriers

consisting of polymer coated agglomerates of Au NP and Lyz with incorporation of CPT. That the average size of the carriers conforms to the requirements for extravasation through leaky vesicles improves their chance of practical usage.

4.2.2 Stability of the PLGA coated nanocarriers in human blood serum and against proteases

For the application of the nanocarriers (especially the protein based) in vivo, they ought to be stable in human blood serum[18] and be resistant to degradation by protease enzymes in the presystemic circulation.[20, 21] Their stability in human blood serum was tested by adding the PLGA coated nanocarriers in serum (being kept at 37 °C) and recording the extinction spectrum of the medium at different time intervals, which was pursued for 48 h. **Figure 4.3 a** shows the extinction spectra of the serum, nanocarriers in water and nanocarriers after being added to the serum. A closer analysis revealed that the extinction spectrum of nanocarriers

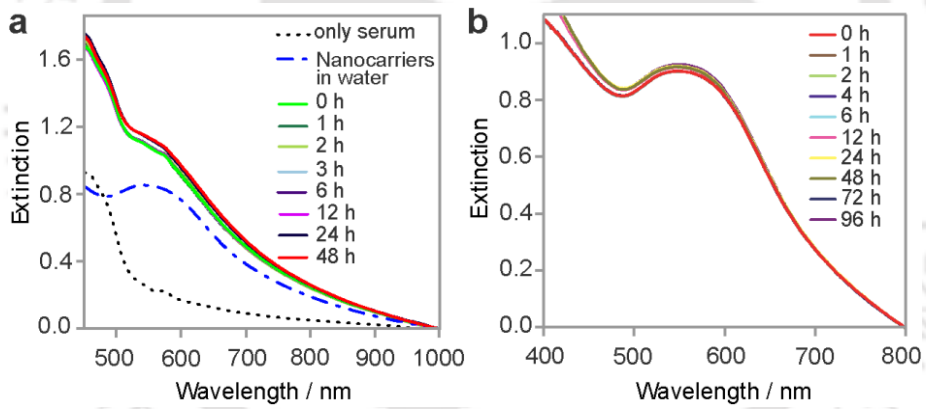

Figure 4.3 Evidences for the stability of PLGA coated nanocarriers in human blood serum and in water. UV-visible extinction spectra of PLGA coated nanocarriers (a) in human blood serum and (b) in water at different intervals of time as mentioned in the legends.

in serum is a simple summation of the extinction due to the nanocarriers and the serum, indicating that presence of serum did not lead to significant changes in the nanocarriers. Moreover, there was no change in the extinction spectrum of the nanocarriers in serum with time indicating that no further agglomeration, disruption or precipitation occurred. This ensured the stability of the nanocarriers in human blood serum, which could possibly enable their in vivo applications. Furthermore, the stability of the nanocarriers was tested similarly in water, where they also proved to be stable (**Figure 4.3 b).** The stability of the nanocarriers in

human blood serum and in water might be due to the presence of PLGA coating surrounding the agglomerates.

In order to investigate the stability of the carriers – especially the Lyz protein – against enzymatic digestion, the PLGA coated nanocarriers were incubated with a broad spectrum serine protease, Proteinase K, for 1 h at 37 °C, which was analyzed using sodium dodecyl sulphate polyacrylamide gel electrophoresis (SDS-PAGE) and TEM. The SDS-PAGE analysis depicted that Lyz treated with the protease (250 ng) was degraded nearly completely, as is shown in Lane 3 of **Figure 4.4 a**. On the other hand, as are evident in Lane 5 and Lane 6 (**Figure 4.4 a**), distinct bands due to Lyz present in the PLGA coated carrier appeared, even following treatment with 250 ng and 500 ng of protease, respectively. The results indicated stability of the protein in the PLGA coated nanocarrier even in the presence of protease. The appearance of lower molecular weight bands in both Lane 5 and Lane 6 was

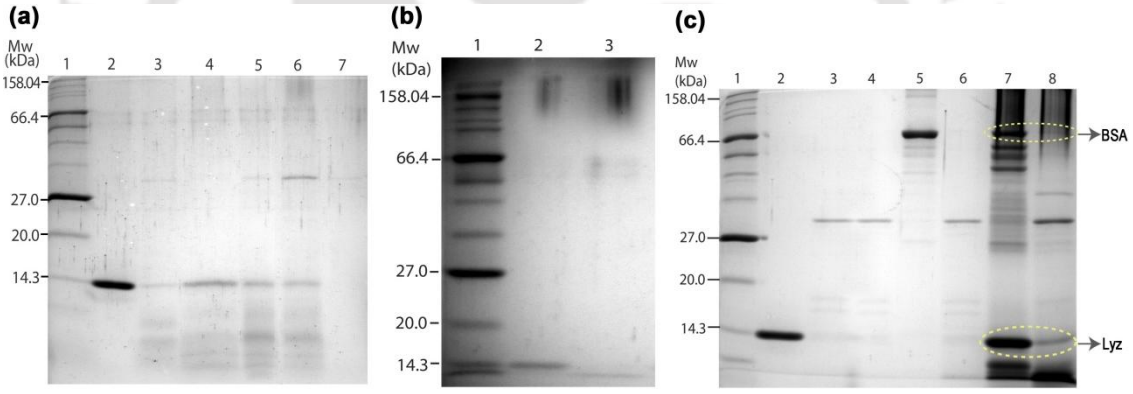

Figure 4.4 (a) SDS-PAGE analysis of PLGA coated nanocarriers with and without protease treatment. The lanes correspond to 1: New England Biolabs Protein marker; 2: Lyz without protease treatment; 3: Lyz with protease treatment; 4: PLGA coated nanocarriers without protease treatment; 5: PLGA coated nanocarriers with 250 ng protease treatment; 6: PLGA coated nanocarriers with 500 ng protease treatment and 7: Proteinase K. (b) SDS-PAGE analysis of Au NP-Lyz agglomerates with and without protease treatment. Lane 1: New England Biolabs Protein marker; 2: Au NP-Lyz agglomerates without protease treatment and 3: Au NP-Lyz agglomerates with protease treatment. (c) SDS-PAGE analysis of albumin coated nanocarriers with and without protease treatment. Lane 1: New England Biolabs Protein marker; 2: Lyz without protease treatment; 3: Lyz with protease treatment; 4: Proteinase K; 5: albumin without protease treatment; 6: albumin with protease treatment; 7: albumin coated nanocarriers without protease treatment and 8: albumin coated nanocarriers with protease treatment. The molecular weights of the proteins in the marker are reported on the left of each image for reference.

possibly due to the degradation of Lyz that remained adhered to the outer surface of the PLGA shell during fabrication of the nanocarriers. It is to be mentioned here that the 28.9 kDa band in Lanes 3, 5, 6 and 7 is due to Proteinase K. Importantly, in order to probe the stability due to PLGA coating, the SDS-PAGE analysis was carried out with Au NP-Lyz agglomerates. Lyz in agglomerates, without polymer shell, was completely degraded after protease treatment (Lane 3; **Figure 4.4 b**). Further, in albumin coated nanocarriers (mentioned in Chapter 3, **Figure 4.4 c**), both the proteins – albumin and Lyz – were found to have been either completely or nearly completely degraded after protease treatment (Lane 8; **Figure 4.4 c**).

The above results were also supported by the TEM analysis, which indicated that the agglomerated structures along with polymer coating were intact in case of PLGA coated nanocarriers (**Figure 4.5**), whereas, in albumin coated nanocarriers (**Figure 4.6 a-c**), the albumin layer as well as the agglomerated structures were disrupted following protease treatment (**Figure 4.6 d-f**). In other words, when the agglomerates were coated with albumin, the nanocarriers were susceptible to protease degradation. On the other hand, when the agglomerates were coated with PLGA instead they were stable in the presence of proteases.

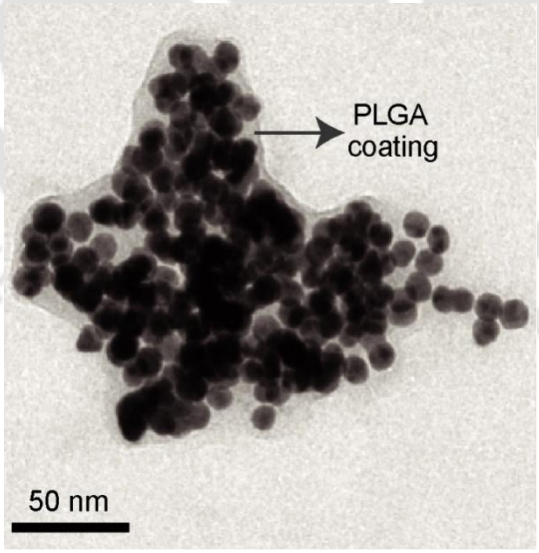

Figure 4.5 TEM micrograph of PLGA coated nanocarrier after protease treatment.

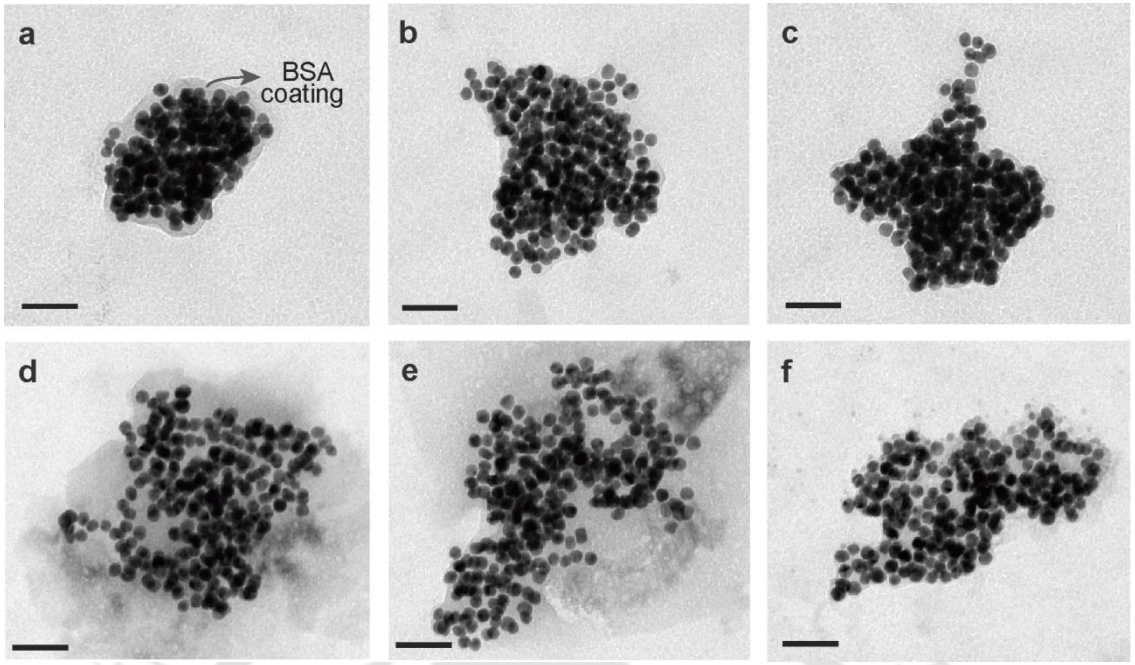

Figure 4.6 TEM micrographs of albumin coated nanocarriers (a-c) without and (d-f) with protease treatment. Scale bar is 50 nm.

4.2.3 Encapsulation efficiency and in vitro release of CPT from loaded PLGA coated nanocarriers

The encapsulation efficiency (E.E.) of the nanocarriers for CPT was calculated using a fluorescence spectroscopic technique and it was found to be 38.6 %, when 0.04 mL of 0.5 mg mL^{-1} CPT was added to NP-protein agglomerates. The agglomerates were formed from 15 mL of Cit-Au NPs, with a maximum extinction 0.72 at 516 nm (**Figure 4.1 a**) and 1.2 mL of 0.01 mg mL^{-1} Lyz. This means, when 20 μg of CPT was present in the dispersion containing 15 mL of Au NPs and 12 μg of Lyz, 7.72 μg of CPT was encapsulated due to hydrophobic interaction of CPT with the tryptophan residue of Lyz.[122] CPT was chosen particularly for encapsulation because its free form is unstable – the active lactone form gets hydrolyzed to inactive carboxylate form, which binds irreversibly with human serum albumin at physiological pH.[17] Therefore, the delivery of the drug CPT can be possible by encapsulating the drug in a suitable nanocarrier. The in vitro cumulative release (C.R.) of CPT from the PLGA coated nanocarriers was also studied for 24 h and it was about ~5 % in acetate buffer (pH 4.0), ~7 % in phosphate buffer (pH 7.4) and ~12 % in DMSO (data not shown). The relatively

higher release of CPT in DMSO could be due to its greater solubility in the non-polar solvent.

4.2.4 Uptake of PLGA coated nanocarriers by cancer cells

An important criterion for the success of nanocarriers is the ease of their internalization by the cancer cells. The in vitro internalization study was pursued by incubating the HeLa cells with PLGA coated nanocarriers for 5 h, followed by analysis using TEM and confocal microscopy. **Figure 4.7 a** represents the TEM micrograph of a HeLa cell treated with PLGA coated nanocarriers and **Figure 4.7 b** is the magnified image of a part of the cell, marked with red dotted circle. **Figure 4.7 b** demonstrates the internalization of a significant number of nanocarriers by the single cell. Selected area electron diffraction (SAED) pattern of the darker spots represented (110) and (200) planes of fcc Au NP crystals, thus confirming the presence of Au NPs in the cell. The details of nanocarrier internalization by the cell at various positions are shown in **Figure 4.8 a-f**.

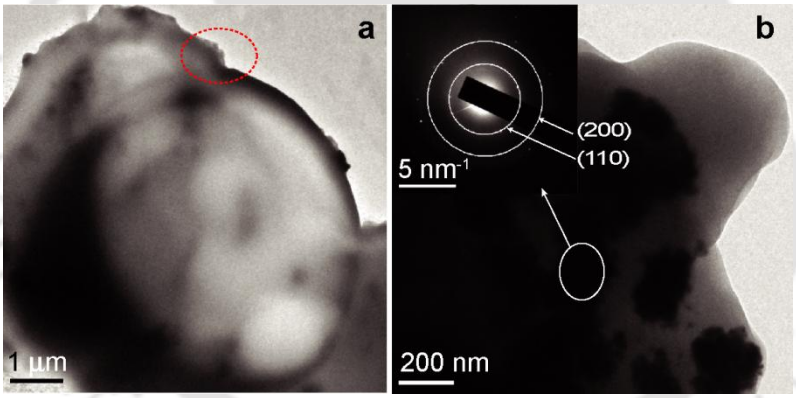

Figure 4.7 Evidence for the uptake of PLGA coated nanocarriers by the HeLa cells. (a) TEM micrograph of the HeLa cell treated with PLGA coated nanocarriers for 5 h and (b) High magnification image of a region of the HeLa cell (marked with red dotted circle) having the nanocarriers internalized, inset: SAED from the internalized nanocarriers.

The internalization of the CPT loaded nanocarriers by the HeLa cells was also confirmed by the confocal microscopic analysis. In order to have clearer view of the cells, the cytoplasm was counterstained with calcein AM after treatment with CPT loaded nanocarriers for 5 h. Calcein AM is the acetomethoxy derivative of calcein which can readily enter the cell membrane and gets converted to green fluorescent calcein by intracellular esterases.[125] **Figure 4.9 a-d** demonstrated the

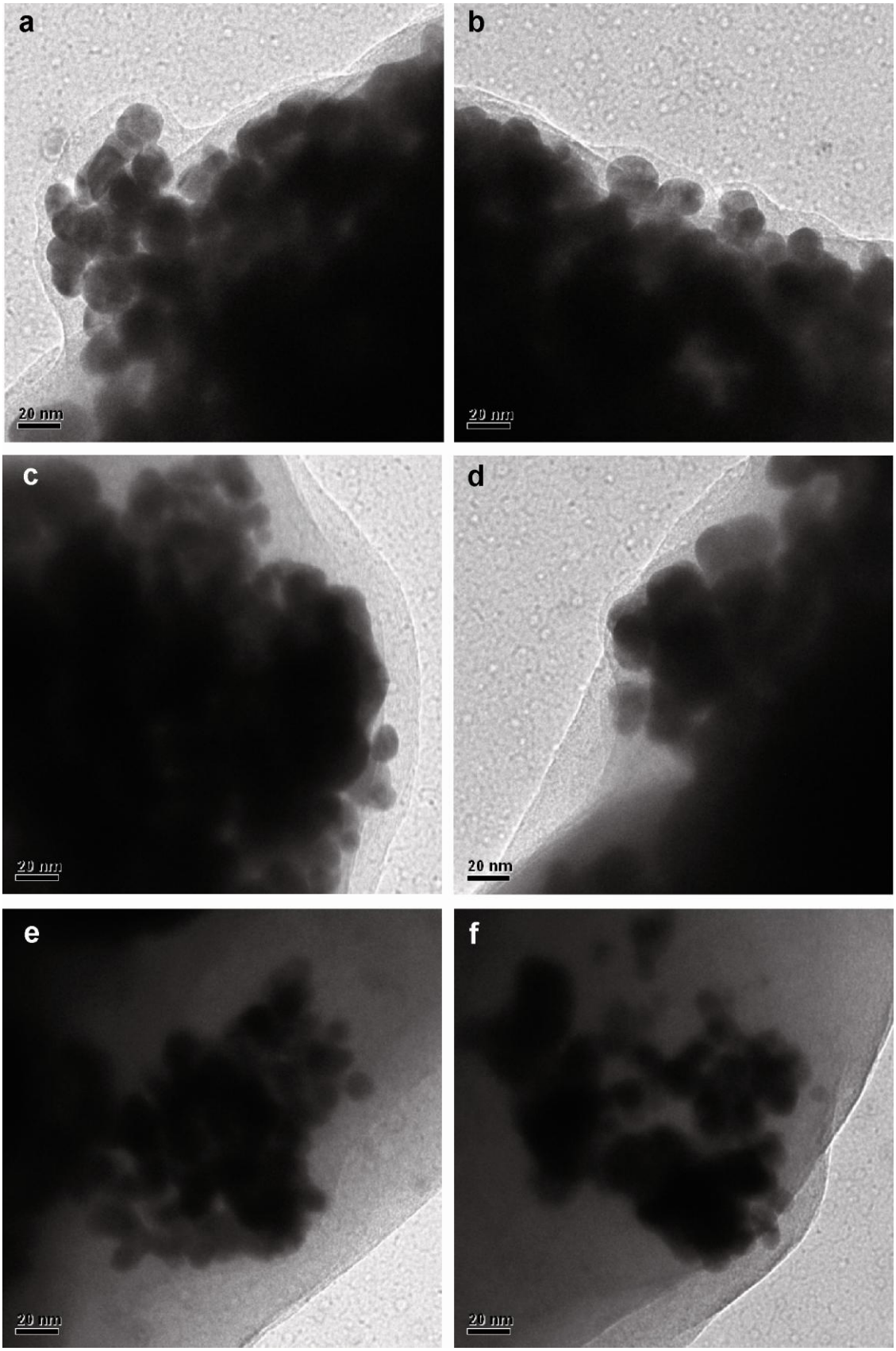

Figure 4.8 TEM micrographs of the various regions of the HeLa cell having the PLGA coated nanocarriers internalized. Scale bar is 20 nm.

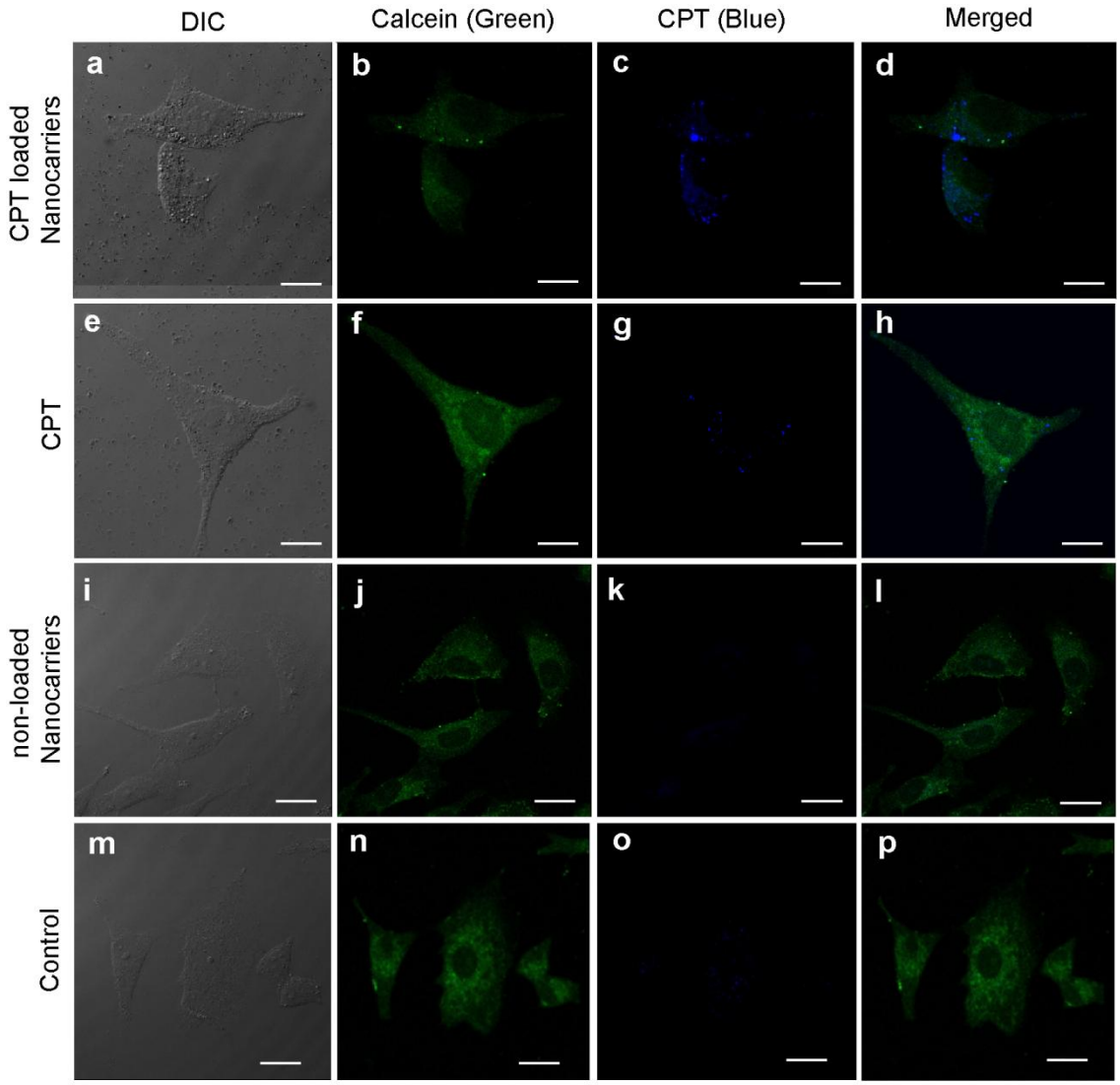

Figure 4.9 Representative confocal laser scanning microscopic images of HeLa cells treated with (a-d) CPT loaded nanocarriers, (e-h) CPT only and (i-l) non-loaded nanocarriers for 5 h. (m-p) Representative confocal laser scanning microscopic images of control HeLa cells. The cytoplasm was counterstained with calcein AM (Scale bar: 20 μm, Magnification: 60× oil immersion objective).

presence of blue fluorescence – corresponding to CPT – at various positions inside the cell. This, similar to TEM analysis, also indicated the internalization of several nanocarriers by the single cell after 5 h. The observed blue fluorescence (**Figure 4.9 c and d**) – for the CPT loaded nanocarrier treated HeLa cell – could be either due to CPT loaded in the nanocarriers or CPT released from the nanocarriers inside the cell or both. However, it is difficult to quantitatively measure the amount of CPT released after 5 h treatment inside the cells. Blue fluorescence was also observed for HeLa cells treated with CPT only (**Figure 4.9 e-h**). However, no

such blue fluorescence could be observed for non-loaded nanocarriers treated (**Figure 4.9 i-l**) and control HeLa cells (**Figure 4.9 m-p**). Thus, although the PLGA coated nanocarriers are negatively charged, they are efficiently internalized by the cancerous cells.[126, 127] This internalization of negatively charged nanocarriers could be either due to facultative diffusion or via endocytotic processes.[128]

4.2.5 Consequence of the drug release from the loaded PLGA coated nanocarriers

The real test for successful delivery of CPT using nanocarriers is in their release within the cell, which would eventually lead to the drug-induced accumulation of topoisomerase I-DNA complexes, causing apoptotic cell death.[129] In order to confirm this, the HeLa cells were incubated with various concentrations of CPT loaded nanocarriers for 24 h and MTT based in vitro cell viability assay was performed on those cells. The results, as shown in **Figure 4.10 a**, demonstrated that CPT loaded nanocarriers killed the HeLa cells efficiently. With increase in the concentration of CPT loaded nanocarriers from 0.05 mg mL^{-1} (containing 0.15 μg mL^{-1} of CPT) to 0.45 mg mL^{-1} (containing 1.3 μg mL^{-1} of CPT), the cell viability decreased consistently from 77 % to 46 %. In order to ensure that the cytotoxic effect was for CPT and not for nanocarriers themselves, cell viability assay, by

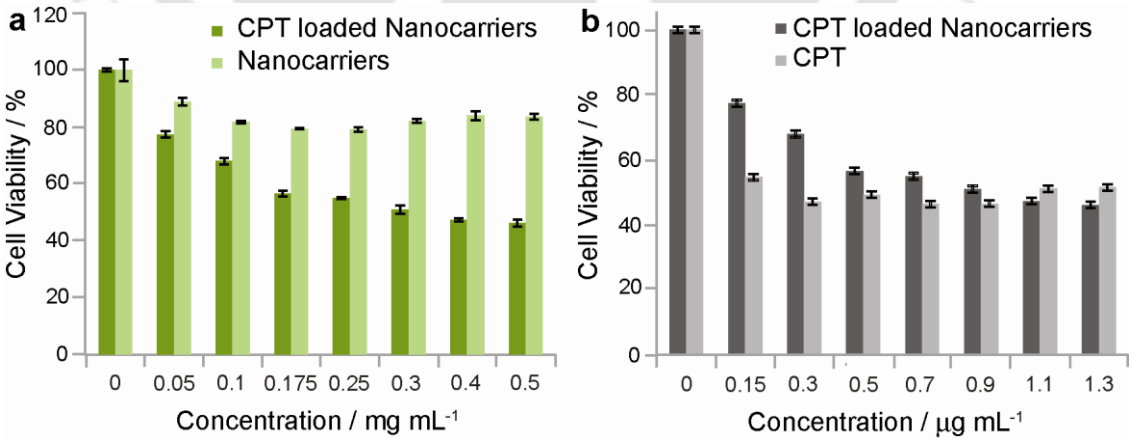

Figure 4.10 MTT based cell viability assay of HeLa cells after 24 h treatment with (a) CPT loaded nanocarriers or non-loaded nanocarriers at varying nanocarrier concentration and (b) CPT loaded nanocarriers or CPT only at varying CPT concentrations. Data are represented as mean ± S.D. of three individual experiments.

incubating the HeLa cells with non-loaded nanocarriers was also performed. The results (**Figure 4.10 a**) indicated that the nanocarriers themselves were not significantly toxic to the cells. Further, the half maximal inhibitory concentration (IC_{50}) value for CPT loaded in the nanocarriers was found and compared with that of free CPT. For CPT loaded in the nanocarriers it was found to be ~0.9 μg mL^{-1} (CPT concentration), which was higher than that of free CPT (~0.3 μg mL^{-1}) (**Figure 4.10 b**). This could be due to incomplete release of CPT from the nanocarriers during the investigation period.[130]

Another evidence for the programmed cell death is the formation of apoptotic bodies. The field emission scanning electron microscopy (FESEM) image of the CPT loaded nanocarriers treated HeLa cell showed the presence of such apoptotic bodies (**Figure 4.11 a**), thus confirming the binding of CPT with DNA, leading to programmed cell death. As a control, the FESEM image of the untreated HeLa cell is shown in **Figure 4.11 b**, which evidenced the absence of apoptotic body. Thus, from MTT based cell viability assay and FESEM analysis, it is clear that CPT must have been released inside the cells and interacted with DNA, resulting in programmed cell death. The complete mechanism of intracellular drug release is beyond the reach of the current experiments; however, it could be due to the degradation of PLGA coating either by hydrolysis or by intracellular esterases,[45] which resulted in the diffusion/release of CPT from the Au NP-Lyz agglomerates.

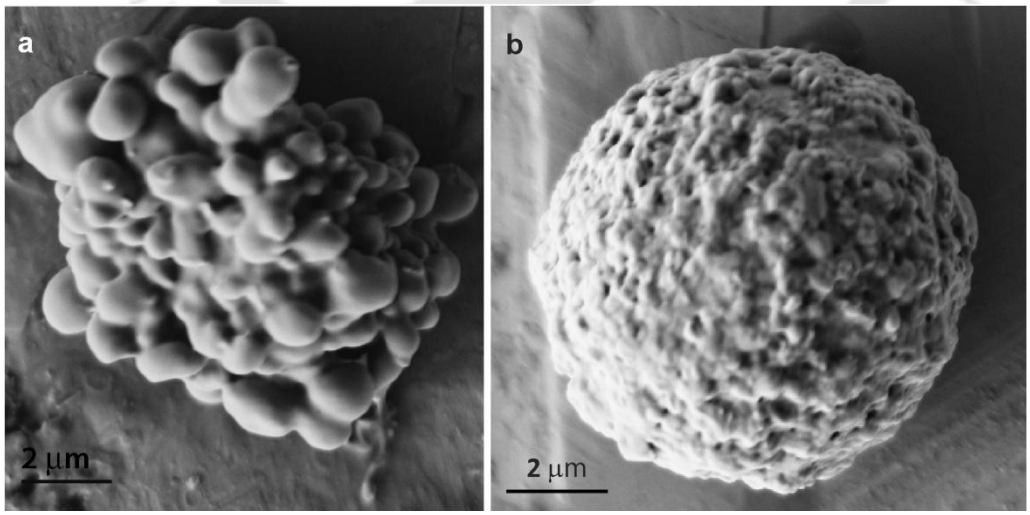

Figure 4.11 FESEM images of (a) CPT loaded nanocarriers treated (for 5 h) HeLa cell and (b) untreated HeLa cell.

4.3 Conclusions

In summary, we have been able to fabricate a highly stable nanocarrier based on non-covalent interactions between Au NPs, protein and finally PLGA. The nanocarriers were biocompatible; they could be loaded with the hydrophobic drug CPT and delivered to cancer cells, whereupon apoptotic cell death occurred following the release of the molecule. Importantly, the nanocarriers were resistant against protease degradation; they were stable in human blood serum and are of sizes suitable for cancer tissue passive targeting based on the EPR effect. Their ease of formation, ability for encapsulation of hydrophobic drug and facile release of the potent molecules in cancer cells make the nanocarriers an ideal choice for practical drug delivery especially for cancer treatment. Moreover, incorporation of the targeting ligands like monoclonal antibody, arginine-glycine-aspartate (RGD) peptide on the PLGA coating would enhance the efficacy through active targeting of cancer tissues.[131, 132]

CHAPTER 5

Gold Nanocluster embedded Albumin Nanoparticles for Two-photon Imaging of Cancer Cells accompanying Drug Delivery

As chapters 3 and 4 were based on the fabrication of nanocarriers for only drug delivery application, this chapter reports the fabrication of biocompatible gold nanocluster embedded albumin nanoparticles for both diagnosis and therapy i.e theranostic. The gold nanoclusters embedded in albumin nanoparticles were non-toxic, highly photostable and have the capability to be imaged both by one- and two- photon excitations with the two-photon excitation/emission lying in the biological window of 650-900 nm. The composite nanoparticles loaded the anticancer drug doxorubicin with high efficiency and were then used to deliver to cancer cells, leading to apoptotic cell death. The drug loaded composite nanoparticles retained their luminescence in human blood serum and met the size criterion for possible passive targeting of cancer cells, through the enhanced permeation and retention (EPR) effect. The luminescent nanoparticles may serve as model platforms for nanotheranostics.

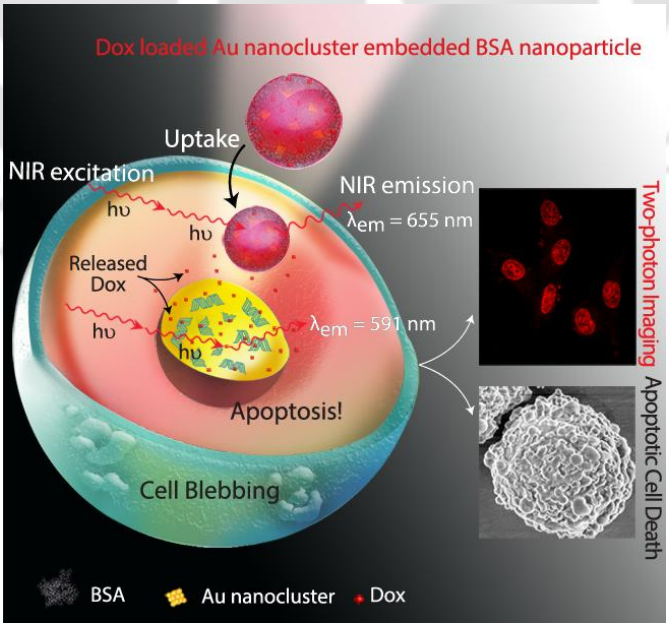

* **Submitted to Small (Wiley-VCH)**

5.1 Experimental Section

5.1.1 Materials

Hydrogen tetrachloroaurate trihydrate ($HAuCl_4.3H2O$, Sigma-Aidrich Co., USA), bovine serum albumin (BSA, Sisco Research Laboratories Pvt. Ltd., India), sodium hydroxide (NaOH, Merck, India), acetone (Merck, India), doxorubicin hydrochloride (Dox, Parental Drugs Ltd., India), 3-(4,5-dimethylthiazol-2-yl)-2,5-diphenyltetrazolium bromide (MTT, Himedia, India), quinine sulfate (Fluka, USA) and rhodamine 6G (Sigma-Aldrich Co., Germany) were purchased and used as received without any further purification. Milli-Q ultrapure water (>18 MΩ cm, Millipore) was used in all the experiments.

5.1.2 Synthesis of BSA-stabilized Au nanoclusters

BSA-stabilized Au nanoclusters were prepared following a method reported by Xie et al.[133] Briefly, aqueous $HAuCl_4$ solution (5 mL of 10 mM) was added to aqueous BSA solution (5 mL of 50 mg mL^{-1}) and stirred vigorously for 2 min at 37 °C. After this, NaOH solution (1.1 mL, 1 M) was added to adjust the pH of the reaction mixture to 12.0. The above solution was allowed to stir vigorously for 12 h at 37 °C, resulting in the formation of deep brown solution, which is characteristic of BSA-stabilized Au nanocluster formation.[133]

5.1.3 Synthesis of Au nanocluster embedded BSA nanoparticles

The Au nanocluster embedded BSA nanoparticles were prepared by modifying the known methods for the preparation of BSA nanoparticles.[134, 135] Typically, the as-synthesized BSA-stabilized Au nanoclusters (3.3 mL) were diluted (to 10 mL) with water and the pH was adjusted to 8.8. To the above stirring (750 rpm) solution at 30 °C, acetone was added (using the peristaltic pump) drop by drop at a rate of 1 mL min^{-1} until the solution became just turbid. The turbidity indicated the formation of nanoparticles. After this, the temperature was raised to 50 °C and the dispersion was stirred (at 750 rpm) continuously for 12 h to stabilize the nanoparticles. Then, the organic solvent acetone was removed using a rota-vapor and finally the nanoparticles were centrifuged twice at 25000 rcf, for 20 mins and 4 °C to remove the untreated BSA-stabilized Au nanoclusters. The pellet so

obtained was redispersed in water (4.2 mL) and used for further experiments. The pH of the Au nanocluster embedded BSA nanoparticle dispersion was measured to be ~8.2.

5.1.4 Characterization of BSA-stabilized Au nanoclusters and Au nanocluster embedded BSA nanoparticles

The BSA-stabilized Au nanoclusters and Au nanocluster embedded BSA nanoparticles were characterized using UV-visible spectrophotometer (Perkin Elmer, Lambda 750), HORIBA Jobin Yvon FluoroMax-4 spectrofluorimeter and TEM (JEOL JEM 2100, maximum accelerating voltage 200 kV). Quantum yields of the samples were measured using rhodamine 6G (in ethanol) as the reference. Photostability experiments were performed, using rhodamine 6G as the standard, in a Perkin Elmer LS 55 instrument for 1800 sec (with 0.1 sec data interval). The solid powder of the BSA-stabilized Au nanoclusters and Au nanocluster embedded BSA nanoparticles were obtained after lyophilization (using Christ Alpha 1-4 LD lyophilizer) of their respective aqueous dispersions. As a control, the pH of the as-synthesized BSA-stabilized Au nanocluster solution was adjusted ~8.2 (similar to the dispersion of Au nanocluster embedded BSA nanoparticles).

5.1.5 Loading of Dox in Au nanocluster embedded BSA nanoparticles and calculating the encapsulation efficiency (E.E.)

To the above dispersion of Au nanocluster embedded BSA nanoparticles (1 mL), an aqueous solution of Dox (2 mL of 16.39 μg mL^{-1} - actual content of Dox in the as-prepared solution) was added and stirred (750 rpm) for 2 h at 30 °C in the dark. After this, the Dox loaded Au nanocluster embedded BSA nanoparticles were led through three cycles of centrifugation (25000 rcf, 20 mins and 4 °C), washing with water and redispersion to remove the unloaded Dox. Finally, the pellet obtained was redispersed in water.

For calculating the E.E., the supernatants obtained from all the washing cycles were mixed together and its emission (λ_{ex} = 480) spectrum was recorded using the spectrofluorimeter. The emission intensity at 591 nm was noted and the concentration of Dox in the supernatant was calculated using the standard curve (intensity vs concentration) of Dox. The E.E. was measured in triplicates.

Then the E.E. was calculated using the formula

$$E.E.\ \% = \frac{Dox_i - Dox_s}{Dox_i} X100 \qquad (5.1)$$

where, $[Dox]_i$ is the concentration of Dox initially added and $[Dox]_s$ is the concentration of Dox in the supernatant. The E.E. for Pyr was also calculated in the same way.

Generation of standard curve of Dox for E.E. study

As the emission intensity of Dox is a function of the pH of the medium and the supernatant may contain several moieties which can effect the emission intensity of Dox,[112] the standard curve of Dox was obtained by dissolving different concentrations of Dox in the supernatant, obtained after washing of Au nanocluster embedded BSA nanoparticles (non-loaded) only (similar to Dox loaded Au nanocluster embedded BSA nanoparticles). The emission (λ_{ex} = 480) spectra of all the Dox containing solutions were recorded using the spectrofluorimeter and the emission intensities at 591 nm were noted. Using these emission intensities and the respective Dox concentrations, a standard curve for E.E was obtained.

5.1.6 Characterization of Dox loaded Au nanocluster embedded BSA nanoparticles

The particle size and the zeta potential were measured using a DLS-based particle size analyzer (Zetasizer Nano ZS90, Model No. ZEN3690, Malvern). The emission spectrum was recorded using a HORIBA Jobin Yvon FluoroMax-4 spectrofluorimeter. In addition to DLS-based particle size analysis, the size characterization was also done using TEM, FESEM and AFM. For TEM, dispersion of Dox loaded Au nanocluster embedded BSA nanoparticles was drop-casted on carbon-coated copper TEM grid and left overnight for drying. This was then analyzed under a JEOL JEM 2100 transmission electron microscope, operating at a maximum accelerating voltage of 200 kV. For FESEM, 10 μL of the dispersion was deposited on a glass slide (which was wrapped with an aluminium foil), dried and then coated with a gold film (using SC7620 “Mini”, Polaron Sputter Coater, Quorum Technologies, Newhaven, England). The sample was analyzed under

ΣIGMA, Carl Zeiss field emission scanning electron microscope. For AFM, the dispersion of Dox loaded Au nanocluster embedded BSA nanoparticles was spin coated (2000 rpm) onto a glass slide and dried at 50 °C for 2 h and then the sample was analyzed under Agilent (Model 5500-SPM) atomic force microscopy.

5.1.7 Stability of the luminescence intensity of Dox loaded Au nanocluster embedded BSA nanoparticles in human blood serum

The concentrated dispersion of Dox loaded Au nanocluster embedded BSA nanoparticles were diluted with human blood serum and its emission spectra with two different excitations (365 and 505 nm) were recorded immediately. After this, the nanoparticle dispersion in human blood serum was incubated at 37 °C and at regular time intervals, its emission spectra were recorded. As a control, similarly, the emission spectra of the human blood serum only were also recorded at excitations 365 and 505 nm.

5.1.8 Confocal laser scanning microscopic analyses

For confocal analyses, 150000 HeLa cells well^{-1} were seeded onto coverslips placed inside 6 well plate and allowed to grow overnight. Then the medium was removed and fresh medium containing Au nanocluster embedded BSA nanoparticles (0.62 mg mL^{-1}), Dox loaded Au nanocluster embedded BSA nanoparticles (0.62 mg mL^{-1} of the loaded composite, which effectively meant 7.8 μg mL^{-1} of Dox was present in the medium) or Dox (7.8 μg mL^{-1}) were added to the cells and incubated for 4 h in a humidified atmosphere containing 5 % CO_2 at 37 °C. After this, the cells were washed twice with PBS and were fixed with freshly prepared 4 % formaldehyde solution for 15 min at room temperature. The cells were washed again and finally mounted on a glass microscopic slide with a drop of mounting agent. The cover slips were sealed and then the samples were visualized under Leica TCS SP8 STED (using 405 nm diode laser and 515 nm multiline argon laser) and TCS SP5 Multi-Photon (using multi-photon laser and white light laser, WLL) confocal microscope.

5.1.9 Cell viability assay

For cell viability assay, HeLa cells (8500 cells well^{-1}) were seeded in a 96 well

microplate and grown overnight. Then the medium was removed and fresh medium containing varying concentrations of Au nanocluster embedded BSA nanoparticles (0.16 - 1.1 mg mL^{-1}) or Dox loaded Au nanocluster embedded BSA nanoparticles (0.16 - 1.1 mg mL^{-1}) or Dox (0.28 - 1.94 μg mL^{-1}) were added to the cells. After 36 h incubation, MTT based cell viability assay was carried out and the absorbance of the formed formazan in DMSO was recorded at 550 nm, using a Bio-Rad 680 microplate reader. For each of the samples, the assay was carried out in triplicates.

5.1.10 FESEM analyses of the untreated and treated HeLa cells

For FESEM analyses, the HeLa cells were seeded in a 35 mm cell culture plate and were then allowed to grow overnight. Then the medium was removed and fresh medium containing Dox loaded Au nanocluster embedded BSA nanoparticles (0.62 mg mL^{-1}) was added to the cells. After 4 h incubation, the cells were washed twice with PBS and then trypsinized. The trypsinized cells were centrifuged and redispersed in 2 % glutaraldehyde solution for fixation. Following 3 h of incubation at room temperature, the cells were washed with graded ethanol solutions and finally resuspended in absolute ethanol. Similarly the suspension of HeLa cells without treatment was also prepared. The cell suspension of both treated and untreated cells were deposited on separate glass slides (which were wrapped with aluminium foils) and then were observed under FESEM.

5.2 Results and Discussion

5.2.1 Generation and characterization of Au nanocluster embedded BSA nanoparticles

The nanocluster embedded BSA nanoparticles were prepared by first synthesizing Au nanoclusters in BSA using an established procedure.[133] This was followed by the preparation of BSA nanoparticles using a modified procedure based on the preparation of only albumin nanoparticle.[134, 135] This was necessary as it was observed that the established procedure for the generation of stable albumin nanoparticle led to loss of luminescence of the nanoclusters. The use of chemical reagents like glyoxal and glutaraldehyde[136] or the high temperature[137] was

avoided for cross linking the protein during stabilization as this led to quenching of the luminescence of the nanoclusters. Briefly, BSA-stabilized Au nanoclusters were treated with acetone - at an addition rate of 1 mL min^{-1} at 30 °C - till turbidity was observed in the medium. This was followed by stirring the mixture at 50 °C for 12 h. The medium was centrifuged and the pellet so obtained was redispersed in water, which was then used for further experiments. The detailed procedure is described in the Experimental Section.

The clear brown dispersion of BSA-stabilized Au nanoclusters (**Figure 5.1 a i**) turned turbid brown following formation of composite nanoparticles (**Figure 5.1 a iii**). On the other hand, excitation by UV light (365 nm) led to intense red coloration of both the as-synthesized BSA-stabilized Au nanoclusters and the nanoparticles, in liquid dispersions (**Figure 5.1 a v and vii**) as well as in solid powder forms (**Figure 5.1 a vi and viii**). Importantly, the extinction (with no prominent bands;[133, 138] **Figure 5.1 b**) and excitation (with a broad band centered at 505 nm, in addition to a shoulder at 365 nm;[139] **Figure 5.1 c**) spectra remained unaltered following formation of nanoparticles. However, there was a blue shift of the emission maximum by 4 nm (i.e. from 659 nm to 655 nm), at both the 365 nm (**Figure 5.1 d**) and 505 nm (**Figure 5.1 e**) excitations. The quantum yield (**Table 5A.1,** *Appendix*) of the clusters embedded in BSA nanoparticles was found to have been reduced in comparison to those of as-synthesized BSA-stabilized Au nanoclusters. For example, the quantum yield (QY) of the as-prepared Au nanoclusters embedded in BSA nanoparticle was found to be 1.9 % at pH 8.2 (which is quite suitable for bio-imaging),[83] while as-prepared BSA-stabilized Au nanoclusters showed the yield of 5.8 % at pH 12.0[133] (**Table 5A.1,** *Appendix*). Additionally, when the pH of the as-synthesized BSA-stabilized nanoclusters was adjusted to ~pH 8.2 (similar to aqueous dispersion of the nanoparticles), similar 4 nm blue shift in the emission spectra was observed (**Figure 5A.1 a and b,** *Appendix*);[137] while no significant change was observed in the excitation spectrum

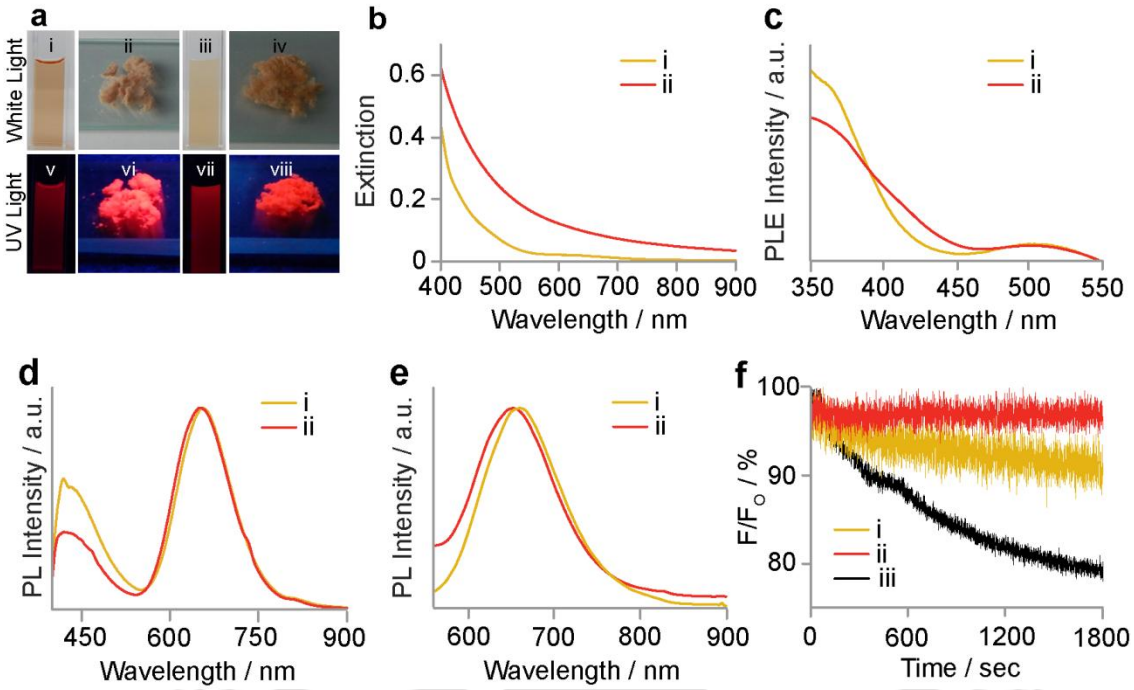

Figure 5.1 Retention of optical properties of Au nanocluster in the composite nanoparticles. (a) Digital photographs of (i, v) aqueous dispersion and (ii, vi) solid powder of BSA-stabilized Au nanoclusters, (iii, vii) aqueous dispersion and (iv, viii) solid powder of Au nanocluster embedded BSA nanoparticles in presence of white light and UV light (365 nm). (b) Extinction spectra of (i) BSA-stabilized Au nanoclusters and (ii) Au nanocluster embedded BSA nanoparticles. (c) Excitation spectra of (i) BSA-stabilized Au nanoclusters (λ_{em} = 659 nm) and (ii) Au nanocluster embedded BSA nanoparticles (λ_{em} = 655 nm). (d) Emission (λ_{ex} = 365 nm) spectra of (i) BSA-stabilized Au nanoclusters and (ii) Au nanocluster embedded BSA nanoparticles. (e) Emission (λ_{ex} = 505 nm) spectra of (i) BSA-stabilized Au nanoclusters and (ii) Au nanocluster embedded BSA nanoparticles. (f) Photostability of (i) BSA-stabilized Au nanoclusters (λ_{em} = 659 nm), (ii) Au nanocluster embedded BSA nanoparticles (λ_{em} = 655 nm) and (iii) Rhodamine 6G (λ_{em} = 560 nm) monitored with λ_{ex} = 505 nm.

of the pH adjusted BSA-stabilized Au nanoclusters (**Figure 5A.1 c,** *Appendix*). This clearly indicates that the emission behavior of BSA-stabilized Au clusters is pH dependent[137] and also supports that the observed blue shift in emission maxima and decreased QY were primarily due to change in pH of the aqueous dispersion of BSA-stabilized Au nanoclusters as well as that of the composite nanoparticles. The photostability of the Au nanoclusters in the composite nanoparticles was found to be comparable to that of BSA-stabilized clusters and the values were five and three times higher than that of an organic dye (rhodamine 6G) at 365 nm (**Figure 5A.2,** *Appendix*) and 505 nm (**Figure 5.1 f**) excitations (**Table 5A.2,** *Appendix*)

respectively. The Stokes shifts of the emissions, due to Au clusters embedded in BSA nanoparticles, were also found to be large i.e 290 nm (at λ_{ex} = 365 nm) and 150 nm (at λ_{ex} = 505 nm). Finally, it can be stated that the Au nanoclusters were successfully embedded in BSA nanoparticles, without significant loss of their photoluminescence properties and these nanoparticles were endowed with all the characteristics for use in real applications i.e. in vivo imaging.

5.2.2 Encapsulation of Dox by Au nanocluster embedded BSA nanoparticles

The efficiency of the Au nanocluster embedded BSA nanoparticles to encapsulate the therapeutic drug Dox was investigated, using the fluorescence spectroscopic technique and it was found to be 83.05 %. Thus, when 32.78 μg of Dox was added to as-prepared 1 mL of the nanoparticle dispersion, 27.22 μg of the drug was encapsulated. The emission spectrum of the Dox loaded Au nanocluster embedded BSA nanoparticles evidenced an additional peak at ~591 nm, when excitation was fixed at 505 nm (**Figure 5.2**). This peak at ~591 nm is the characteristic of Dox (**Figure 5.2**). The encapsulation of Dox was further confirmed by measuring the zeta potential of the Dox loaded composite nanoparticles. The zeta potential of the Au clusters embedded BSA nanoparticles changed from −39.6 ± 0.9 mV to −26.1 ±

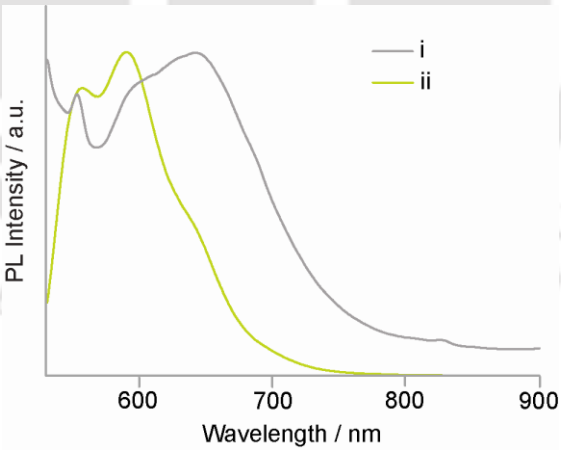

Figure 5.2 Emission (λ_{ex} = 505 nm) spectra of (a) Dox loaded Au nanocluster embedded BSA nanoparticles and (b) Dox only.

0.2 mV after loading of Dox. This reduction in zeta potential may be due to electrostatic interaction of positively charged Dox (pk_a 8.4) with the negatively charged composite nanoparticles.[54] However, the interactions of Dox with the

hydrophilic and hydrophobic sites of BSA cannot be ruled out.[140] Thus, the excellent luminescent properties of the Au nanocluster embedded in BSA nanoparticles as well as the high efficiency of them to encapsulate the therapeutic drug molecules made them suitable for nanotheranostics.

5.2.3 Luminescence stability of Dox loaded Au nanocluster embedded BSA nanoparticles in human blood serum

Ideally, in order to monitor the pharmacokinetics of these Dox loaded composite nanoparticles in vivo, their photoluminescence must be present at least in the blood serum. For this, the emission spectra of the nanoparticles redispersed in human blood serum were recorded at regular intervals of time (upto 24 h) and it was observed that there were no significant changes, thus confirming their stability (**Figure 5.3 a and b**).

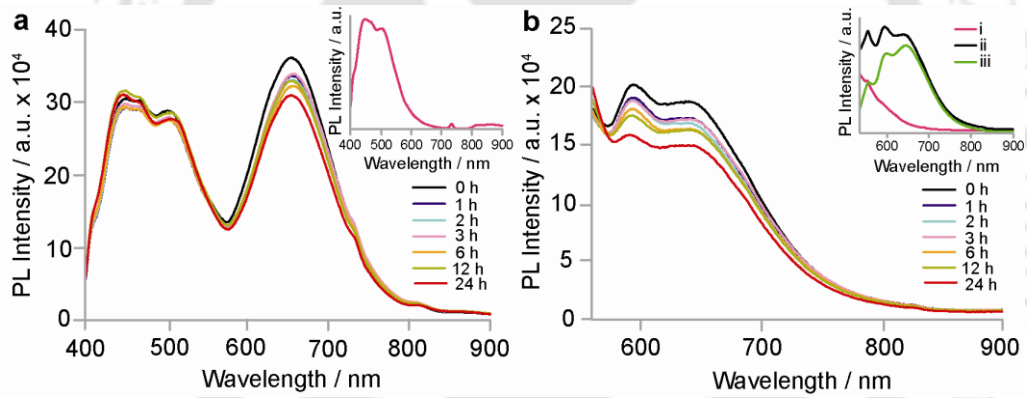

Figure 5.3 Evidences for the luminescence stability of Dox loaded Au nanocluster embedded BSA nanoparticles in human blood serum. (a) Emission (λ_{ex} = 365 nm) spectra of Dox loaded Au nanocluster embedded BSA nanoparticles in human blood serum at different intervals of time as mentioned in the legends. Inset: Emission (λ_{ex} = 365 nm) spectrum of human blood serum only. (b) Emission (λ_{ex} = 505 nm) spectra of Dox loaded Au nanocluster embedded BSA nanoparticles in human blood serum at different intervals of time as mentioned in the legends. Inset: Emission (λ_{ex} = 505 nm) spectra of (i) human blood serum only and (ii) Dox loaded Au nanocluster embedded BSA nanoparticles (in human blood serum). (iii) Emission spectrum as plotted following subtraction of emission intenties of human blood serum only from the emission intensities of Dox loaded Au nanocluster embedded BSA nanoparticles (in human blood serum). As the emission spectrum iii (inset of Figure 5.3 b) matches with that of emission spectrum i (in Figure 5.2), it indicates that the serum components did not led to any significant change in the emission spectrum of Dox loaded Au nanocluster embedded BSA nanoparticles.

5.2.4 Size suitability of Dox loaded Au nanocluster embedded BSA nanoparticles for enhanced permeation and retention (EPR) effect

The size suitability of these nanoparticles for possible application through passive targeting of tumor cells via the EPR effect was examined. For this, the Dox loaded composite nanoparticles were characterized using transmission electron microscopy (TEM), field emission scanning electron microscopy (FESEM), atomic force microscopy (AFM) and dynamic light scattering (DLS)-based particle size analysis. From TEM (**Figure 5.4 a**) and FESEM (**Figure 5.4 b**), the average particle size was found to be 112 ± 20 nm and 112 ± 14 nm respectively, whereas from AFM (**Figure 5.4 c**) it was calculated to be 200 ± 33 nm. DLS-based particle size analysis showed a single narrow particle size distribution curve (**Figure 5.4 d**) with average hydrodynamic diameter (Z_{avg}) of 186 ± 2 nm and polydispersity index (PDI) of 0.06 ± 0.01. The relatively higher sizes observed in AFM and DLS measurements could be due to the presence of water surrounding the particle, which was absent in the vacuum environment of electron microscopic measurements. Overall, it can be mentioned that the nanoparticles meet the size criterion for extravasation through the leaky vessels of the tumor vasculature.[2,33] TEM (**Figure 5.4 a**), FESEM (**Figure 5.4 b**) and AFM (**Figure 5.4 c**) micrographs

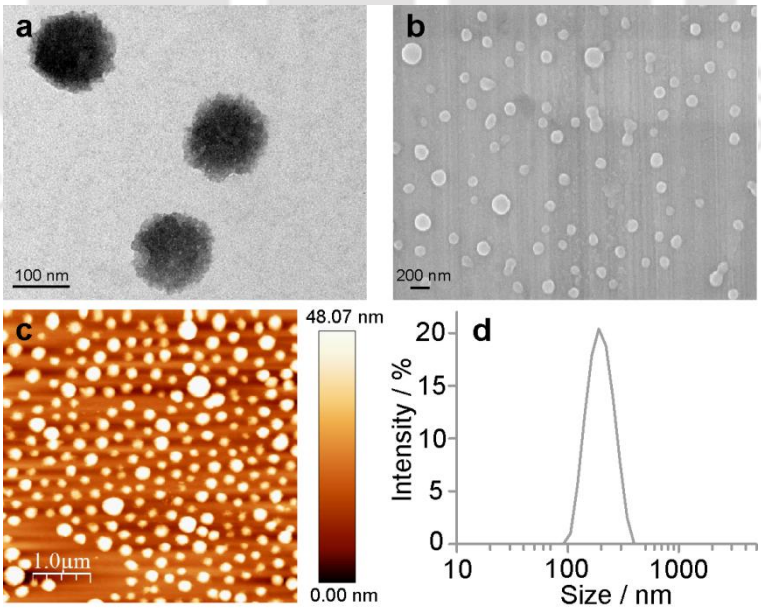

Figure 5.4 (a) TEM image, (b) FESEM image, (c) AFM image and (d) DLS-based particle size distribution curve of Dox loaded Au nanocluster embedded BSA nanoparticles showing the size suitability for passive targeting of tumor cells through the EPR effect.

also indicated that the nanoparticles were nearly spherical and homogeneous in sizes and they remained non-agglomerated even under different sample preparation conditions. Additionally, the TEM micrographs (**Figure 5.5 a and b**) indicated the presence of nanoclusters in the composite nanoparticles. The TEM micrographs of as-synthesized BSA-stabilized Au nanoclusters are shown in **Figure 5.6 a and b**, which indicated the presence of small particles.

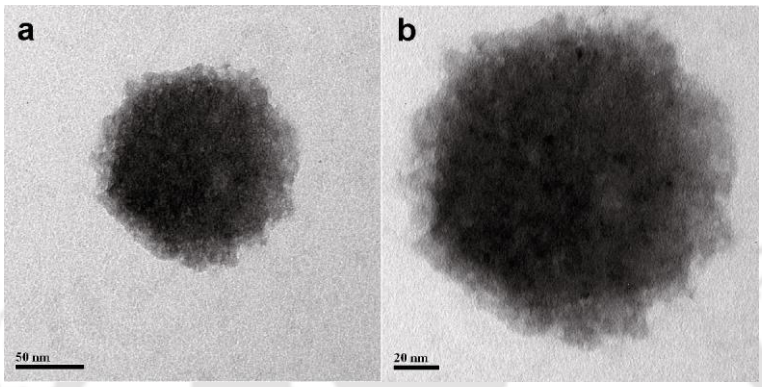

Figure 5.5 (a, b) Magnified TEM images of Dox loaded Au nanocluster embedded BSA nanoparticle showing the presence of nanoclusters in BSA nanoparticle.

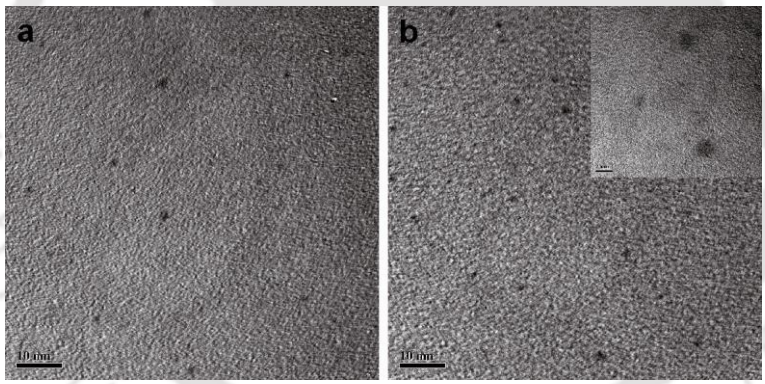

Figure 5.6 (a, b) TEM images of as-synthesized BSA-stabilized Au nanoclusters, scale bar: 10 nm (Inset: Magnified TEM image at scale bar: 2 nm).

5.2.5 Uptake and intracelleular release of Dox from loaded nanoparticles

As the sizes of the nanoparticles were found to be suitable for the delivery through EPR effect, our next aim was to study their internalization and then release of the drug molecules inside the cancer cells. This was pursued by incubating the cervical cancer HeLa cells with Dox loaded composite nanoparticles for 4 h and then analyzing under confocal microscope by one-photon excitation (using 405 nm diode laser, 515 nm multiline argon laser and white light laser – WLL with 505

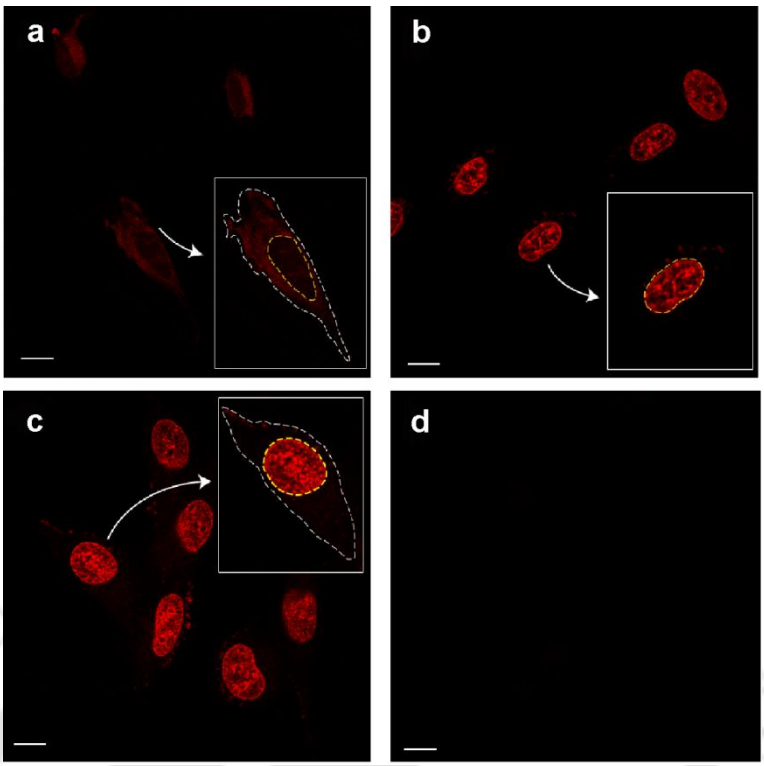

Figure 5.7 CLSM images of HeLa cells after incubation with (a) Au nanocluster embedded BSA nanoparticles, (b) Dox only and (c) Dox loaded Au nanocluster embedded BSA nanoparticles for 4 h at 37 °C. (d) CLSM image of control HeLa cells. (Scale bar: 20 μm, Excitation source: white light laser with 505 nm excitation wavelength, Magnification: 60x oil immersion objective). The insets show the high magnification images of the cells as indicated by white arrows. The periphery with yellow serrated lines represents the nuclear membrane and that with the white serrated lines represent the cell membrane.

nm excitation wavelength) as well as by two-photon excitation (using a multi-photon laser with 730 nm excitation wavelength). For the HeLa cells separately treated with Au nanocluster embedded BSA nanoparticles and Dox only, weak red luminescence predominantly in the cytoplasm (**Figure 5.7 a and Figure 5.8 a**) and bright red luminescence primarily in the nucleus (**Figure 5.7 b and Figure 5.8 b**), respectively, were observed when excited by one-photon WLL 505 nm and two-photon 730 nm lasers. The faint red luminescence is due to the Au nanoclusters embedded in BSA nanoparticles and the bright red luminescence corresponds to Dox. However, both weaker (in the cytoplasm) and brighter red luminescence (mainly in the nucleus) were observed for the HeLa cells incubated with Dox loaded composite nanoparticles, under 505 nm (**Figure 5.7 c**) or 730 nm (**Figure 5.8 c**) illumination. This indicated that the loaded nanoparticles have

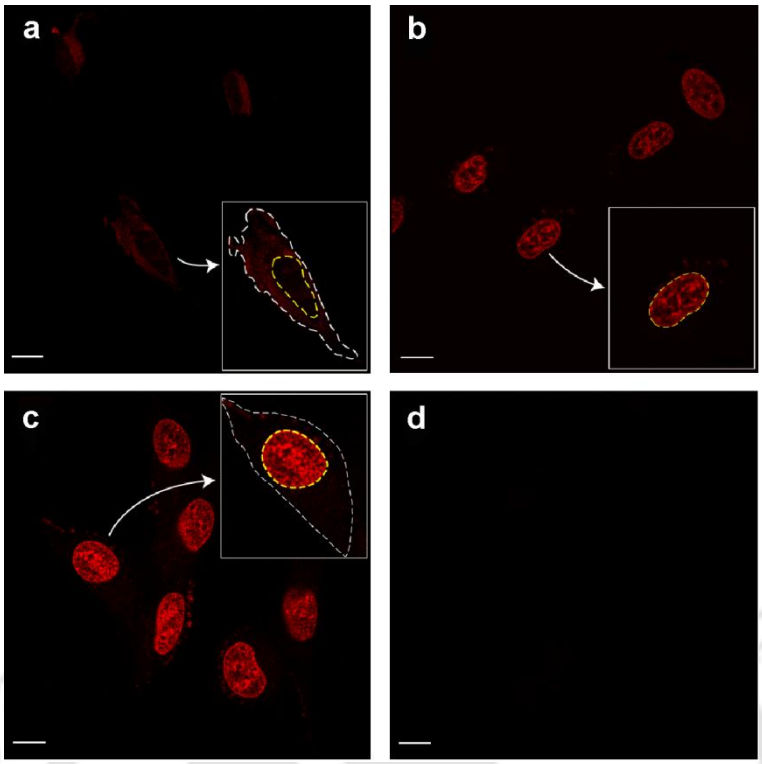

Figure 5.8 Two-photon fluorescence images of HeLa cells after incubation with (a) Au nanocluster embedded BSA nanoparticles, (b) Dox only and (c) Dox loaded Au nanocluster embedded BSA nanoparticles for 4 h at 37 °C. (d) CLSM image of control HeLa cells. (Scale bar: 20 μm, Excitation source: multi-photon laser with 730 nm excitation wavelength, Magnification: 60x oil immersion objective). The insets show the high magnification images of the cells as indicated by white arrows. The periphery with yellow serrated lines represents the nuclear membrane and that with the white serrated lines represent the cell membrane.

entered the cytoplasm of the cells giving weak red luminescence and releasing Dox, which later entered the nucleus and led to bright red emission. In untreated HeLa cells, no red luminescence was observed (**Figure 5.7 d and Figure 5.8 d**). Thus, the red luminescence emerging out of the nanoclusters embedded in BSA nanoparticles helped in studying the internalization of the nanoparticles by the cancer cells and the intrinsic red luminescence of Dox helped in studying the release of the drug molecules from the nanoparticles inside the cells. Similar observations were made when the treated and untreated control cells were imaged by exciting with 405 nm (**Figure 5.9**) and 515 nm (**Figure 5.10**) lasers. Thus, it can be concluded that the Au nanoclusters embedded in the protein nanoparticles are ideal candidates for imaging of cancer cells by both one- and

two- photon excitations and with the two-photon excitation/emission wavelengths lying in the 650-900 nm window.

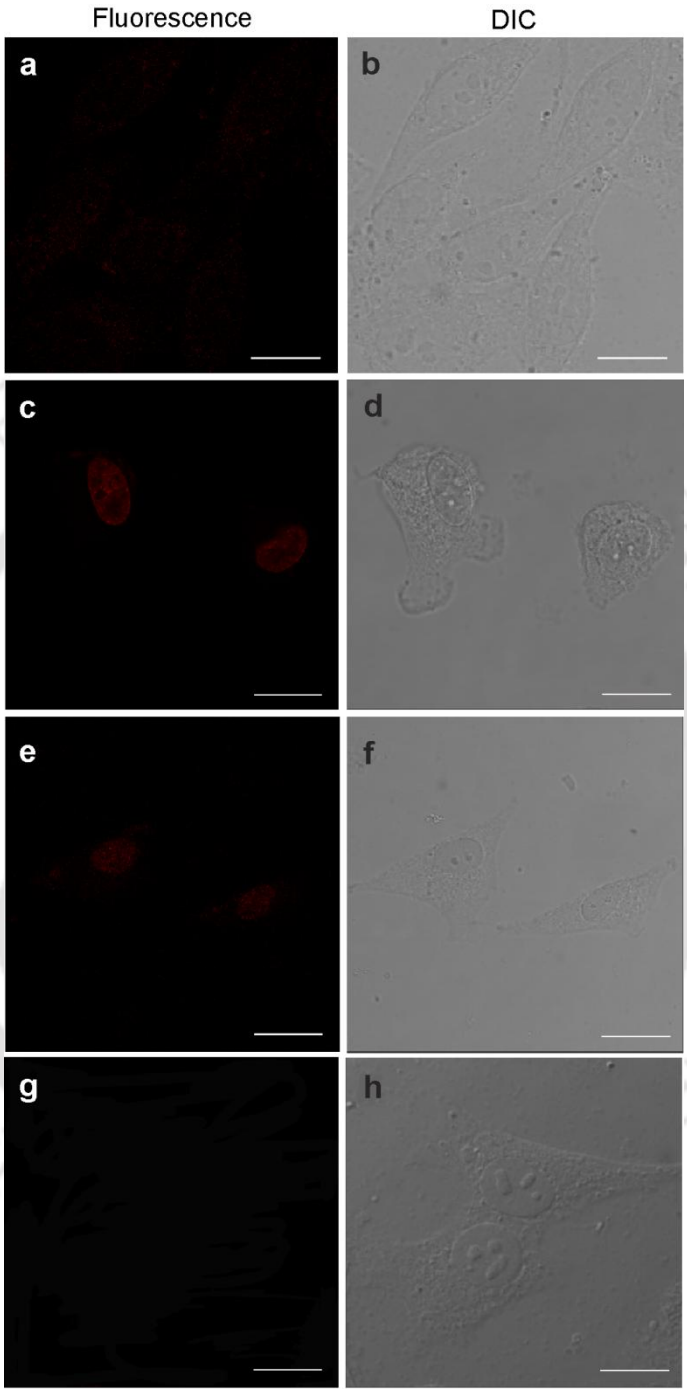

Figure 5.9 CLSM images of HeLa cells after incubation with (a, b) Au nanocluster embedded BSA nanoparticles, (c, d) Dox only and (e, f) Dox loaded Au nanocluster embedded BSA nanoparticles for 4 h at 37 °C. (g, h) CLSM images of control HeLa cells. (Scale bar: 20 μm, Excitation source: diode laser with 405 nm excitation wavelength, Magnification: 60x with oil immersion objective).

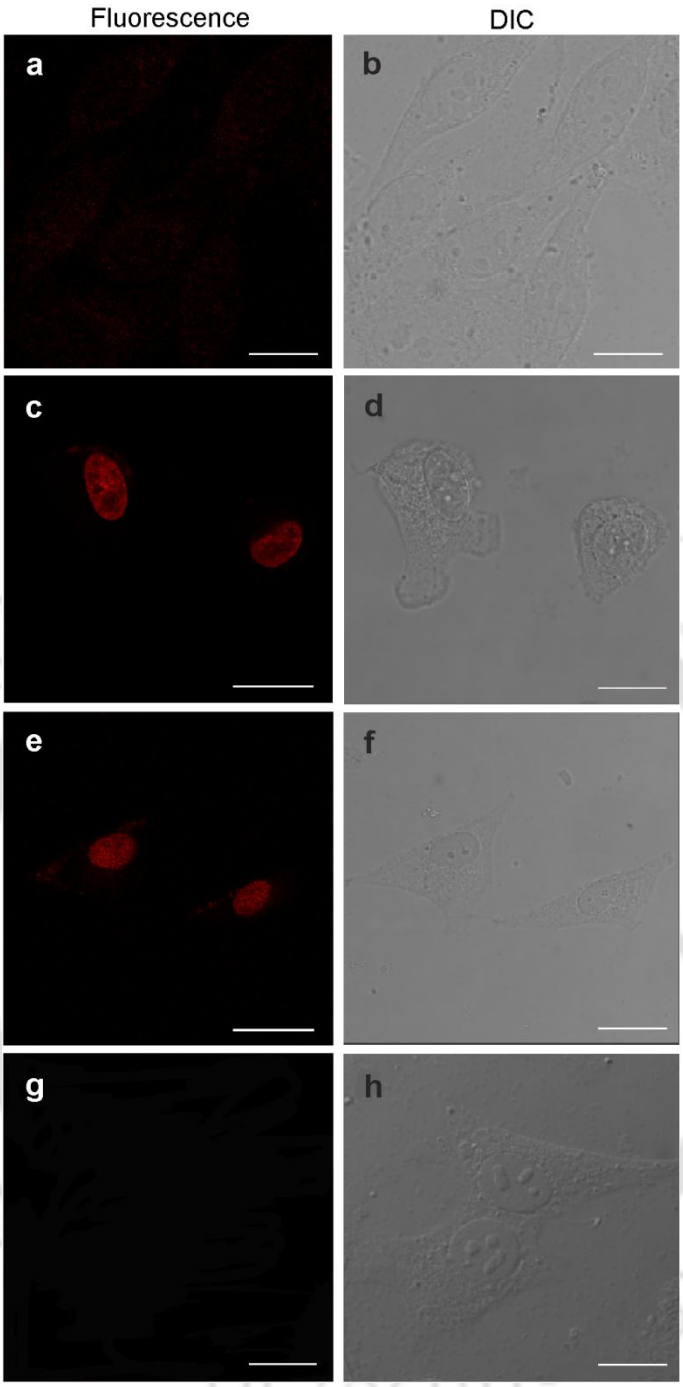

Figure 5.10 CLSM images of HeLa cells after incubation with (a, b) Au nanocluster embedded BSA nanoparticles, (c, d) Dox only and (e, f) Dox loaded Au nanocluster embedded BSA nanoparticles for 4 h at 37 °C. (g, h) CLSM images of control HeLa cells. (Scale bar: 20 μm; Excitation source: multiline argon laser with 515 nm excitation wavelength; Magnification: 60x with oil immersion objective).

3.2.6 Consequence of the drug release from the Dox loaded nanoparticles

In order to probe the cytotoxicity – if any – of the Au nanocluster embedded BSA nanoparticles, MTT based in vitro cell viability assay was carried out by incubating the HeLa cells with the nanoparticles for 36 h. For all the concentrations used, more than 90 % of the cells were viable (**Figure 5.11 a**). Thus the nanoparticles

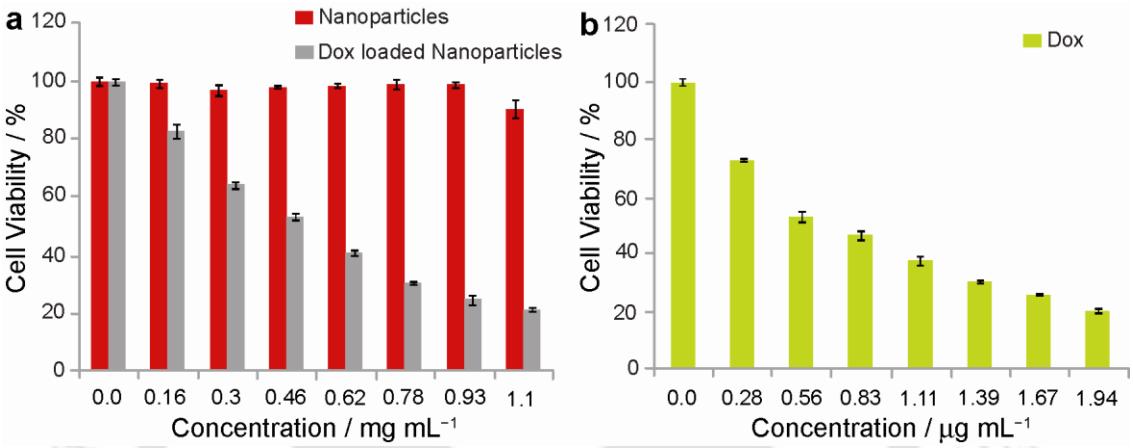

Figure 5.11 MTT based cell viability assay of HeLa cells after 36 h treatment with (a) Au nanocluster embedded BSA nanoparticles (non-loaded) and Dox loaded Au nanocluster embedded BSA nanoparticles at varying concentrations of the nanoparticles and (b) Dox only at varying Dox concentrations. Data are represented as mean ± S.D. of three individual experiments.

themselves were non-toxic to the cells and hence qualify for use in bio-imaging. However, when these nanoparticles were loaded with Dox, they killed the cancer cells efficiently (**Figure 5.11 a**). However, the measured IC_{50} value of 0.47 mg mL^{-1} Dox loaded nanoparticles, which is equivalent to 6.3 µg mL^{-1} of Dox, is greater than that of free Dox (IC_{50} 0.82 µg mL^{-1}; **Figure 5.11 b**). The difference could be due to incomplete release of Dox from the nanoparticles during the investigation period.[130] Further, the nanoparticle formulation has many advantages over free drug; for example, it reduces the side effects through passive targeting of the cancer cells as well as prevents the drug from degradation and prematurely interacting with biological moieties.[1] Additionally, in order to probe the ability of the luminescent nanoparticle containing Dox to cause programmed cell death (apoptosis),[121] FESEM analysis of a HeLa cell incubated with the same for 4 h was carried out. This evidenced the presence of apoptotic bodies on the surface of treated HeLa cell (**Figure 5.12 a**), which was absent in a control HeLa

cell (**Figure 5.12 b**). Thus, the luminescent nanoparticle not only helped in probing the delivery but also released the drug leading to apoptotic cell death. A schematic description in **Scheme 5.1**, of the use of Au nanocluster embedded and Dox loaded BSA nanoparticle for in vitro drug delivery and observing its effect on human cervical cancer HeLa cells, captures the essence of the work.

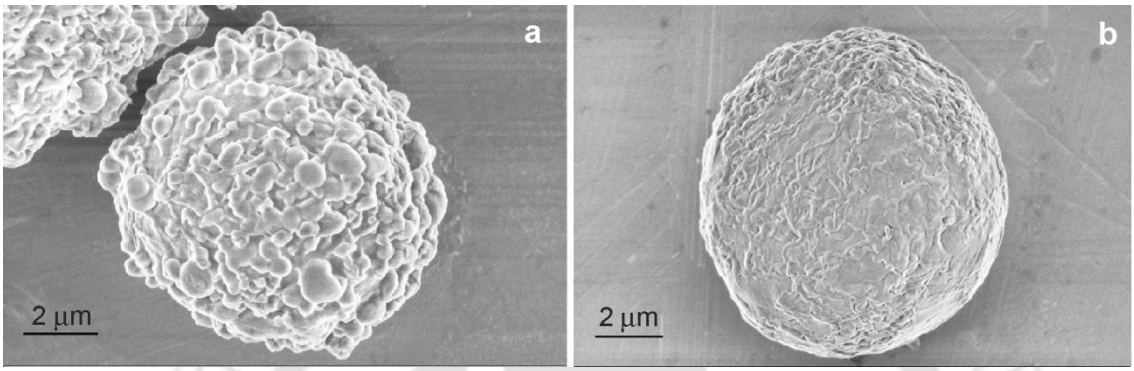

Figure 5.12 FESEM images of (a) Dox loaded Au nanocluster embedded BSA nanoparticles treated (for 4 h) HeLa cell and (b) untreated HeLa cell.

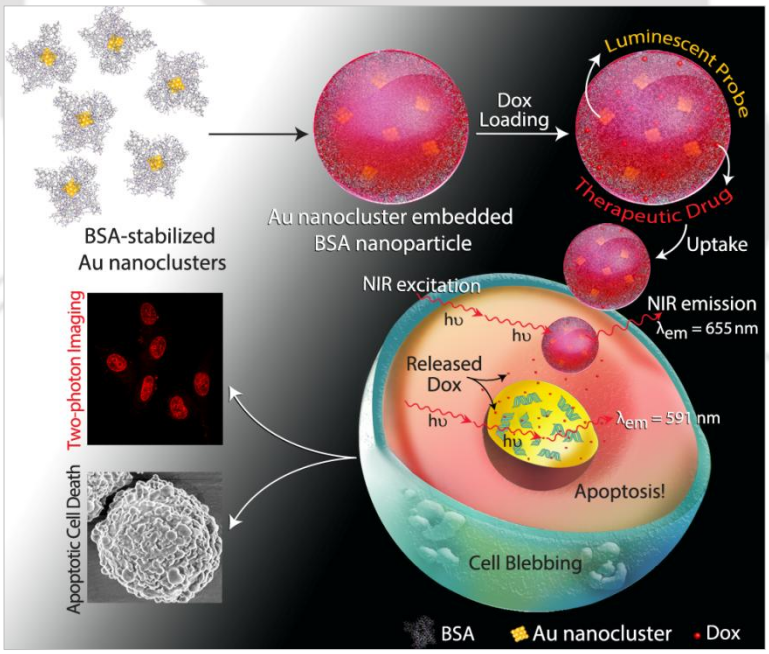

Scheme 5.1 A schematic illustration of the formation of Dox loaded Au nanocluster embedded BSA nanoparticles, followed by uptake and release of Dox inside the HeLa cells, leading to apoptotic cell death in addition to two-photon imaging.

5.3 Conclusions

In conclusion, we were able to fabricate nanotheranostic BSA nanoparticles having Au nanoclusters as the luminescent probe and which could incorporate anticancer drug Dox with high efficiency. The nanoparticles were biocompatible, non-cytotoxic, highly photostable and have suitable quantum yield and large Stokes shifted emission. Moreover, their excitation (by two-photon) and emission fall in the NIR 650-900 nm window, thus satisfying an essential criterion for in vivo imaging. These nanoparticles released the anticancer drug Dox to the cancer cells, leading to apoptotic cell death. The luminescence of both Au nanoclusters and Dox were found to be useful – Au clusters helped in tracking the uptake of the nanoparticles by the cancer cells; whereas, the luminescence of Dox helped in probing the intracellular release of the drug. Interestingly, the Dox loaded and Au cluster embedded BSA nanoparticles were of size, which is known to be suitable for passive targeting of tumor cells through the EPR effect. They also retained their luminescence in human blood serum. These nanoparticles have the potential to find use in clinical applications especially for in vivo imaging and combination therapy where the nanoclusters in conjunction with the conventional drug would be used for therapy using radiation.

CHAPTER 6

Thesis Overview and Future Outlook

6.1 Overview of the Thesis

The present thesis described the generation of gold nanoparticle (Au NP)-protein agglomerates via interaction with single protein as well as binary protein mixtures. The interaction of Au NPs with proteins was depended mainly on the charge on the surface of the NP as well as the protein. For example, the negatively charged citrate-stabilized Au NPs (Cit-Au NPs) interacted with positively charged protein lysozyme (Lyz) to form nanoagglomerates. On the other hand, the interaction of Cit-Au NPs with binary protein mixture was not only depended on the charges of the interacting moieties but also on the concentration and the mode of addition of proteins in a binary mixture.

These agglomerates were demonstrated to encapsulate non-covalently both the hydrophilic and hydrophobic anticancer drugs. Following drug encapsulation, these agglomerates were coated either with protein bovine serum albumin (BSA) or polymer poly(lactic-co-glycolic acid) (PLGA), which provided stability to the agglomerates against further agglomeration and precipitation. In addition to this, both types of coating have their own advantages – like the albumin coating facilitates intratumor accumulation of the nanocarrier, whereas, the PLGA coating provides stability to the agglomerates against protease degradation in the presystemic circulation. The albumin coated nanocarrier has the possibility to be used for intravenous delivery, whereas, the PLGA coated nanocarrier can be used for both intravenous and oral deliveries. Both the nanocarriers were internalized by the human cervical cancer HeLa cells, where they released their payloads causing apoptotic cell death. The nanocarriers themselves were not toxic to the cells, but when loaded either with hydrophilic or hydrophobic drug killed the cancer cells efficiently. The nanocarriers were found to be stable in human blood serum and met the size criterion for possible passive targeting of tumor cells through the enhanced permeation and retention (EPR) effect.

We have also demonstrated the incorporation of luminescent gold nanoclusters in the protein agglomerates, which could facilitate imaging guided drug delivery.

These gold nanoclusters have the capability to be imaged both by one- and two-photon excitations, with the two-photon excitation and emission wavelengths lying in the biologically important 650-900 nm NIR window. Moreover, the luminescence of the nanoclusters was retained after drug (doxorubicin) encapsulation. The nanoclusters were highly photostable, have suitable quantum yield and large Stokes-shifted emission. These nanoclusters are also known to be used for X-ray computed tomography imaging and cancer radiotherapy. The overview of the thesis is shown pictorially in **Figure 6.1.**

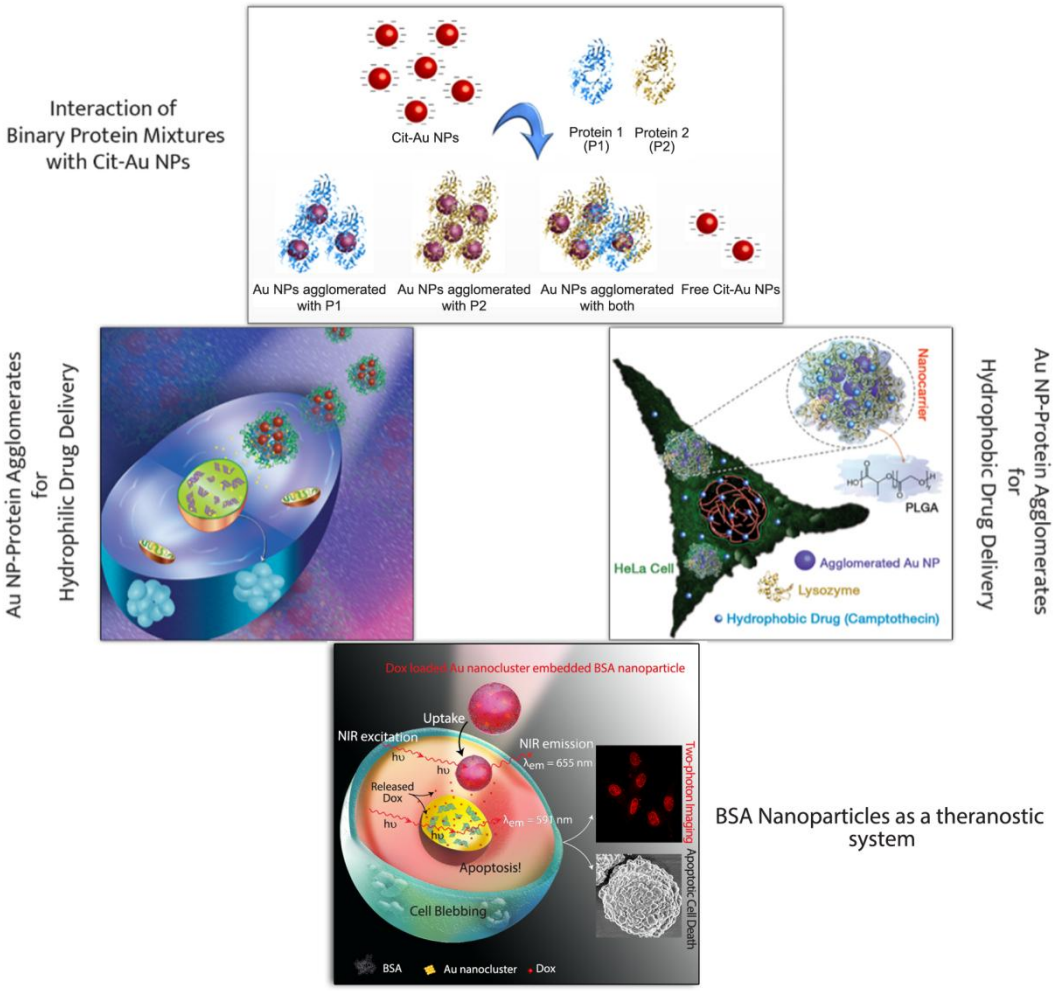

Figure 6.1 A schematic representation of the overview of the thesis work.

6.2 Future Outlook

1. The agglomerated Au NPs in the nanocarriers (mentioned in Chapters 3 and 4), with their optical extinction in the NIR region, could possibly be used for photodynamic cancer therapy.
2. The NP-protein agglomerates could also be used for the simultaneous encapsulation of more than one anticancer drug (all hydrophilic or all hydrophobic or some hydrophilic and some hydrophobic) for combinatorial therapy.
3. A three component (plasmonic + magnetic + imaging) nanoparticulate system could also be fabricated by combining Au NPs, Fe_3O_4 NPs and luminescent metal nanoclusters, all being incorporated in the proteins.
4. The gold nanoclusters embedded albumin nanoparticles (mentioned in Chapter 5) could also be used for encapsulation of more than one anticancer drug and cancer radiotherapy.
5. All the nanocarriers fabricated in this thesis could be used for in vivo applications.

Appendix

A2: Chapter 2

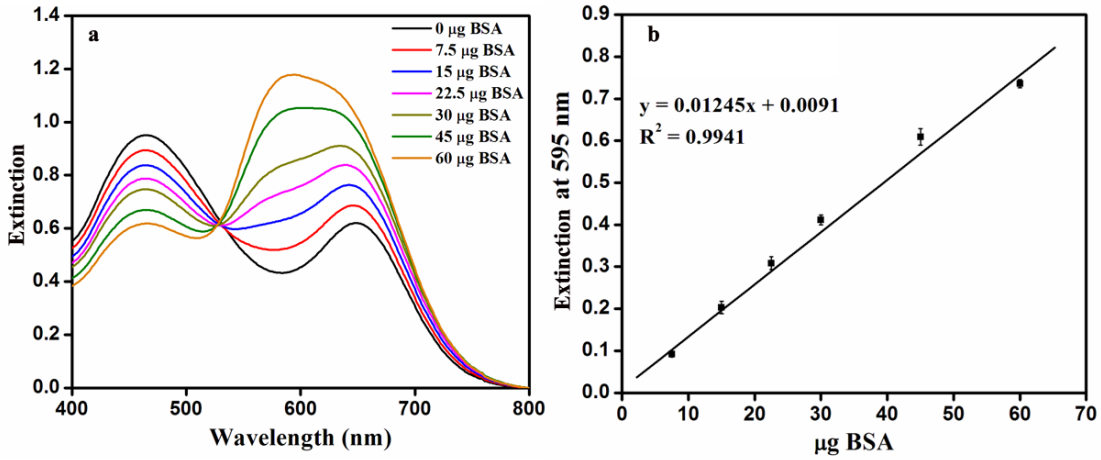

Figure 2A.1 Graphs representing Bradford assay of proteins. (a) UV-visible extinction spectra of Serva Blue G dye in the presence of various amounts of BSA as mentioned in the legends and (b) Standard curve representing extinction at 595 nm versus amount of BSA (in µg).

Table 2A.1 Combination of amount of α-amylase and BSA in their binary mixtures used for different sets of experiments in UV-visible measurements (the respective concentrations being mentioned in the Chapter 2). The concentrations of BSA and α-amylase stock solutions used were 0.1 mg mL^{-1} and 7.4 μg mL^{-1} respectively.

	α-amylase (μL)	Buffer (μL)		α-amylase (μL)	Buffer (μL)
BSA = 10 μL	10	140	**BSA = 20 μL**	10	130
	20	130		20	120
	30	120		30	110
	40	110		40	100
	50	100		50	90
	60	90		60	80
	70	80		70	70
	80	70		80	60
	90	60		90	50
	α-amylase (μL)	**Buffer (μL)**		**α-amylase (μL)**	**Buffer (μL)**
BSA = 40 μL	10	110	**BSA = 60 μL**	10	90
	20	100		20	80
	30	90		30	70
	40	80		40	60
	50	70		50	50
	60	60		60	40
	70	50		70	30
	80	40		80	20
	90	30		90	10
	α-amylase (μL)	**Buffer (μL)**		**BSA (μL)**	**Buffer (μL)**
BSA = 80 μL	10	70	**α-amylase = 20 μL**	10	130
	20	60		30	110
	30	50		50	90
	40	40		70	70
	50	30		90	50
	60	20		110	30
	70	10		130	10
	80	0		-	-

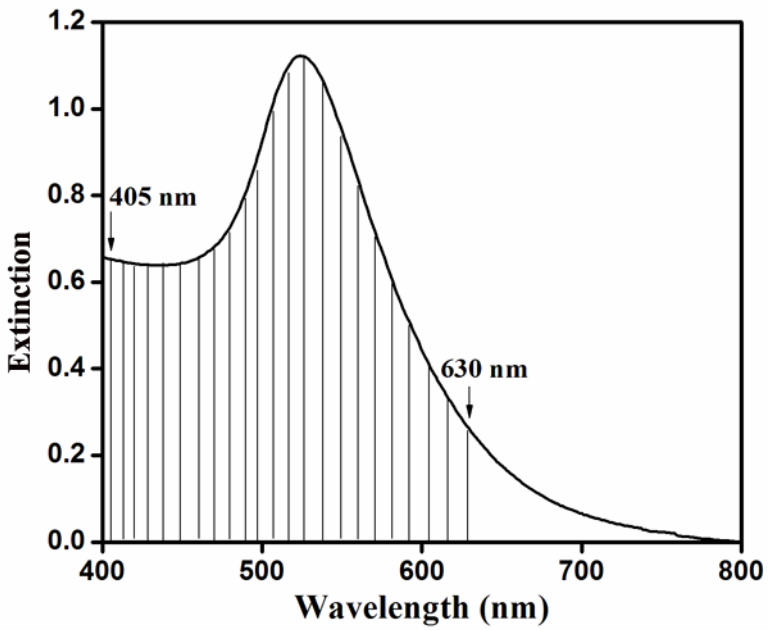

Figure 2A.2 A typical graph showing the area under the curve, after selecting the wavelength region, using the software associated with the UV-visible spectrophotometer.

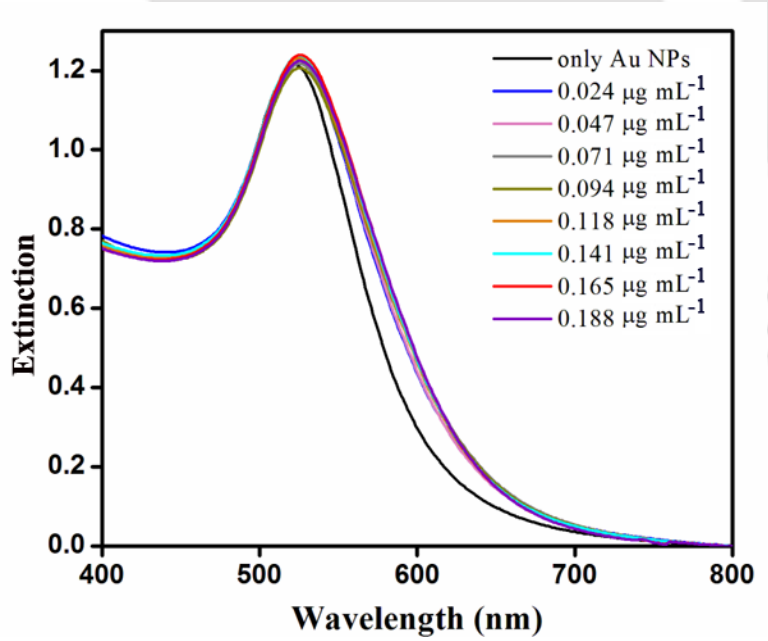

Figure 2A.3 SPR spectra of Cit-Au NP dispersion before and after addition of binary protein mixtures having different fractional content of α-amylase and BSA. Concentration of α-amylase was varied from 0.024 μg mL^{-1} to 0.188 μg mL^{-1} (the legends refer to different concentrations), keeping the concentration of BSA fixed at 2.532 μg mL^{-1}.

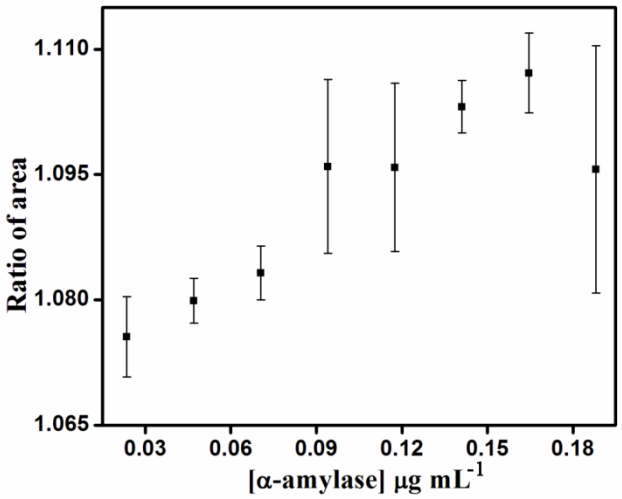

Figure 2A.4 Ratio of area under the UV-visible spectrum of Cit-Au NP dispersion in presence of different fractional content of α-amylase and BSA to that of Cit-Au NPs only plotted against α-amylase concentration (μg mL^{-1}). Concentration of α-amylase was varied from 0.024 μg mL^{-1} to 0.188 μg mL^{-1}, keeping the concentration of BSA fixed at 2.532 μg mL^{-1}. The error bars were calculated from the results of three independent experiments.

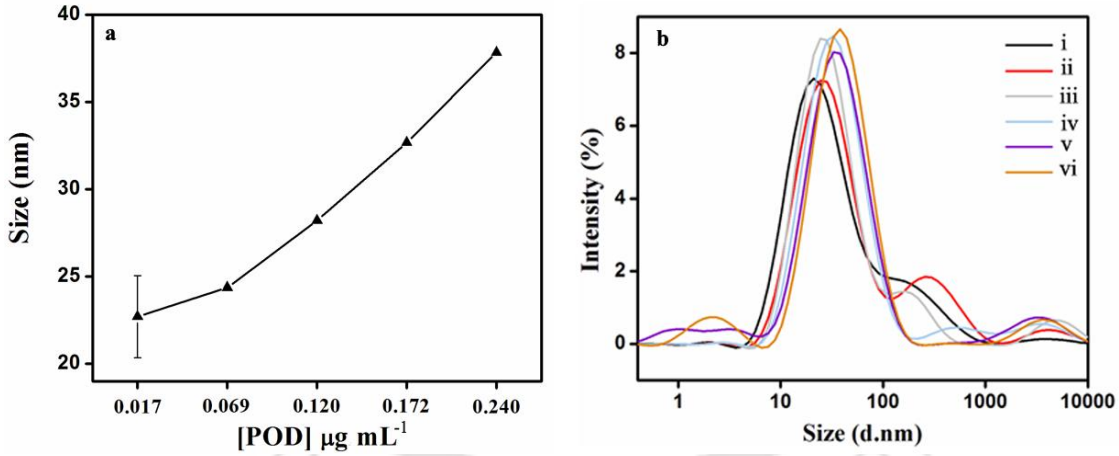

Figure 2A.5 (a) DLS analysis of Cit-Au NPs in presence of binary mixtures of GOD and POD. Concentration of POD was changed from 0.017 μg mL^{-1} to 0.240 μg mL^{-1}, keeping the concentration of GOD constant at 0.045 μg mL^{-1}. The size referred here corresponds to the maximum of the particle size distribution. The error bars were calculated from the results of two independent measurements carried out for the same sample. (b) Particle size distribution curves of Cit-Au NPs in presence of GOD and POD in the linear regime. The legends refer to (i) Cit-Au NPs only, (ii) Cit-Au NPs + 0.045 μg mL^{-1} GOD + 0.017 μg mL^{-1} POD, (iii) Cit-Au NPs + 0.045 μg mL^{-1} GOD + 0.069 μg mL^{-1} POD, (iv) Cit-Au NPs + 0.045 μg mL^{-1} GOD + 0.120 μg mL^{-1} POD, (v) Cit-Au NPs + 0.045 μg mL^{-1} GOD + 0.172 μg mL^{-1} POD and (vi) Cit-Au NPs + 0.045 μg mL^{-1} GOD + 0.240 μg mL^{-1} POD.

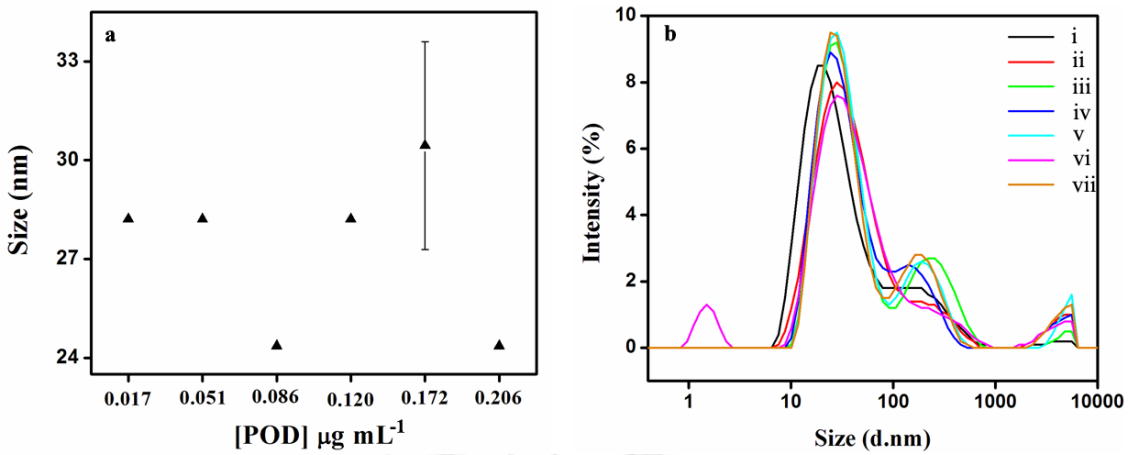

Figure 2A.6 (a) DLS analysis of Cit-Au NPs in presence of binary mixtures of GOD and POD. Concentration of POD was changed from 0.017 μg mL^{-1} to 0.206 μg mL^{-1}, keeping the concentration of GOD constant at 0.903 μg mL^{-1}. The size referred here corresponds to the maximum of the particle size distribution. The error bars were calculated from the results of two independent measurements carried out for the same sample. (b) Particle size distribution curves of Cit-Au NPs in presence of GOD and POD in the non-linear regime. The legends refer to (i) Cit-Au NPs only, (ii) Cit-Au NPs + 0.903 μg mL^{-1} GOD + 0.017 μg mL^{-1} POD, (iii) Cit-Au NPs + 0.903 μg mL^{-1} GOD + 0.051 μg mL^{-1} POD, (iv) Cit-Au NPs + 0.903 μg mL^{-1} GOD + 0.086 μg mL^{-1} POD, (v) Cit-Au NPs + 0.903 μg mL^{-1} GOD + 0.120 μg mL^{-1} POD, (vi) Cit-Au NPs + 0.903 μg mL^{-1} GOD + 0.172 μg mL^{-1} POD and (vii) Cit-Au NPs + 0.903 μg mL^{-1} GOD + 0.206 μg mL^{-1} POD.

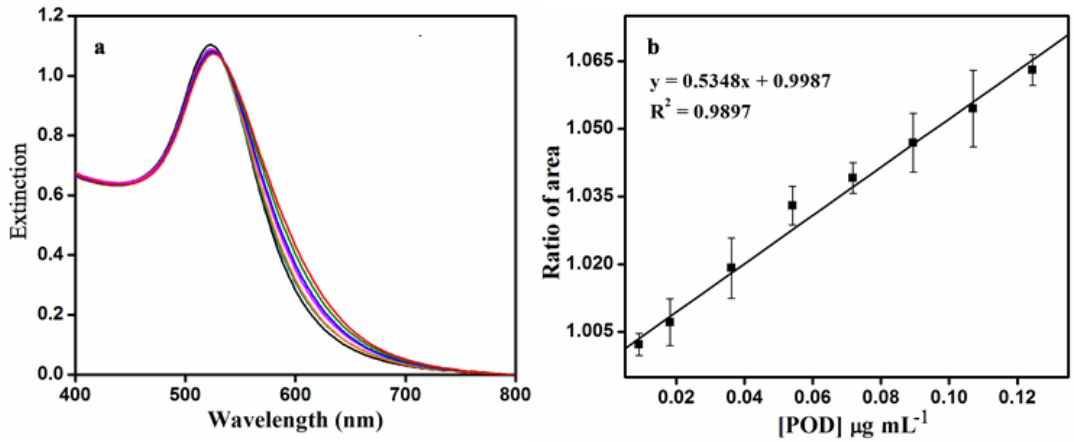

Figure 2A.7 (a) SPR extinction spectra of Cit-Au NP in the presence of increasing POD concentration and (b) Plot of the ratio of area under the extinction spectrum of Cit-Au NPs in presence of POD to that of Cit-Au NPs only as a function of concentration. POD sensitivity: 0.009 μg mL^{-1} to 0.124 μg mL^{-1}.

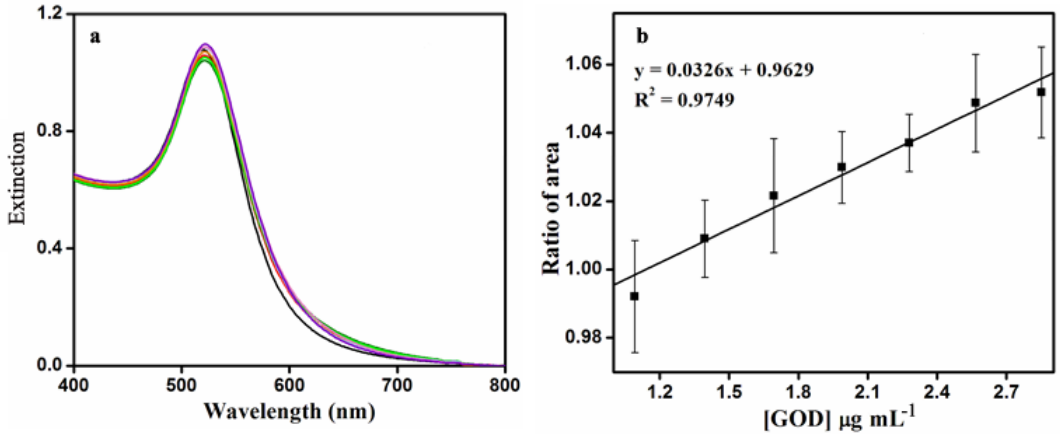

Figure 2A.8 (a) SPR extinction spectra of Cit-Au NP in the presence of increasing GOD concentration and (b) Plot of the ratio of area under the extinction spectrum of Cit-Au NPs in presence of POD to that of Cit-Au NPs only as a function of concentration. GOD sensitivity: 1.091 μg mL^{-1} to 2.851 μg mL^{-1}.

Table 2A.2 The sequence of addition of α-amylase and BSA to the Cit-Au NP dispersion to reach the final constant composition of the mixture and corresponding ratio of area under the extinction curves.

Composition of the final NP-protein solution	Ratio of area
3.0 mL Cit-Au NPs + (0.633 μg mL^{-1} α-amylase + 0.071 μg mL^{-1} BSA)	1.028 ± 0.010
(3.0 mL Cit-Au NPs + 0.633 μg mL^{-1} α-amylase) + 0.071 μg mL^{-1} BSA	1.025 ± 0.003
(3.0 mL Cit-Au NPs + 0.071 μg mL^{-1} BSA) + 0.633 μg mL^{-1} α-amylase	1.043 ± 0.008

Table 2A.3 The sequence of addition of α-amylase and BSA to the Cit-Au NP dispersion to reach the final constant composition of the mixture and corresponding ratio of area under the extinction curves.

Composition of the final NP-protein solution	Ratio of area
3.0 mL Cit-Au NPs + (0.118 μg mL^{-1} α-amylase + 1.899 μg mL^{-1} BSA)	1.037 ± 0.007
(3.0 mL Cit-Au NPs + 0.118 μg mL^{-1} α-amylase) + 1.899 μg mL^{-1} BSA	1.039 ± 0.005
(3.0 mL Cit-Au NPs + 1.899 μg mL^{-1} BSA) + 0.118 μg mL^{-1} α-amylase	1.048 ± 0.006

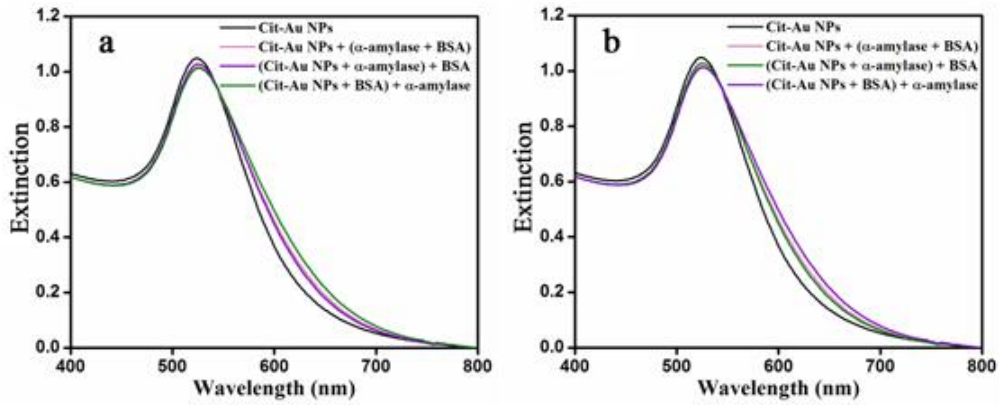

Figure 2A.9 SPR extinction spectra of Cit-Au NPs in absence and presence of binary mixture of proteins. (a) in presence of 0.633 μg mL^{-1} α-amylase and 0.071 μg mL^{-1} BSA and (b) in presence of 0.118 μg mL^{-1} α-amylase and 1.899 μg mL^{-1} BSA. The two proteins α-amylase and BSA were added following three different modes as mentioned in the Chapter 2.

Table 2A.4 The sequence of addition of α-amylase and AMG to the Cit-Au NP dispersion to reach the final constant composition of the mixture and corresponding ratio of area under the extinction curves.

Composition of the final NP-protein solution	Ratio of area
3.0 mL Cit-Au NPs + (0.118 μg mL^{-1} α-amylase + 0.157 μg mL^{-1} AMG)	1.032 ± 0.004
(3.0 mL Cit-Au NPs + 0.118 μg mL^{-1} α-amylase) + 0.157 μg mL^{-1} AMG	1.037 ± 0.006
(3.0 mL Cit-Au NPs + 0.157 μg mL^{-1} AMG) + 0.118 μg mL^{-1} α-amylase	1.087 ± 0.014

Table 2A.5 The sequence of addition of GOD and POD to the Cit-Au NP dispersion to reach the final constant composition of the mixture and corresponding ratio of area under the extinction curves.

Composition of the final NP-protein solution	Ratio of areas
3.0 mL Cit-Au NPs + (0.045 μg mL^{-1} POD + 0.043 μg mL^{-1} GOD)	1.001 ± 0.004
(3.0 mL Cit-Au NPs + 0.045 μg mL^{-1} POD) + 0.043 μg mL^{-1} GOD	1.001 ± 0.001
(3.0 mL Cit-Au NPs + 0.043 μg mL^{-1} GOD) + 0.045 μg mL^{-1} POD	1.017 ± 0.004

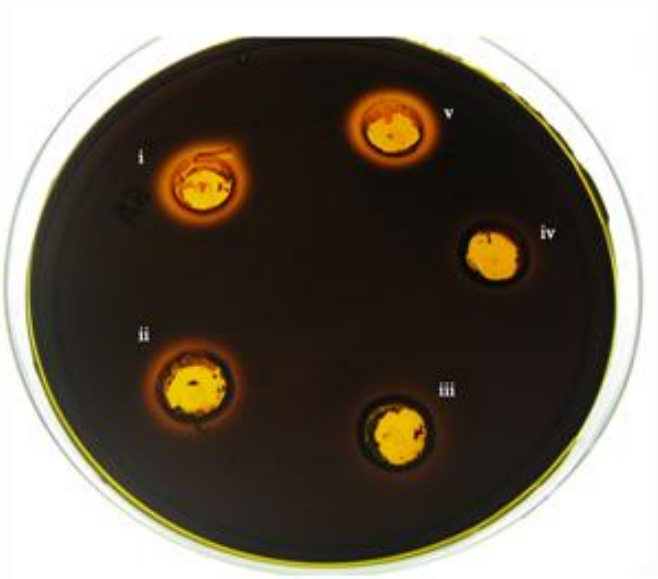

Figure 2A.10 Starch-agar plate assay for enzymatic activity of (i) pure α-amylase solution of 0.165 μg mL^{-1}, (ii) composite of Au NPs containing 1.266 μg mL^{-1} BSA and 0.235 μg mL^{-1} α-amylase, (iii) composite of Au NPs containing 1.266 μg mL^{-1} BSA and 0.094 μg mL^{-1} α-amylase (iv) composite of Au NPs containing 1.266 μg mL^{-1} BSA and 0.165 μg mL^{-1} α-amylase and (v) pure α-amylase solution of 0.235 μg mL^{-1}.

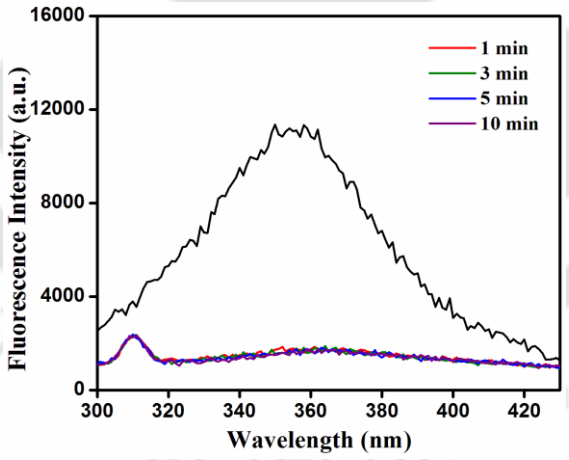

Figure 2A.11 Fluorescence spectra of binary mixture of α-amylase (0.118 μg mL^{-1}) and BSA (1.582 μg mL^{-1}) in the presence and absence of Cit-Au NPs at different times following sample preparation.

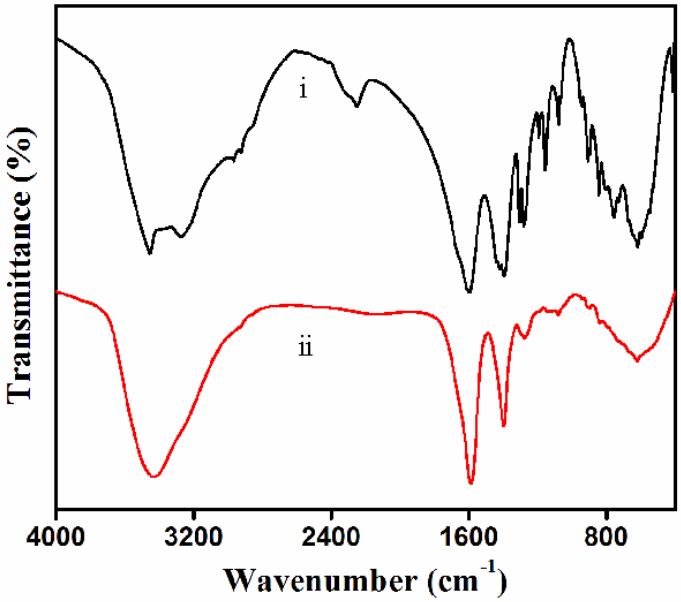

Figure 2A.12 FTIR spectra of (i) trisodium citrate dihydrate and (ii) Cit-Au NPs only.

A3: Chapter 3

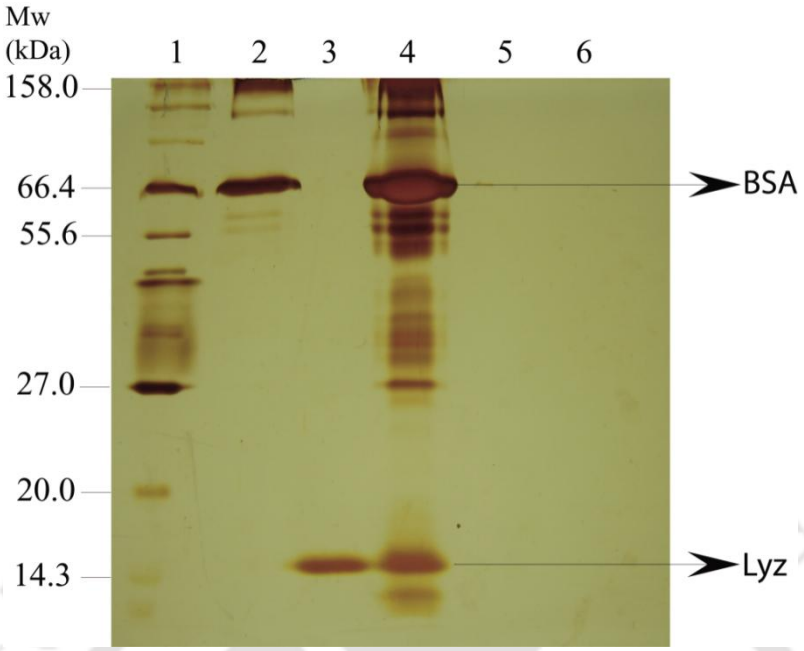

Figure 3A.1 SDS-PAGE analysis of nanocarriers, using silver-staining of the gel. Lanes corresponding to 1: New England Biolabs Protein marker; 2: BSA; 3: Lyz; 4: Nanocarriers; 5: Cit-Au NPs and 6: Dox. The molecular weights of the proteins in the marker used are reported on the left for reference.

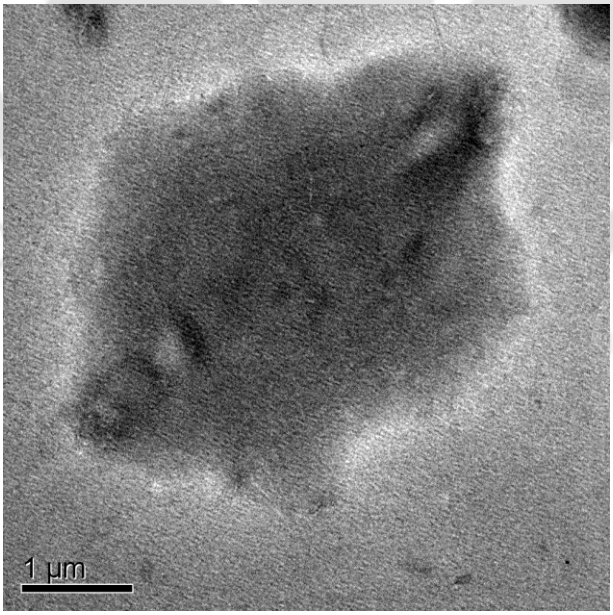

Figure 3A.2 TEM image of an untreated HeLa cell.

A4: Chapter 4

Table 4A.1 Compositions of the samples for SDS-PAGE analysis corresponding to Figure 4.4 a

Lane No.	Composition of SDS-PAGE Samples				
	Amount/ Sample	Water	Proteinase K	Loading Dye	Total Volume
1	5.0 µL of Protein Marker	11.0 µL	-	5.0 µL	21.0 µL
2	15.0 µL of 0.1 mg mL^{-1} Lyz	1.0 µL	-	5.0 µL	21.0 µL
3	15.0 µL of 0.1 mg mL^{-1}Lyz	-	1.0 µL of 250.0 µg mL^{-1}	5.0 µL	21.0 µL
4	15.0 µL of PLGA coated nanocarriers	1.0 µL	-	5.0 µL	21.0 µL
5	15.0 µL of PLGA coated nanocarriers	-	1.0 µL of 250.0 µg mL^{-1}	5.0 µL	21.0 µL
6	15.0 µL of PLGA coated nanocarriers	-	1.0 µL of 500.0 µg mL^{-1}	5.0 µL	21.0 µL
7	-	15.0 µL	1.0 µL of 250.0 µg mL^{-1}	5.0 µL	21.0 µL

Table 4A.2 Compositions of the samples for SDS-PAGE analysis corresponding to Figure 4.4 b

Lane No.	Composition of SDS-PAGE Samples				
	Amount/ Sample	Water	Proteinase K	Loading Dye	Total Volume
1	5.0 µL of Protein Marker	11.0 µL	-	5.0 µL	21.0 µL
2	15.0 µL of Au NP-Lyz agglomerates	1.0 µL	-	5.0 µL	21.0 µL
3	15.0 µL of Au NP-Lyz agglomerates	-	1.0 µL of 250.0 µg mL^{-1}	5.0 µL	21.0 µL

Table 4A.3 Compositions of the samples for SDS-PAGE analysis corresponding to Figure 4.4 c

Lane No.	Composition of SDS-PAGE Samples				
	Amount/ Sample	Water	Proteinase K	Loading Dye	Total Volume
1	5.0 µL of Protein Marker	11.0 µL	-	5.0 µL	21.0 µL
2	15.0 µL of 0.1 mg mL^{-1} Lyz	1.0 µL	-	5.0 µL	21.0 µL
3	15.0 µL of 0.1 mg mL^{-1} Lyz	-	1.0 µL of 500.0 µg mL^{-1}	5.0 µL	21.0 µL
4		15.0 µL	1.0 µL of 500.0 µg mL^{-1}	5.0 µL	21.0 µL
5	15.0 µL of 0.1 mg mL^{-1} albumin	1.0 µL	-	5.0 µL	21.0 µL
6	15.0 µL of 0.1 mg mL^{-1} albumin	-	1.0 µL of 500.0 µg mL^{-1}	5.0 µL	21.0 µL
7	15.0 µL of albumin coated nanocarriers	1.0 µL	-	5.0 µL	21.0 µL
8	15.0 µL of albumin coated nanocarriers	-	1.0 µL of 500.0 µg mL^{-1}	5.0 µL	21.0 µL

A5: Chapter 5

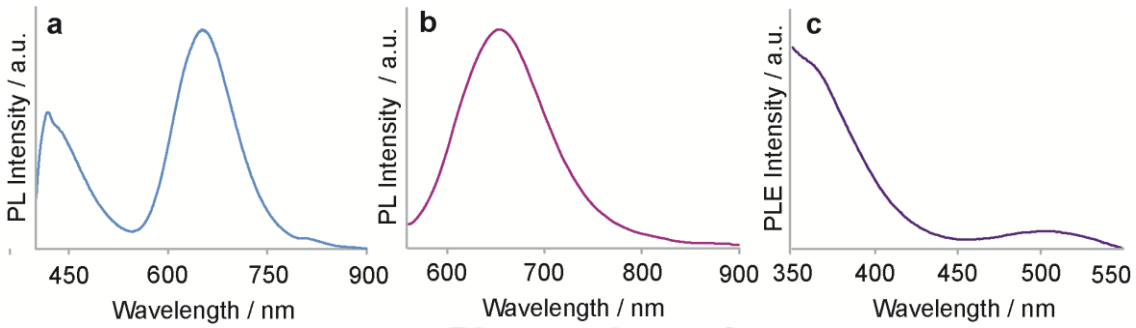

Figure 5A.1 Emission spectra (a) at λ_{ex} = 365 nm and (b) at λ_{ex} = 505 nm and (c) excitation spectrum (λ_{em} = 655 nm) of the aqueous dispersion of BSA-stabilized Au nanoclusters. The pH of the medium was adjusted to 8.2 before recording the spectrum.

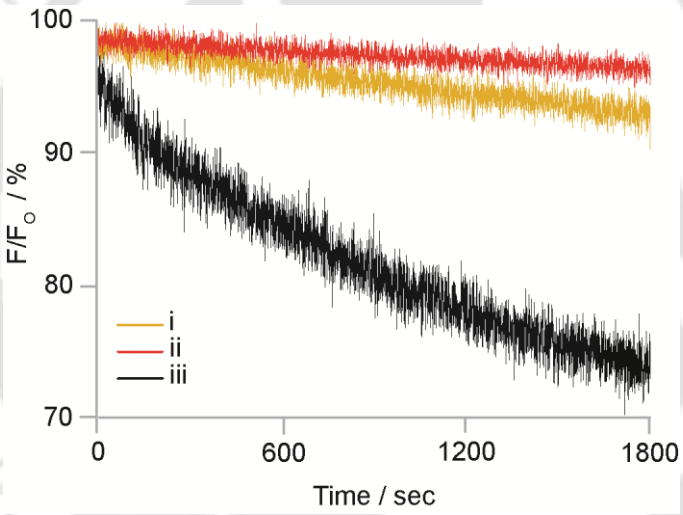

Figure 5A.2 Photostability results (as measured through luminescence) of (i) BSA-stabilized Au nanoclusters (λ_{em} = 659 nm), (ii) Au nanocluster embedded BSA nanoparticles (λ_{em} = 655 nm) and (iii) rhodamine 6G (λ_{em} = 560 nm) monitored with λ_{ex} = 365 nm.

Table 5A.1 Quantum yield (%) (with respect to rhodamine 6G in ethanol) of (i) BSA-stabilized Au nanoclusters (λ_{em} = 659 nm) and (ii) Au nanocluster embedded BSA nanoparticles (λ_{em} = 655 nm). The excitation wavelength was set at 505 nm.

Samples	Quantum Yield (%)
(i) BSA-stabilized Au nanoclusters	5.8
(ii) Au nanocluster embedded BSA nanoparticles	1.9

Quantum Yield (QY) Calculation: The quantum yields of the above samples were calculated using the following equation,

$$Q_S = Q_R \times \frac{I_S}{I_R} \times \frac{A_R}{A_S} \times \frac{\eta_S^2}{\eta_R^2}$$

Where Q_S = QY of sample, Q_R = QY of reference, I_S = area under PL curve of sample, I_R = area under PL curve of reference, A_R = absorbance of the reference, A_S = absorbance of the sample, η_S = refractive index of sample, η_R = refractive index of reference. QY of rhodamine 6G = 0.95 and refractive index of ethanol = 1.36 and water = 1.33.

The concentrations of the samples and the reference were adjusted in such a way that the optical densities were near to 0.1 at 505 nm excitation wavelength. The corrected optical densities for BSA-stabilized Au nanoclusters and Au nanocluster embedded BSA nanoparticles were obtained after subtracting the scattering (Rayleigh scattering for BSA-stabilized Au nanoclusters and Tyndall scattering for Au nanocluster embedded BSA nanoparticles) from the extinction.[93, 141]

It is important to mention here that 365 nm is not the actual excitation maximum of the Au nanoclusters. It is the Forster resonance energy transfer (FRET) between the BSA and the Au nanoclusters (inside the BSA) through which the nanoclusters get excited.[142] Thus, the quantum yield study was done at λ_{ex} 505 nm only.

Table 5A.2 Photodegradation rate (expressed in % per sec) of (i) BSA-stabilized Au nanoclusters (λ_{em} = 659 nm), (ii) Au nanocluster embedded BSA nanoparticles (λ_{em} = 655 nm) and (iii) rhodamine 6G (λ_{em} = 560 nm) as monitored with λ_{ex} = 365 and 505 nm.

Samples	Photodegradation Rate (% per sec)	
	λ_{ex} = 365 nm	λ_{ex} = 505 nm
(i) BSA-stabilized Au nanoclusters	0.005	0.005
(ii) Au nanocluster embedded BSA nanoparticles	0.003	0.003
(iii) Rhodamine 6G	0.015	0.01

Bibliography

[1] D. Peer, J. M. Karp, S. Hong, O. C. Farokhzad, R. Margalit, R. Langer, *Nat. Nanotechnol.* **2007**, *2*, 751–760.

[2] O. C. Farokhzad, R. Langer, *ACS Nano* **2009**, *3*, 16–20.

[3] M. De, P. S. Ghosh, V. C. Rotello, *Adv. Mater.* **2008**, *20*, 4225–4241.

[4] G. Bao, S. Mitragotri, S. Tong, *Annu. Rev. Biomed. Eng.* **2013**, *15*, 253–282.

[5] X. Liu, N. Huang, H. Li, H. Wang, Q. Jin, J. Ji, *ACS Appl. Mater. Interfaces* **2014**, *6*, 5657–5668.

[6] J. Kim, H. S. Kim, N. Lee, T. Kim, H. Kim, T. Yu, I. C. Song, W. K. Moon, T. Hyeon, *Angew. Chem.* **2008**, *120*, 8566–8569; *Angew. Chem. Int. Ed.* **2008**, *47*, 8438–8441.

[7] M. E. Davis, Z. G. Chen, D. M. Shin, *Nat. Rev. Drug Discov.* **2008**, *7*, 771–782.

[8] D. Sun, *Mol. Pharmaceutics* **2010**, *7*, 1879.

[9] S. T. Selvan, P. K. Patra, C. Y. Ang, J. Y. Ying *Angew. Chem. Int. Ed.* **2007**, *46*, 2448–2452.

[10] T. P. Stricker, V. Kumar, *Robbins Basic Pathology*, 8th edition.

[11] http://www.cancer.org/treatment/treatmentsandsideeffects/treatmenttypes/treatment-types-landing, accessed: February, **2015**.

[12] http://www.cancer.gov/cancertopics/treatment/types-of-treatment, accessed: February, **2015**.

[13] C. Carvalho, R. X. Santos, S. Cardoso, S. Correia, P. J. Oliveira, M. S. Santos, P. I. Moreira, *Curr Med Chem.* **2009**, *16*, 3267–3285.

[14] E. Miele, G. P. Spinelli, E. Miele, F. Tomao, S. Tomao, *Int. J. Nanomedicine* **2009**, *4*, 99–105.

[15] P. Botella, I. Abasolo, Y. Fernández, C. Muniesa, S. Miranda, M. Quesada, J. Ruiz, S. Schwartz Jr., A. Corma, *J. Control. Release* **2011**, *156*, 246–257.

[16] S. Parveen, R. Misra, S. K. Sahoo, *Nanomedicine: NBM* **2012,** *8*, 147–166.

[17] Z. Mi, T. G. Burke, *Biochemistry* **1994**, *33*, 10325–10336.

[18] J. Lu, S. C. Owen, M. S. Shoichet, *Macromolecules* **2011**, *44*, 6002–6008.

[19] H. Katas, Z. Hussain, S. A. Awang, *J.Nano Mat.* **2013**, *2013*, 9 pp.

[20] M. Morishita, N. A. Peppas, *Drug Discov Today* **2006**, *11*, 905–910.

[21] C. Damge, C. Michel, M. Aprahamian, P. Couvreur, J. P. Devissaguet, *J. Control. Release* **1990**, *13*, 233–239.

[22] A. Z. Wang, R. Langer, O. C. Farokhzad, *Annu. Rev. Med.* **2012**, *63*, 185–198.

[23] J. V. Jokerst, T. Lobovkina, R. N. Zare, S. S. Gambhir, *Nanomedicine*, **2011**, *6*, 715–728.

[24] T. Stylianopoulos, C. Wong, M. G. Bawendi, R. K. Jain, D. Fukumura, *Methods Enzymol.* **2012**, *508*, 109–130.

[25] M. S. Yavuz, Y. Cheng, J. Chen, C. M. Cobley, Q. Zhang, M. Rycenga, J. Xie, C. Kim, K. H. Song, A. G. Schwartz, L. V. Wang, Y. Xia, *Nature Mater.* **2009**, *8*, 935–939.

[26] J. C. Y. Kah, J. Chen, A. Zubieta, K. H. Schifferli, *ACS Nano* **2012**, *6*, 6730–6740.

[27] K. Dong, Z. Liu, Z. Li, J. Ren, X. Qu, *Adv. Mater.* **2013**, *25*, 4452–4458.

[28] M. Raoof, S. J. Corr, W. D. Kaluarachchi, K. L. Massey, K. Briggs, C. Zhu, M. A. Cheney, L. J. Wilson, S. A. Curley, *Nanomedicine* **2012**, *8*, 1096–1105.

[29] E. R. Hernandez, A. Baeza, M. V. Regi, *ACS Nano*, 2011, **5**, 1259–1266.

[30] S. H. Hu, S. Y. Chen, X. Gao, *ACS Nano* **2012**, *6*, 2558–2565.

[31] Y. Barenholz, *J. Control. Release* **2012**, *160*, 117–134.

[32] Y. Masayuki, M. Mizue, Y. Noriko, O. Teruo, S. Yasuhisa, *J. Control. Release* **1990**, *11*, 269–278.

[33] X. Ma, Z. Zhou, E. Jin, Q. Sun, B. Zhang, J. Tang, Y. Shen, *Macromolecules* **2013**, *46*, 37–42.

[34] A. M. Caminade, C. O. Turrin, *J. Mater. Chem. B* **2014**, *2*, 4055–4066.

[35] J. D. Gibson, B. P. Khanal, E. R. Zubarev, *J. Am. Chem. Soc*. **2007**, *129*, 11653–11661

[36] C. K. Kim, P. Ghosh, C. Pagliuca, Z. J. Zhu, S. Menichetti, V. M. Rotello, *J. Am. Chem. Soc*. **2009**, *131*, 1360–1361.

[37] S. S. Agasti, A. Chompoosor, C. C. You, P. Ghosh, C. K. Kim, V. M. Rotello, *J. Am. Chem. Soc*. **2009**, *131*, 5728–5729.

[38] C. Park, H. Youn, H. Kim, T. Noh, Y. H. Kook, E. T. Oh, H. J. Park, C. Kim, *J. Mater. Chem.* **2009**, *19*, 2310–2315.

[39] S. Aryal, J. J. Grailer, S. Pilla, D. A. Steeber, S. Gong, *J. Mater. Chem.* **2009**, *19*, 7879–7884.

[40] X. Zhang, H. Chibli, R. Mielke, J. Nadeau, *Bioconjugate Chem.* **2011**, *22*, 235–243.

[41] M. J. Hawkins, P. Soon-Shiong, N. Desai, *Adv. Drug Deliv. Rev.* **2008**, *60*, 876–885.

[42] M. G. Anhorn, S. Wagner, J. Kreuter, K. Langer, H. V. Briesen, *Bioconjugate Chem.* **2008**, *19*, 2321–2331.

[43] A. D. S. Krishna, R. K. Mandraju, G. Kishore, A. K. Kondapi, *PLoS ONE* **2009**, *4*, e7240.

[44] W. B. Liechty, D. R. Kryscio, B. V. Slaughter, N. A. Peppas, *Annu. Rev. Chem. Biomol. Eng.* **2010**, *1*, 149–173.

[45] H. K. Makadia, S. J. Siegel, *Polymers* **2011**, *3*, 1377–1397.

[46] J. M. Lu, X. Wang, C. M. Muller, H. Wang, P. H. Lin, Q. Yao, C. Chen. *Expert Rev Mol Diagn*. **2009**, *9*, 325–341.

[47] M. Gou, X. Zheng, K. Men, J. Zhang, L. Zheng, X. Wang, F. Luo, Y. Zhao, X. Zhao, Y. Wei, Z. Qian, *J. Phys. Chem. B* **2009**, *113*, 12928–12933.

[48] L. Meng, X. Zhang, Q. Lu, Z. Fei, P. J. Dyson, *Biomaterials* **2012**, *33*, 1689–1698.

[49] A. Bianco, K. Kostarelos, M. Prato, *Curr. Opin. Chem. Biol.* **2005**, *9*, 674–679.

[50] V. Bagalkot, L. Zhang, E. L. Nissenbaum, S. Jon, P. W. Kantoff, R. Langer, O. C. Farokhzad, *Nano Lett.* **2007**, *7*, 3065–3070.

[51] W. Lohcharoenkal, L. Wang, Y. C. Chen, Y. Rojanasakul, *BioMed Res. Int.* **2014**, *2014*, 12 pp.

[52] F. Kratz, B. Elsadek, *J. Control. Release* **2012**, *161*, 429–445.

[53] M. Haas, F. Moolenaar, A. Elsinga, E. A. V. Wouden, P. E. D. Jong, D. K. F. Meijer, D. D. Zeeuw, *J. Drug Target.* **2002**, *10*, 81–89.

[54] V. Mohanta, G. Madras, S. Patil, *J. Phys. Chem. C* **2012**, *116*, 5333–5341.

[55] F. Kratz, *J. Control. Release* **2008**, *132*, 171–183.

[56] E. Miele, G. P. Spinelli, E. Miele, F. Tomao, S. Tomao, *Int. J. Nanomedicine* **2009**, *4*, 99–105.

[57] M. Haas, A. C. A. Kluppel, E. S. Wartna, F. Moolenaar, D. K. F. Meijer, P. E. D. Jong, D. D. Zeeuw, *Kidney Int.* **1997**, *52*, 1693–1699.

[58] J. F. Zayas, *Functionality of Proteins in Food,* Springer-Verlag, Berlin, Heidelberg, New York **1997**, p. 289.

[59] D. Zhang, O. Neumann, H. Wang, V. M. Yuwono, A. Barhoumi, M. Perham, J. D. Hartgerink, P. Wittung-Stafshede, N. J. Halas, *Nano Lett.* **2009**, *9*, 666–671.

[60] E. A. Simone, T. D. Dziubla, E. Arguiri, V. Vardon, V. V. Shuvaev, M. Christofidou-Solomidou, V. R. Muzykantov, *Pharm. Res.* **2009**, *26*, 250–260.

[61] G. Han, P. Ghosh, M. De, V. M. Rotello, *Nanobiotechnol*. **2007**, *3*, 40–45.

[62] F. Wang, Y. C. Wang, S. Dou, M. H. Xiong, T. M. Sun, J. Wang, *ACS Nano*. **2011**, *5*, 3679–3692.

[63] C. Kojima, Y. Umeda, A. Harada, K. Kono, *Colloids and Surfaces B: Biointerfaces* **2010**, *81*, 648–651.

[64] L. C. Kennedy, L. R. Bickford, N. A. Lewinski, A. J. Coughlin, Y. Hu, E. S. Day, J. L. West, R. A. Drezek, *Small* **2011**, *2*, 169–183.

[65] M. Colombo, S. Mazzucchelli, V. Collico, S. Avvakumova, L. Pandolfi, F. Corsi, F. Porta, D. Prosperi, *Angew. Chem.Int. Ed.* **2012**, *51*, 9272–9275.

[66] A. N. Shirazi, D. Mandal, R. K. Tiwari, L. Guo, W. Lu, K. Parang, *Mol. Pharmaceutics* **2013**, *10*, 500–511.

[67] J. Deka, A. Paul, A. Chattopadhyay, *J. Phys. Chem. C* **2009**, *113*, 6936–6947.

[68] J. Deka, A. Paul, A. Chattopadhyay, *Nanoscale* **2010**, *2*, 1405–1412.

[69] N. Nath, A. Chilkoti, *J. Am. Chem. Soc.* **2001**, *123*, 8197–8202.

[70] G. Mie, *Ann. Phys.* **1908**, *330*, 377–445.

[71] T. Lammers, F. Kiessling, W. E. Hennink, G. Storm, *Mol. Pharmaceutics* **2010**, *7*, 1899–1912.

[72] Y. Q. Sun, J. Liu, X. Lv, Y. Liu, Y. Zhao, W. Guo, *Angew. Chem.* **2012**, *124*, 7752–7754; *Angew. Chem. Int. Ed.* **2012**, *51*, 7634–7636.

[73] R. Weissleder, *Nat. Biotechnol.* **2001**, *19*, 316–317.

[74] X. He, J. Gao, S. S. Gambhir, Z. Cheng, *Trends Mol. Med.* **2010**, *16*, 574–583.

[75] W. Qin, D. Ding, J. Liu, W. Z. Yuan, Y. Hu, B. Liu, B. Z. Tang, *Adv. Funct. Mater.* **2012**, *22*, 771–779.

[76] D. Ding, K. Li, W. Qin, R. Zhan, Y. Hu, J. Liu, B. Z. Tang, B. Liu, *Adv. Healthcare Mater.* **2013**, *2*, 500–507.

[77] L. M. Maestro, J. E. Ramirez-Hernandez, N. Bogdan, J. A. Capobianco, F. Vetrone, J. Garcia Sole, D. Jaque, *Nanoscale* **2012**, *4*, 298–302.

[78] U. Resch-Genger, M. Grabolle, S. Cavaliere-Jaricot, R. Nitschke, T. Nann, *Nat. Methods* **2008**, *5*, 763–775.

[79] Z. Wang, J. Li, J. Cho, A. B. Malik, *Nat. Nanotechnol.* **2014**, *9*, 204–210.

[80] S. Sripriyalakshmi, C. H. Anjali, P. D. George, B. Rajith, R. Aswathy, *PLoS ONE* **2014**, *9*, e86317.

[81] C. Wong, T. Stylianopoulos, J. Cui, J. Martin, V. P. Chauhan, W. Jiang, Z. Popovic, R. K. Jain, M. G. Bawendi, D. Fukumura, *Proc. Natl. Acad. Sci. U.S.A.* **2011**, *108*, 2426–2431.

[82] J. H. Park, G. Maltzahn, E. Ruoslahti, S. N. Bhatia, M. J. Sailor, *Angew. Chem.* **2008**, *120*, 7394–7398; *Angew. Chem. Int. Ed.* **2008**, *47*, 7284–7288.

[83] C. A. J. Lin, T. Y. Yang, C. H. Lee, S. H. Huang, R. A. Sperling, M. Zanella, J. K. Li, J. L. Shen, H. H. Wang, H. I. Yeh, W. J. Parak, W. H. Chang, *ACS Nano* **2009**, *3*, 395–401.

[84] A. Retnakumari, S. Setua, D. Menon, P. Ravindran, H. Muhammed, T. Pradeep, S. Nair, M. Koyakutty, *Nanotechnology* **2010**, *21*, 055103 (12pp).

[85] Y. Wang, J. Chen, J. Irudayaraj, *ACS Nano* **2011**, *5*, 9718–9725.

[86] C. L. Liu, H. T. Wu, Y. H. Hsiao, C. W. Lai, C. W. Shih, Y. K. Peng, K. C. Tang, H. W. Chang, Y. C. Chien, J. K. Hsiao, J. T. Cheng, P. T. Chou, *Angew. Chem.* **2011**, *123*, 7194–7198; *Angew. Chem. Int. Ed.* **2011**, *50*, 7056–7060.

[87] C. Wang, J. Li, C. Amatore, Y. Chen, H. Jiang, X. M. Wang, *Angew. Chem.* **2011**, *123*, 11848–11852; *Angew. Chem. Int. Ed.* **2011**, *50*, 11644–11648.

[88] C. V. Durgadas, C. P. Sharma, K. Sreenivasan, *Analyst* **2011**, *136*, 933–940.

[89] X. Wu, X. He, K. Wang, C. Xie, B. Zhou, Z. Qing, *Nanoscale* **2010**, *2*, 2244–2249.

[90] A. Zhang, Y. Tu, S. Qin, Y. Li, J. Zhou, N. Chen, Q. Lu, B. Zhang, *J. Colloid Interface Sci.* **2012**, *372*, 239–244.

[91] Z. Luo, K. Zheng, J. Xie, *Chem. Commun.* **2014**, *50*, 5143–5155.

[92] J. Xie, Y. Zheng, J. Y. Ying, *J. Am. Chem. Soc.* **2009**, *131*, 888–889.

[93] S. Raut, R. Chib, R. Rich, D. Shumilov, Z. Gryczynski, I. Gryczynski, *Nanoscale* **2013**, *5*, 3441–3446.

[94] X. L. Guevel, *IEEE J. Sel. Topics Quantum Electron.* **2014**, *20*, 6801312.

[95] X. D. Zhang, J. Chen, Z. Luo, D. Wu, X. Shen, S. S. Song, Y. M. Sun, P. X. Liu, J. Zhao, S. Huo, S. Fan, F. Fan, X. J. Liang, J. Xie, *Adv. Healthcare Mater.* **2014**, *3*, 133–141.

[96] J. N. Israelachvili, *Intermolecular and Surface Forces*, 2nd ed. London: Academic Press, **1992**.

[97] M. Bostrom, D. R. M. Williams, B. W. Ninham, ***Phys. Rev. Lett.*** **2001**, *87*, 168103 (1)–168103 (4).

[98] P. Mulvaney, *Langmuir* **1996**, *12*, 788–800.

[99] C. Rocker, M. Potzl, F. Zhang, W. J. Parak, G. U. Nienhaus, *Nature Nanotech*. **2009**, *4*, 577–580.

[100] A. Lamanda, Z. Cheaib, M. D. Turgut, A.Lussi, *PLoS ONE* **2007**, *2*, e263.

[101] K. Y. Chun, P. Stroeve, *Langmuir* **2002**, *18,* 4653–4658.

[102] J. H. Pazur, K. Kleppe, *Biochemistry* **1964**, *3*, 578–583.

[103] C. Xialing, M. Lin, *J. Biochem. Tech.* **2009**, *1*, 92–95.

[104] A. Faccenda, C. A. Bonham, P. O. Vacratsis, X. Zhang, B. Mutus, *J. Am. Chem. Soc.* **2010**, *132*, 11392–11394.

[105] A. Rangnekar, T. K. Sarma, A. K. Singh, J. Deka, A. Ramesh, A. Chattopadhyay, *Langmuir* **2007**, *23*, 5700–5706.

[106] V. R. S. Babu, M. A. Kumar, N. G. Karanth, M. S. Thakur, *Biosens. Bioelectron.* **2004**, *19*, 1337–1341.

[107] M. Iosin, F. Toderas, P. L. Baldeck, S. Astilean, *J. Mol. Struct.* **2009**, *924-926*, 196–200.

[108] L. Shang, Y. Wang, J. Jiang, S. Dong, *Langmuir* **2007**, *23*, 2714–2721.

[109] W. K. Surewicz, H. H. Mantsch, D.Chapman, *Biochemistry* **1993**, *32*, 389–394.

[110] N. S. Myshakina, Z. Ahmed, S. A. Asher, *J. Phys. Chem. B* **2008**, *112*, 11873–11877.

[111] I. Ojea-Jimenez, N. G. Bastus, V. Puntes, *J. Phys. Chem. C* **2011**, *115*, 15752–15757.

[112] K. K. Karukstis, E. H. Z. Thompson, J. A. Whiles, R. J. Rosenfeld, *Biophys. Chem.* **1998**, *73*, 249–263.

[113] A. Albanese, P. S. Tang, W. C. W. Chan, *Annu. Rev. Biomed. Eng.* **2012**, *14*, 1–16.

[114] A. Albanese, W. C. W. Chan, *ACS Nano* **2011**, *5*, 5478–5489.

[115] F. Yuan, M. Dellian, D. Fukumura, M. Leunig, D. A. Berk, V. P. Torchilin, R. K. Jain, *Cancer Res*. **1995**, *55*, 3752–3756.

[116] S. Dhar, E. M. Reddy, A. Prabhune, V. Pokharkar, A. Shiras, B. L. V. Prasad, *Nanoscale* **2011**, *3*, 575–580.

[117] N. Husain, R. A. Agbaria, I. M. Warner, *J. Phys. Chem.* **1993**, *97*, 10857–10861.

[118] J. Xia, P. L. Dubin, Y. Morishima, T. Sato, B. B. Muhoberac, *Biopolymers* **1995**, *35*, 411–418.

[119] S. H. Hu, S. Y. Chen, X. Gao, *ACS Nano* **2012**, *6*, 2558–2565.

[120] N. Ashley, J. Poulton, *Biochem. Biophys. Res. Commun.* **2009**, *378*, 450–455.

[121] J. M. Escoffre, J. Piron, A. Novell, A. Bouakaz, *Mol. Pharmaceutics* **2011**, *8*, 799–806.

[122] Q. Ling-bo, B. Xi-xi, R. Yu, C. Xiao-ying, Y. Lan-lan, *Journal of Instrumental Analysis* **2012**, *31*, 644–650.

[123] A. Giteau, M. C. Venier-Julienne, A. Aubert-Pouëssel, J. P. Benoit, *Int. J. Pharm.* **2008**, *350*, 14–26.

[124] R. K. Pujala, *Dispersion Stability, Microstructure and Phase Transition of Anisotropic Nanodiscs*, Springer Theses, Switzerland **2014**, p. 31.

[125] Calcein technical sheet – Interchim, http://www.interchim.fr/ft/4/466251.pdf, accessed: February, **2014**.

[126] C. Jin, L. Bai, H. Wu, Z. Teng, G. Guo, J. Chen, *J. Nanopart. Res.* **2008**, *10*, 1045–1052.

[127] S. Xiong, X. Zhao, B. C. Heng, K. W. Ng, J. S. C. Loo, *Biotechnol. J.* **2011**, *6*, 501–508.

[128] J. Panyam, V. Labhasetwar, *Pharm. Res.* **2003**, *20*, 212–220.

[129] V. J. Venditto, E. E. Simanek, Mol. Pharmaceutics **2010**, *7*, 307–349.

[130] P. Botella, I. Abasolo, Y. Fernandez, C. Muniesa, S. Miranda, M. Quesada, J. Ruiz, S. Schwartz Jr, A. Corma, *J. Control. Release* **2011**, *156*, 246–257.

[131] P. Kocbek, N. Obermajer, M. Cegnar, J. Kos, J. Kristl, *J. Control. Release* **2007**, *120* ,18–26.

[132] R. Dinarvand, N. Sepehri, S. Manoochehri, H. Rouhani, F. Atyabi, *Int. J. Nanomed.* **2011**, *6*, 877–895.

[133] J. Xie, Y. Zheng, J. Y. Ying, *J. Am. Chem. Soc.* **2009**, *131*, 888–889.

[134] J. Y. Jun, H. H. Nguyen, S. Y. R. Paik, H. S. Chun, B. C. Kang, S. Ko, *Food Chem.* **2011**, *127*, 1892–1898.

[135] I. M. Steinhauser, K. Langer, K. M. Strebhardt, B. Spankuch, *Biomaterials* **2008**, *29*, 4022–4028.

[136] X. Wang, P. Wu, Y. Lv, X. Hou, *Microchem. J.* **2011**, *99*, 327–331.

[137] Y. Xu, J. Sherwood, Y. Qin, D. Crowley, M. Bonizzoni, Y. Bao, *Nanoscale* **2014**, *6*, 1515–1524.

[138] M. A. H. Muhammed, P. K. Verma, S. K. Pal, A. Retnakumari, M. Koyakutty, S. Nair, T. Pradeep, *Chem. Eur. J.* **2010**, *16*, 10103–10112.

[139] X. L. Guevel, B. Hotzer, G. Jung, K. Hollemeyer, V. Trouillet, M. Schneider, *J. Phys. Chem. C* **2011**, *115*, 10955–10963.

[140] D. Agudelo, P. Bourassa, J. Bruneau, G. Berube, E. Asselin, H. A. Tajmir-Riahi, *PLoS ONE* **2012**, *7*, e43814.

[141] Quantitative UV-Visible Analysis in the Presence of Scattering, http://www.chem.agilent.com/Library/applications/59633927.pdf, accessed: December, **2014**.

[142] P. L. Xavier, K. Chaudhari, P. K. Verma, S. K. Pal, T. Pradeep, *Nanoscale* **2010**, *2*, 2769–2776.

List of Publications

In Peer Reviewed Journals:

1. **R. Khandelia**, J. Deka, A. Paul, A. Chattopadhyay. Signatures of specificity of interactions of binary protein mixtures with citrate-stabilized gold nanoparticles. *RSC Adv.* **2012,** *2***,** 5617–5628.

2. **R. Khandelia**, A. Jaiswal, S. S. Ghosh, A. Chattopadhyay. Gold Nanoparticle–Protein Agglomerates as Versatile Nanocarriers for Drug Delivery. *Small* **2013,** *9*, 3494–3505.

3. **R. Khandelia**, A. Jaiswal, S. S. Ghosh, A. Chattopadhyay. Polymer coated Gold Nanoparticle–Protein Agglomerates as Nanocarriers for Hydrophobic Drug Delivery. *J. Mater. Chem. B* **2014**, *2*, 6472–6477.

4. **R. Khandelia**, S. Bhandari, U. N. Pan, S. S. Ghosh, A. Chattopadhyay. Gold Nanocluster embedded Albumin Nanoparticles for Two-photon Imaging of Cancer Cells accompanying Drug Delivery (*Submitted* **2015**).

5. S. Bhandari, **R. Khandelia**, U. N. Pan, A. Chattopadhyay. Targeted Cellular Imaging of Surface Complexation Based Magnetofluorescent Biocompatible Probe (*To be communicated*).

In Conference Proceedings:

1. **Rumi Khandelia** and Arun Chattopadhyay. A New Nanocarrier in Cancer Drug Delivery Block. *International Symposium on Nanotechnology & Cancer Theranostics* (**ISNACT-2015**)**,** Indian Institute of Technology Bombay, India.

2. **Rumi Khandelia** and Arun Chattopadhyay. A New Paradigm in Cancer Drug Delivery. *1 st Indo-Sweden Workshop on Advanced Materials for Healthcare and Energy* (**2014**)**,** Indian Institute of Technology Guwahati, India.

3. **Rumi Khandelia** and Arun Chattopadhyay. A New Paradigm in Cancer Drug Delivery. *INDO-US Meeting On Advanced Materials: Current Trends & Future Prospects* (**2014**)**,** Manali, India.

4. **Rumi Khandelia**, Siddhartha Sankar Ghosh and Arun Chattopadhyay. Gold Nanoparticle-Protein Agglomerates as Versatile Drug Delivery Vehicles. *International Conference on Advanced Nanomaterials and Nanotechnology* (**ICANN-2013**), Indian Institute of Technology Guwahati, India.

5. **Rumi Khandelia**, Amit Jaiswal, Siddhartha Sankar Ghosh and Arun Chattopadhyay. Nanoparticle-Protein Agglomerates for Theranostic Applications. *Young Scientists' Colloquium* (**YSC-2013**), Jadavpur University, Kolkata, India.

6. **Rumi Khandelia**, Amit Jaiswal, Siddhartha Sankar Ghosh and Arun Chattopadhyay. Nanoparticle-Protein Aggregates for Diagnostics and Therapeutics. *DAE-BRNS 4th Interdisciplinary Symposium on Materials Chemistry* (**ISMC-2012**), Bhabha Atomic Research Centre, Mumbai, India.

7. **Rumi Khandelia**, Amit Jaiswal, Siddhartha Sankar Ghosh and Arun Chattopadhyay. Application Potential of Nanoparticle-Protein Aggregates. *21st International Symposium on Processing and Fabrication of Advanced Materials* (**PFAM-2012**)*,* Institute of Technology Guwahati, India.

8. **Rumi Khandelia**, Jashmini Deka, Amit Jaiswal, Anumita Paul, S. S. Ghosh and Arun Chattopadhyay. Interaction of Gold Nanoparticles with Proteins and their

Biomedical Applications. *National Conference on Frontiers in Chemical Sciences* (**FICS-2012**), Indian Institute of Technology Guwahati, India.

9. **Rumi Khandelia**, Jashmini Deka, Anumita Paul and Arun Chattopadhyay. Probing the Interactions of a Binary Protein Mixture with Gold Nanoparticles using Optical Property Changes. *Indo-US Bilateral Workshop on Nanoparticle Assembly: From Fundamentals to Applications* (**2011**), Indian Institute of Technology Delhi, India.

10. **Rumi Khandelia**, Jashmini Deka, Anumita Paul and Arun Chattopadhyay. Interactions of Binary Protein Mixtures with Citrate-Stabilized Gold Nanoparticles. *International Conference on Advanced Nanomaterials and Nanotechnology* (**ICANN-2011**), Indian Institute of Technology Guwahati, India.

Permissions

ELSEVIER LICENSE
TERMS AND CONDITIONS

Feb 02, 2015

This is a License Agreement between Rumi Khandelia ("You") and Elsevier ("Elsevier") provided by Copyright Clearance Center ("CCC"). The license consists of your order details, the terms and conditions provided by Elsevier, and the payment terms and conditions.

All payments must be made in full to CCC. For payment instructions, please see information listed at the bottom of this form.

Supplier	Elsevier Limited The Boulevard,Langford Lane Kidlington,Oxford,OX5 1GB,UK
Registered Company Number	1982084
Customer name	Rumi Khandelia
Customer address	Department of Chemistry Guwahati, 781039
License number	3560851036468
License date	Feb 02, 2015
Licensed content publisher	Elsevier
Licensed content publication	Elsevier Books
Licensed content title	Methods in Enzymology
Licensed content author	Catarina Pinto Reis,Christiane Damgé
Licensed content date	2012
Number of pages	22
Start Page	109
End Page	130
Type of Use	reuse in a thesis/dissertation
Portion	figures/tables/illustrations
Number of figures/tables/illustrations	1
Format	both print and electronic
Are you the author of this Elsevier chapter?	No
Will you be translating?	No
Original figure numbers	Figure 6.1
Title of your thesis/dissertation	Interactive Proteins and Nanoscale Particles for Diagnostics and Therapeutics
Expected completion date	Mar 2015
Estimated size (number of pages)	5

RSC | Advancing the Chemical Sciences

Royal Society of Chemistry
Thomas Graham House
Science Park
Milton Road
Cambridge
CB4 0WF

Tel: +44 (0)1223 420 066
Fax: +44 (0)1223 423 623
Email: contracts-copyright@rsc.org

www.rsc.org

Acknowledgements to be used by RSC authors

Authors of RSC books and journal articles can reproduce material (for example a figure) from the RSC publication in a non-RSC publication, including theses, without formally requesting permission providing that the correct acknowledgement is given to the RSC publication. This permission extends to reproduction of large portions of text or the whole article or book chapter when being reproduced in a thesis.

The acknowledgement to be used depends on the RSC publication in which the material was published and the form of the acknowledgements is as follows:

- For material being reproduced from an article in *New Journal of Chemistry* the acknowledgement should be in the form:
  - [Original citation] - Reproduced by permission of The Royal Society of Chemistry (RSC) on behalf of the Centre National de la Recherche Scientifique (CNRS) and the RSC
- For material being reproduced from an article *Photochemical & Photobiological Sciences* the acknowledgement should be in the form:
  - [Original citation] - Reproduced by permission of The Royal Society of Chemistry (RSC) on behalf of the European Society for Photobiology, the European Photochemistry Association, and RSC
- For material being reproduced from an article in *Physical Chemistry Chemical Physics* the acknowledgement should be in the form:
  - [Original citation] - Reproduced by permission of the PCCP Owner Societies
- For material reproduced from books and any other journal the acknowledgement should be in the form:
  - [Original citation] - Reproduced by permission of The Royal Society of Chemistry

The acknowledgement should also include a hyperlink to the article on the RSC website.

The form of the acknowledgement is also specified in the RSC agreement/licence signed by the corresponding author.

Except in cases of republication in a thesis, this express permission does not cover the reproduction of large portions of text from the RSC publication or reproduction of the whole article or book chapter.

A publisher of a non-RSC publication can use this document as proof that permission is granted to use the material in the non-RSC publication.

VAT Registration Number: GB 342 1764 71 Registered Charity Number: 207890

JOHN WILEY AND SONS LICENSE TERMS AND CONDITIONS

Feb 02, 2015

This Agreement between Rumi Khandelia ("You") and John Wiley and Sons ("John Wiley and Sons") consists of your order details and the terms and conditions provided by John Wiley and Sons and Copyright Clearance Center.

License Number	3513780946099
License date	Nov 21, 2014
Licensed Content Publisher	John Wiley and Sons
Licensed Content Publication	Angewandte Chemie International Edition
Licensed Content Title	Insulin-Directed Synthesis of Fluorescent Gold Nanoclusters: Preservation of Insulin Bioactivity and Versatility in Cell Imaging
Licensed Content Author	Chien-Liang Liu,Hung-Tsung Wu,Yi-Hsuan Hsiao,Chih-Wei Lai,Chun-Wei Shih,Yung-Kang Peng,Kuo-Chun Tang,Hsing-Wei Chang,Yun-Chen Chien,Jong-Kai Hsiao,Juei-Tang Cheng,Pi-Tai Chou
Licensed Content Date	Jun 17, 2011
Pages	5
Type of use	Presentation/Slide Kit/Poster
Requestor type	University/Academic
Is the reuse sponsored by or associated with a pharmaceutical or medical products company?	no
Format	Print and electronic
Portion	Figure/table
Number of figures/tables	1
Original Wiley figure/table number(s)	Figure 3
Will you be translating?	No
Title of Presentation	Interactive Proteins and Nanoscale Particles for Diagnostics and Therapeutics
Name of sponsor	IIT Guwahati
Expected presentation date	Dec 2014
Billing Type	Invoice
Billing Address	None Department of Chemistry IIT Guwahati None Guwahati, India 781039 Attn: None
Total	**0.00 USD**

Total

Terms and Conditions

TERMS AND CONDITIONS

This copyrighted material is owned by or exclusively licensed to John Wiley & Sons, Inc. or one of its group companies (each a"Wiley Company") or handled on behalf of a society with which a Wiley Company has exclusive publishing rights in relation to a particular work (collectively "WILEY"). By clicking accept in connection with completing this

JOHN WILEY AND SONS LICENSE TERMS AND CONDITIONS

Feb 03, 2015

This Agreement between Rumi Khandelia ("You") and John Wiley and Sons ("John Wiley and Sons") consists of your license details and the terms and conditions provided by John Wiley and Sons and Copyright Clearance Center.

License Number	3561161054331
License date	Feb 03, 2015
Licensed Content Publisher	John Wiley and Sons
Licensed Content Publication	Small
Licensed Content Title	Nanocarriers: Gold Nanoparticle–Protein Agglomerates as Versatile Nanocarriers for Drug Delivery (Small 20/2013)
Licensed Content Author	Rumi Khandelia,Amit Jaiswal,Siddhartha Sankar Ghosh,Arun Chattopadhyay
Licensed Content Date	Oct 18, 2013
Pages	1
Type of use	Dissertation/Thesis
Requestor type	Author of this Wiley article
Format	Print and electronic
Portion	Figure/table
Number of figures/tables	1
Original Wiley figure/table number(s)	Frontispiece
Will you be translating?	No
Title of your thesis / dissertation	Interactive Proteins and Nanoscale Particles for Diagnostics and Therapeutics
Expected completion date	Mar 2015
Expected size (number of pages)	5
Requestor Location	Rumi Khandelia Department of Chemistry IIT Guwahati Guwahati, India 781039 Attn: Rumi Khandelia
Billing Type	Invoice
Billing Address	Rumi Khandelia Department of Chemistry IIT Guwahati Guwahati, India 781039 Attn: Rumi Khandelia
Total	0.00 USD

JOHN WILEY AND SONS LICENSE TERMS AND CONDITIONS

Feb 02, 2015

This Agreement between Rumi Khandelia ("You") and John Wiley and Sons ("John Wiley and Sons") consists of your order details and the terms and conditions provided by John Wiley and Sons and Copyright Clearance Center.

License Number	3513780253515
License date	Nov 21, 2014
Licensed Content Publisher	John Wiley and Sons
Licensed Content Publication	Small
Licensed Content Title	Gold Nanoparticle–Protein Agglomerates as Versatile Nanocarriers for Drug Delivery
Licensed Content Author	Rumi Khandelia,Amit Jaiswal,Siddhartha Sankar Ghosh,Arun Chattopadhyay
Licensed Content Date	Feb 27, 2013
Pages	12
Type of use	Dissertation/Thesis
Requestor type	Author of this Wiley article
Format	Print and electronic
Portion	Full article
Will you be translating?	No
Title of your thesis / dissertation	Interactive Proteins and Nanoscale Particles for Diagnostics and Therapeutics
Expected completion date	Dec 2014
Expected size (number of pages)	150
Billing Type	Invoice
Billing Address	None Department of Chemistry IIT Guwahati None Guwahati, India 781039 Attn: None
Total	**0.00 USD**

Total

Terms and Conditions

TERMS AND CONDITIONS

This copyrighted material is owned by or exclusively licensed to John Wiley & Sons, Inc. or one of its group companies (each a"Wiley Company") or handled on behalf of a society with which a Wiley Company has exclusive publishing rights in relation to a particular work (collectively "WILEY"). By clicking accept in connection with completing this licensing transaction, you agree that the following terms and conditions apply to this transaction (along with the billing and payment terms and conditions established by the Copyright Clearance Center Inc., ("CCC's Billing and Payment terms and conditions"), at the time that you opened your Rightslink account (these are available at any time at http://myaccount.copyright.com).

Terms and Conditions

- The materials you have requested permission to reproduce or reuse (the "Wiley Materials") are protected by copyright.